Proceedings of the
Annual Stability Conference
Structural Stability Research Council
Baltimore, Maryland, April 10-13, 2018

Looking Back at a Career Shaped by SSRC: Stimulating Stability Research Challenges

Dinar Camotim[1]

Abstract

The objective of this paper is to provide an overview of my research activity on structural stability in the last two decades, *i.e.*, since I joined the Structural Stability Research Council (SSRC), back in 1997. After a few introductory words and a brief visit to my association with SSRC over the years, the paper presents the main findings obtained in several investigations in which I have collaborated on topics/problems dealing with the geometrically non-linear behavior of thin-walled structural members and systems – the common thread is the fact that the vast majority of these findings have been originally reported at a SSRC Annual Stability Conference and can be found in the corresponding proceedings. The various topics or problems addressed are presented in chronological order (as much as possible) and concern (i) the stability, non-linear strength and design of pitched-roof frames, (ii) the distortional post-buckling behavior, ultimate strength and Direct Strength Method (DSM) design of cold-formed steel columns and beams, (iii) the lateral-torsional stability of doubly and singly symmetric web-tapered beams, (iv) Generalized Beam Theory (GBT) formulations and applications, (v) the stability, failure and DSM design of cold-formed steel equal-leg angle columns, and (vi) the post-buckling behavior, ultimate strength and DSM design of cold-formed steel columns and beams undergoing mode interaction phenomena involving distortional buckling, namely local-distortional, distortional-global or local-distortional-global interaction – analytical, numerical and experimental results are dealt with. In each case, the topic or problem under consideration is first outlined, by providing its key features and associated challenges. Then, the main goals of the research effort undertaken are described and followed by a necessarily brief presentation and discussion of the main results/findings obtained. Finally, the paper closes with a few concluding remarks.

1. Introduction

Although I had already heard about the Structural Stability Research Council (SSRC) in the early 80s, during my Ph.D. studies at the University of Waterloo (Ontario, Canada) under the supervision of the late John Roorda, it was not until 1990 that I had my first "live encounter" with this prestigious institution. This took place in Istanbul (Turkey), where I attended the "Fourth SSRC International Colloquium on Structural Stability (Mediterranean Session)", organized by Gülay Aşkar (now Gülay Altay) from Boğaziçi University, a former Research Associate at Lehigh University. By an incredible coincidence (premonition…) the first person I talked with during the whole Colloquium was no less than…Lynn Beedle himself! I explain how this happened: after the Colloquium pre-registration, all participants boarded buses heading to the Colloquium Welcome Cocktail, held on the Boğaziçi University campus,

[1] Professor, CERIS, ICIST, DECivil, Instituto Superior Técnico, Universidade de Lisboa, Portugal. <dcamotim@civil.ist.utl.pt>

with a breathtaking view over the Bosphorus strait – during the whole trip (almost an hour, due to the very heavy Istanbul traffic), and completely by accident (fate…), I sat next to this lovely distinguished elderly gentleman who had the patience to talk with a "Portuguese kid" and encourage him to join SSRC, by describing enthusiastically its activities and the advantages of becoming a member. I must confess that, in my heart, I was "recruited" on that day (September 16, 1990)! I only talked with Lynn Beedle once more in my life, still in Istanbul, to ask him to sign the copy of the book "Stability of Metal Structures – A World View", edited by him, which I had just purchased. To think that, almost 30 years later, I am receiving the SSRC Lynn S. Beedle Award is absolutely mind-boggling (much more so that you can possibly imagine…), completely beyond my wildest dreams.

Even if Lynn Beedle's advice never left my mind, it was not until 1995 that I "encountered" SSRC again, now in Budapest (Hungary) where I attended the SSRC-sponsored "International Colloquium on the Stability of Steel Structures", organized by the late Miklós Iványi, from the Budapest University of Technology (today Budapest University of Technology and Economics – BUTE), and where I saw for the first time (as far as I can remember) Ted Galambos and Don Sherman. Then, in 1996, I attended in Rio de Janeiro the "Fifth SSRC International Colloquium on Structural Stability (Brazilian Session)", organized by Ronaldo Battista from the Federal University of Rio de Janeiro. And, finally, I got to the "real thing" seven years after the first "encounter" with Lynn Beedle: I attended the 1997 "SSRC Annual Technical Sessions and Meeting" in Toronto (Ontario, Canada)[2] and it was "love at first sight". I enjoyed so much the familiar atmosphere, friendly discussions and creative scientific exchanges (I had so many "new ideas") that I have been coming back ever since: I did not miss a single "SSRC Annual Technical Sessions and Meeting" (until 2000) or "SSRC Annual Stability Conference" (since 2001, organized in the context of the AISC North American Steel Construction Conference – NASCC: The Steel Conference) up to now, which means 21 consecutive presences![3]

At this moment, I must say that I feel highly indebted to SSRC "twice". First, to its Executive Committee for having selected me as the recipient of such a prestigious Award – really, the crowning of a research career and the possibility of entering a "room" filled with so many people I have always admired and looked up to. But, more important than that, for having played such an important role in my research career: I could never have made it without the leadership, encouragement, motivation and, most of all, friendship provided by the "SSRC environment and family" – Section 1.1 shows a quite astonishing "quantification" of the role played by SSRC in my career. Throughout the years, I have been permanently and anxiously looking forward to the next Annual Stability Conference, both for professional and personal reasons – and that will never change!

1.1 The Role of SSRC in my Career

Soon after concluding my Ph.D., in 1985, I was drafted into the Portuguese Air Force[4], where I literally "did nothing" for over a year, before being able to return to my job of Assistant Professor at the Technical University of Lisbon[5]. There, I quickly found out the (completely illogical) hardships of "rookie life": a very heavy teaching load, often involving two or more courses per semester, and a lot of administrative duties (that could not be refused) combined to vaporize all the momentum left from my doctoral work. In addition, I had virtually no access to graduate students, all "absorbed" by the most senior faculty members.

---

[2] Afterwards I went to Waterloo to visit my former supervisor, John Roorda – the last time I saw him (without having to close my eyes).

[3] It should have been 22 presences in a row if SSRC had not "failed" me (for the first and only time): it did not organize the "Annual Technical Sessions and Meeting" in 1999.

[4] At that time, the military service was compulsory in Portugal, even if you could postpone it until your graduate studies were finished.

[5] The name changed to University of Lisbon in September, 2013.

The above difficulties, combined with my own flaws (lack of initiative and settlement in a kind of "Mediterranean comfort" groove…), help to explain why (i) the first M.A.Sc. and Ph.D. theses under my supervision were only completed in 1994 and 2001, respectively, and (ii) the second journal paper reporting my doctoral work was published only in 1993 – since I obtained my Ph.D. in 1985, there is absolutely no doubt that it is impossible to imagine a worse candidate for the MAJR Award…[6]

During all this time, (i) I taught many courses, devoting a lot of time to the careful preparation of high-quality notes[7], (ii) I continued to do some research (almost single-handedly), always striving to achieve as much quality as possible, which allowed me to attend a few prestigious international conferences (it was essential to learn from the best), (iii) I participated in Technical Committees involved in developing and updating Eurocode 3 ("Steel Structures"), always looking for scientific collaborations[8], (iv) I never stopped searching for research topics and problems (always dealing with structural stability), as well as for new ideas to tackle them, and, most of all, (v) I kept trying to find bright and passionate students and ways to motivate/attract them to opt for a research career[9]. My first attendance of a "SSRC Annual Technical Sessions and Meeting", in 1997, somehow provided the "connection" between all these various scattered efforts and, all of a sudden, my research career literally took off (when I was already 44 years old!) and has been flying pretty steadily ever since. Just to "quantify" this assertion, the bar chart displayed in Figure 1 provides the evolution of the number of international journal papers I co-authored between 1983 and 2018. It is obvious why the title of this paper mentions a "career shaped by SSRC"…

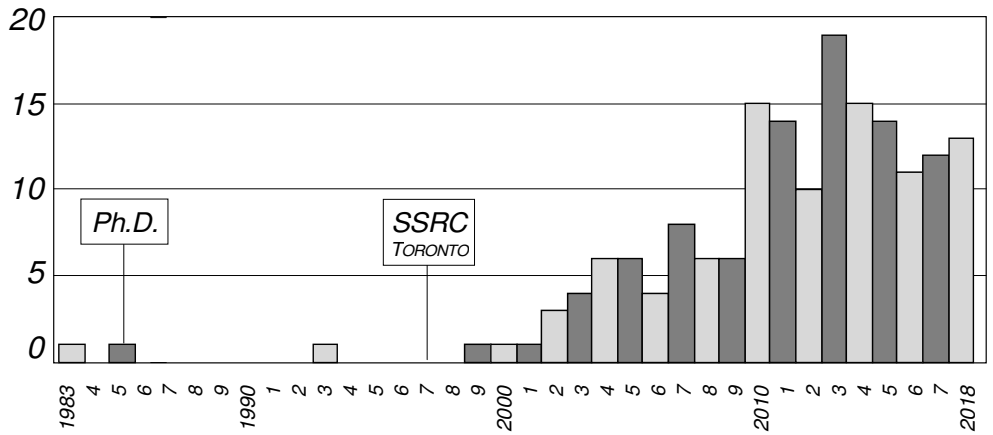

Figure 1: Evolution of the number of international journal papers I co-authored between 1983 and 2018

I served SSRC in several roles over the years: (i) Portuguese Corresponding Member, (ii) Co-Chair (with Miklós Iványi) and Chair of Task Group 11 ("International Cooperation on Stability Studies"), (iii) Executive Committee Member and (iv) Chair of the Vinnakota Award Committee – it has been a great privilege and pleasure to perform these tasks, and I am indebted to SSRC for having trusted me to do so[10].

---

[6] Fortunately, the tenure research requirements at the Technical University of Lisbon were minute at the time…

[7] Part of these notes led to the publication, in 2000 by McGraw-Hill Portugal, of a book on "Structural Stability" (in Portuguese).

[8] Having obtained my Ph.D. degree in North America, I was considerably "isolated" as far as collaborative research contacts were concerned. I tried to alter this situation by looking for scientific collaborations with European and Brazilian researchers.

[9] When presenting research topics to prospective graduate students, I never made them look easy (indeed, I often warned them about the difficulties), but I always characterized them as challenging and exciting (and, therefore, potentially very rewarding) – following the priceless lessons received from Professor S.T. Ariaratnam, at the University of Waterloo, I used to tell them that "there is no joy comparable to mastering a difficult problem" and that "the amount of joy is proportional to the level of difficulty". Naturally, this type of "joy" scared away most of the listeners, frequently all of them… – but those few (if any) remaining in the room were invariably outstanding.

[10] I am particularly thankful to Reidar Bjorhovde for having invited me to Co-Chair Task Group 11 when I was little more than "nobody".

It was also a great honor to organize the SSRC-sponsored "International Colloquium on Stability and Ductility of Steel Structures"[11], held in Lisbon (Portugal) on September 2006, which made it possible to have the pleasure of watching the SSRC logo/banner proudly displayed above the entrance of the Civil Engineering Pavilion of Instituto Superior Técnico (IST) – University of Lisbon School of Engineering.

Finally, I must acknowledge, from the bottom of my heart, the invaluable warmth provided by the SSRC membership during all these years, which "forced" me to come back to this conference over and over again. It is not at all surprising that several SSRC members are amongst my dearest and closest friends.

1.2 Content and Organization of the Paper

Since the content of this paper is intended to be presented in a lecture delivered during the session in which I receive the Lynn S. Beedle Award, granted because of a research career that has been so much influenced by my association with SSRC, I have decided to provide an overview of my research activity on structural stability in the last two decades, *i.e.*, since I joined SSRC back in 1997. The paper presents the main results/findings obtained in several investigations in which I have collaborated on topics/problems dealing with the geometrically non-linear behavior of thin-walled structural members and systems. The common thread between these results/findings is the fact that practically all of them were reported at SSRC Annual Stability Conferences (or Technical Sessions & Meetings) before appearing in international journals – up to this year I have co-authored 66 papers published in SSRC proceedings (full list given in Annex A).

The various topics/problems and results/findings, addressed in chronological order as much as possible, concern (i) the stability, non-linear strength and design of pitched-roof frames, (ii) the distortional post-buckling behavior, ultimate strength and Direct Strength Method (DSM) design of cold-formed steel columns and beams, (iii) the lateral-torsional stability of doubly and singly symmetric web-tapered beams, (iv) Generalized Beam Theory (GBT) formulations and applications, (v) the stability, failure and DSM design of cold-formed steel equal-leg angle columns, and (vi) the post-buckling behavior, ultimate strength and DSM design of cold-formed steel columns and beams affected by mode interaction phenomena involving distortional buckling, namely local-distortional, local-distortional-global or distortional-global interaction – analytical, numerical and experimental results are addressed. In each case, the topic/problem under consideration is first outlined, by providing its key features and associated challenges. Then, the main goals of the research effort undertaken are described and followed by a necessarily brief presentation and discussion of the main results/findings obtained. Finally, the paper closes with a few concluding remarks – and it must certainly open with the acknowledgments!

1.3 Acknowledgments

In Engineering, research findings are invariably the fruit of collaborative efforts involving several people and combining original thinking, breakthrough ideas, solid analytical, numerical and/or experimental concepts and skills, hard work and a fair amount of discipline. Therefore, no single person or competence can "claim" the full credit for a given success (or failure…). In my particular case, I have been blessed by being surrounded by top-class individuals with outstanding talent during my whole research career.

Everybody knows that the key ingredient leading to the success of a research endeavor is the quality of the graduate students collaborating in it. The research activities in which I have participated are no exception (on the contrary, they merely illustrate the above "rule") – indeed, their outcomes were always decisively influenced by the amount and quality of the work carried out by the M.A.Sc. and Ph.D. students involved. Therefore, most of the credit for the findings reported in this paper belongs to Nuno Silvestre (M.A.Sc.

[11] In 1999, it was decided to add the word "Ductility" to the Colloquium series title.

1997 and Ph.D. 2005), Rodrigo Gonçalves (M.A.Sc. 2000 and Ph.D. 2007), Luis Prola (Ph.D. 2001) Anísio Andrade (M.A.Sc. 2004 and Ph.D. 2013), Cilmar Basaglia (Ph.D. 2010), Rui Bebiano (Ph.D. 2010), Rui Fena (M.A.Sc. 2011), Miguel Abambres (Ph.D. 2014), Danilo Cava (M.A.Sc. 2015), Renato Cruz (M.A.Sc. 2015) and André Martins (Ph.D. 2018) – Cilmar Basaglia (2010-2013) and Rui Bebiano (2013-2017) were also post-doctoral fellows after completing their Ph.D. degrees. Some of these graduate students and post-doctoral fellows were co-supervised by my colleagues Nuno Silvestre (University of Lisbon), Pedro Borges Dinis (University of Lisbon), Rodrigo Gonçalves (Nova University of Lisbon) and Alexandre Landesmann (Federal University of Rio de Janeiro), always playing instrumental roles in the success of the corresponding research activities[12].

Everybody also knows how important, for the success of a research endeavor, is the (more or less formal) collaboration with colleagues and peers – in my case, also dear friends. I am particularly indebted to Eduardo Batista and Alexandre Landesmann (Federal University of Rio de Janeiro), and, most of all, to Ben Young (University of Hong Kong), for having worked very closely with me in many occasions, often "filling the experimental gap" in my own research by carefully performing jointly planned test campaigns that provided clear experimental evidence and validation of the analytical and numerical findings unveiled in Lisbon – all the experimental results presented in this paper originated from Hong Kong or Rio de Janeiro. The friendly, enjoyable and fruitful discussions and exchanges of ideas with Ben Schafer (Johns Hopkins University), Greg Hancock and Kim Ramussen (University of Sydney), Ron Ziemian (Bucknell University), René Maquoi (University of Liège) and Leroy Gardner (Imperial College London) are also very gratefully acknowledged – their comments, criticisms and suggestions contributed to improve the quality of several research findings reported in this paper (as well as to prevent the publication of a number of mistakes…).

The last words go to my "family" and my family. To my "sons" Cilmar and Alexandre, who combine the supreme Brazilian sense of humor with a surprising German work capacity, for the continuous support and gentle care. To my "brother" Pedro, the best person I ever met, for being everything to me during so many years (always with a smile in his face). To my Grandmother and Grandfather, who always live in my heart, for the gift of unconditional love and for making me believe that I was capable of doing anything I wanted. To my Father, the most intellectual, charismatic and sweet person I will ever come across, for having taught me the joy of learning, the importance of knowledge and the concepts of human dignity and "cleanliness of character". And to Isabel, my better half, for the privilege of going through life at my side, filling it with love, tenderness and laughter, and for achieving the miracle of being, at the same time, the deep and solid roots ensuring stability at home, and the light and powerful wings helping to master and conquer instability at the office.

2. Pitched-Roof Frames

This section addresses the in-plane behavior of unbraced single-bay pitched-roof steel frames (see Fig. 2(a)) – due to the sloping rafters such behavior is qualitatively very different from its orthogonal (beam-and-column) frame counterpart (Silvestre & Camotim 2007). The findings reported concern the in-plane stability, second-order effects and elastic design. Illustrative numerical results involving frames with fixed and pinned column bases are presented and discussed.

[12] Nuno Silvestre and Rodrigo Gonçalves, both my previous M.A.Sc. and Ph.D. students, are nowadays highly distinguished colleagues. While Rodrigo is the recipient of the SSRC 2017 MAJR Medal (in that quality, he will deliver an invited presentation immediately after this one) and has a very bright future ahead, Nuno is already enjoying an extremely bright present, in spite of his relatively young age – it suffices to mention that he has been recently appointed editor of the international journal Thin-Walled Structures! Nuno and Rodrigo are the "living proof" that I have easily and brilliantly fulfilled the primary requirement of a good teacher/supervisor: "to be outperformed by your students"!

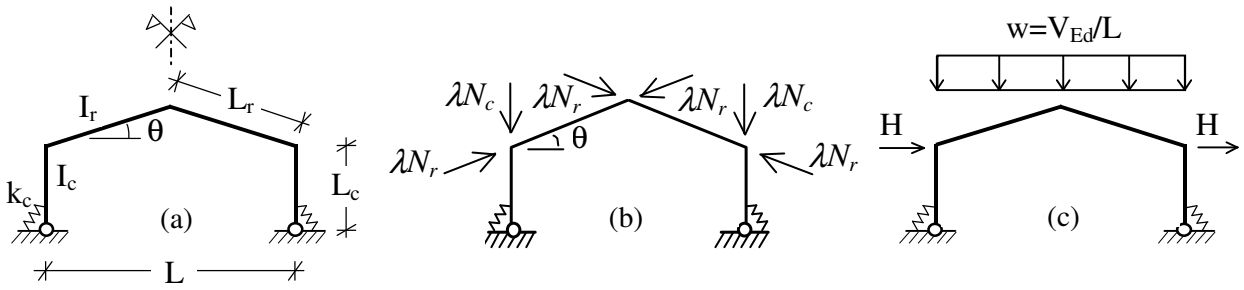

Figure 2: Pitched-roof frame (a) geometry, (b) stability loading and (c) in-plane loading

2.1 In-Plane Stability

Consider the symmetric pitched-roof frame depicted in Figure 2(a), exhibiting semi-rigid column bases (stiffness k_c) and acted only by column (N_c) and rafter (N_r) axial compressive forces, also symmetric and related by $R_N=N_r/N_c$ – see Figure 2(b). The in-plane global buckling behavior of this frame is governed by the two buckling modes shown in Figure 3(a), with anti-symmetric (ASM) and symmetric (SM) configurations – both involve sway displacements (horizontal displacements of the column tops)[13]. Figure 3(b) summarizes the essential features of the pitched-roof frame in-plane stability behavior: note that the critical load parameter $\lambda_{cr}=min\{\lambda_{AS};\lambda_S\}$ (λ_{AS} and λ_S are the load parameters associated with anti-symmetric and symmetric bifurcation – ASB and SB) strongly depends on the (i) rafter slope θ and (ii) axial load ratio R_N, as shown by the curves in Figure 3(b). They provide the N_c and N_r bifurcation values (both linearly dependent on λ – $N_{c.0}^{AS}$, $N_{c.0}^{S}$, $N_{r.0}^{AS}$ and $N_{r.0}^{S}$ are the bifurcation loads for R_N=0 (column compression only) and $R_N=\infty$ (rafter compression only). Their observation prompts the following remarks:

(i) While ASB (solid line) is independent from the rafter inclination, SB (dashed lines) exhibits a high dependence on θ – recall that the latter is mostly governed by the rafter instability.

(ii) For low R_N, $\lambda_{cr}=\lambda_{AS}$ (no dependence on θ). For high R_N, on the other hand, $\lambda_{cr}=\lambda_{AS}$ or $\lambda_{cr}=\lambda_S$, depending on the value of the rafter inclination θ.

(iii) The variation of λ_{cr} with R_N involves either (iii$_1$) both ASB and SB (*e.g.*, $\theta=\theta_1$) or (iii$_2$) only ASB (*e.g.*, $\theta=\theta_3$). Note also that common frame geometries correspond to quite close λ_{AS} and λ_S values.

In order to avoid the need to perform linear stability analyses to obtain λ_{AS} and λ_S, easy-to-use and accurate analytical expressions were developed in the context of frames with semi-rigid column bases (Silvestre & Camotim 1999). The bifurcation loads are provided by the expressions

$$\lambda = \left[\left(\frac{N_c}{\rho_{c.0} N_{Ec}} \right)^C + \left(\frac{N_r}{\rho_{r.0} N_{Er}} \right)^C \right]^{-1/C} \qquad C = \frac{1.2 + 1.6K}{1+K} \qquad , \quad (1)$$

with $\rho_{c.0}$ and $\rho_{r.0}$ given by the formulae given in Table 1, where (i) N_{Ec} and N_{Er} are the column and rafter Euler loads, (ii) N_c and N_r are column/rafter reference axial forces and (iii) $R=L_rI_c/L_cI_r$, $R_H=L_r\sin\theta/L_c$ and $K=k_cL_c/EI_c$. The formulae for pinned and fixed-base frames are obtained by making K tend to zero and infinity, respectively[14].

[13] These displacements may be (i) both "inward" or "outward" or (ii) one "inward" and the other "outward" – only the latter is relevant in orthogonal beam-and-column frames.

[14] These formulae were included in a book by Trahair *et al.* (2006) on the design and behavior of steel structures.

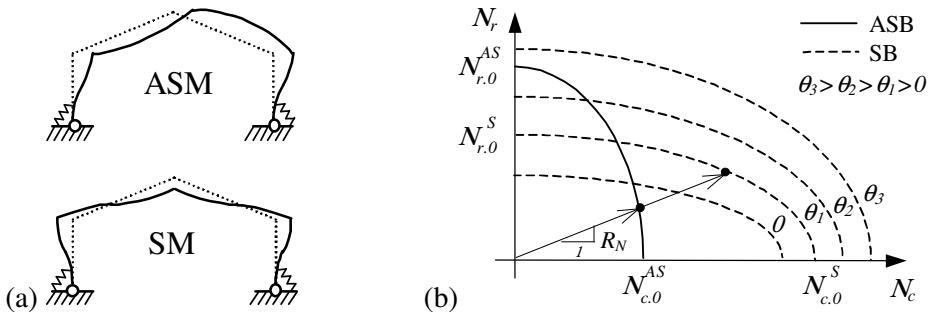

Figure 3: Pitched-roof frame (a) anti-symmetric (ASM) and symmetric (SM) sway buckling modes, and (b) variation of the N_c and N_r bifurcation values with θ and R_N (ASB and SB)

Table 1: Formulae to evaluate $\rho_{c.0}$ and $\rho_{r.0}$

	ASB	SB
$\rho_{c.0}$	$\dfrac{K\cdot(R+3)+3}{10R+12+K\cdot(4R+3)}$	$\dfrac{4.8+12R\cdot(1+R_H)+K\cdot(1+4.8R+4.2RR_H)}{2.4+12R\cdot(1+R_H)+7R^2R_H^2+K\cdot(2.4R+2R^2R_H^2)}$
$\rho_{r.0}$	$\dfrac{4+K\cdot(2R+4)}{4+K\cdot(R+4)}$	$\dfrac{12R+8.4RR_H+K\cdot(4R+4.2RR_H+R^2R_H^2)}{12R+4+K\cdot(4R+2)}$

2.2 Second-Order Behavior

Consider the pitched-roof frame displayed in Figure 2(a), now subjected to the horizontal (H) and vertical (w) loads indicated in Figure 2(c). Before addressing the geometrically non-linear behavior of this frame, it is important to recall some fundamental differences between the structural responses of pitched-roof and orthogonal (beam-and-column) frames (Silvestre *et al.* 1998):

(i) In orthogonal frames, the sway displacements of the two column tops are always virtually identical. In pitched-roof frames, on the other hand, these displacements are only equal if the two horizontal applied loads are identical (due to the sloping rafter lateral stiffness).

(ii) Symmetric (geometry and vertical loading) orthogonal frames have null column top displacements. Vertically loaded symmetric pitched-roof frames exhibit non negligible "outward" column top sway displacements (combined effect of the apex vertical displacement and rafter inclination).

(iii) In symmetric orthogonal frames the first-order sway deformed configuration and bending moment diagram stem exclusively from the applied horizontal loads – this feature is very important, since the validity of the "sway amplification method" (SAM) is based on the similarity between these first-order results and their frame critical buckling mode counterparts (Horne 1975). As will be shown next, pitched-roof frames do not share this feature.

It is possible to express the pitched-roof first-order deformed configuration and bending moment diagram as the sum of the following three components, shown in Figures 4(a)-(c) (Silvestre *et al.* 1998):

(i) The *non sway* components d_{NS} and M_{NS}, due to the vertical loading and assuming that the sway displacements are prevented by horizontal reaction forces R – see Figure 4(a).

(ii) The *symmetric sway* components d_{SS} and M_{SS}, which stem also from the vertical loading, through the application of horizontal forces opposite to the reactions R – see Figure 4(b).

(iii) The *anti-symmetric sway* components d_{AS} and M_{AS}, due to the horizontal loads[15] – see Figure 4(c).

[15] If the horizontal loading is not anti-symmetric (right and left horizontal forces not equal in sign and/or value), *both* the symmetric sway and anti-symmetric sway components are affected.

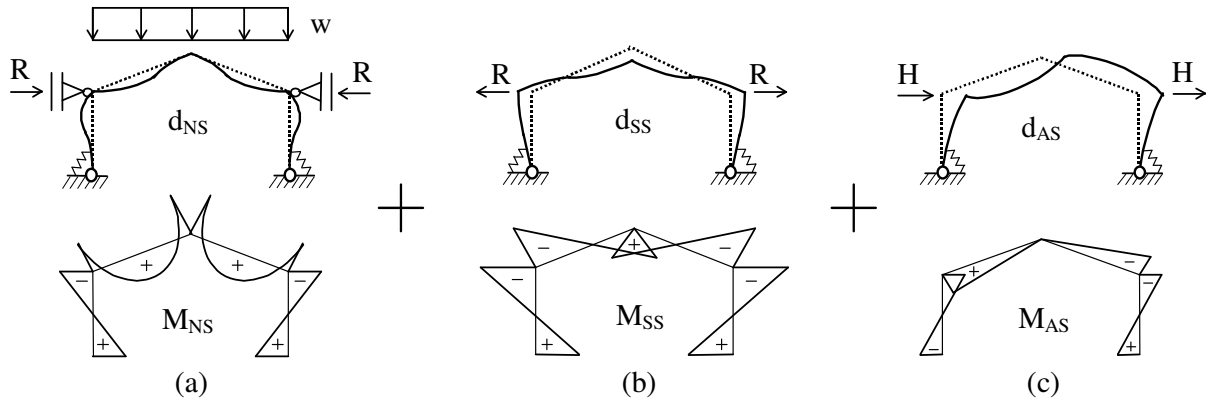

Figure 4: Pitched-roof frame first-order deformed configuration and bending moment distribution components: (a) non-sway (NS), (b) symmetric sway (SS) and (c) anti-symmetric sway (AS)

The maximum M_{SS} values are very often much larger than the M_{AS} ones – the two charts presented in Figures 5(a) (fixed-base frames) and 5(b) (pinned-base frames) enable a straightforward evaluation of the $\phi=M_{SS.max}/M_{AS.max}$ ratio: for a given geometry ($R_L=L_r/L_c$, $R_H=R_L sin\theta$, $R=I_cL_r/L_cI_r$) and loading ($V_{Ed}=wL$, $H_{Ed}=2H$) combination, determining ϕ just requires multiplying ϕ_0 or ϕ_∞, (read from the chart) by $(V_{Ed}/H_{Ed})(R_L cos\theta/18)$ – in semi-rigid base frames ($K=k_cL_c/EI_c$), ϕ can be approximately estimated by $\phi_S=(\phi_0+\phi_\infty K)/(1+K)$. The comparison between the frame (i) first-order sway deformed configurations d_{SS} and d_{AS} (see Figs. 4(b)-(c)) and (ii) symmetric and anti-symmetric buckling mode shapes (see Fig. 3(a)) shows a remarkable *similarity*. This fact, combined with (more or less) close buckling loads V_{AS} and V_S (total vertical loadings associated with λ_{AS} and λ_S), leads to conclusion that, in pitched-roof frames, an approximate second-order analysis based on the amplification concept must involve the *first and second* buckling loads/modes – this is a major difference with respect to orthogonal frames, in which only the first buckling load/mode is involved.

2.2.1 Sway displacement and moment amplification

A sway amplification method to estimate second-order (i) lateral displacements and (ii) elastic internal forces and moments (IFM), in unbraced symmetric pitched-roof frames, involves the following steps:

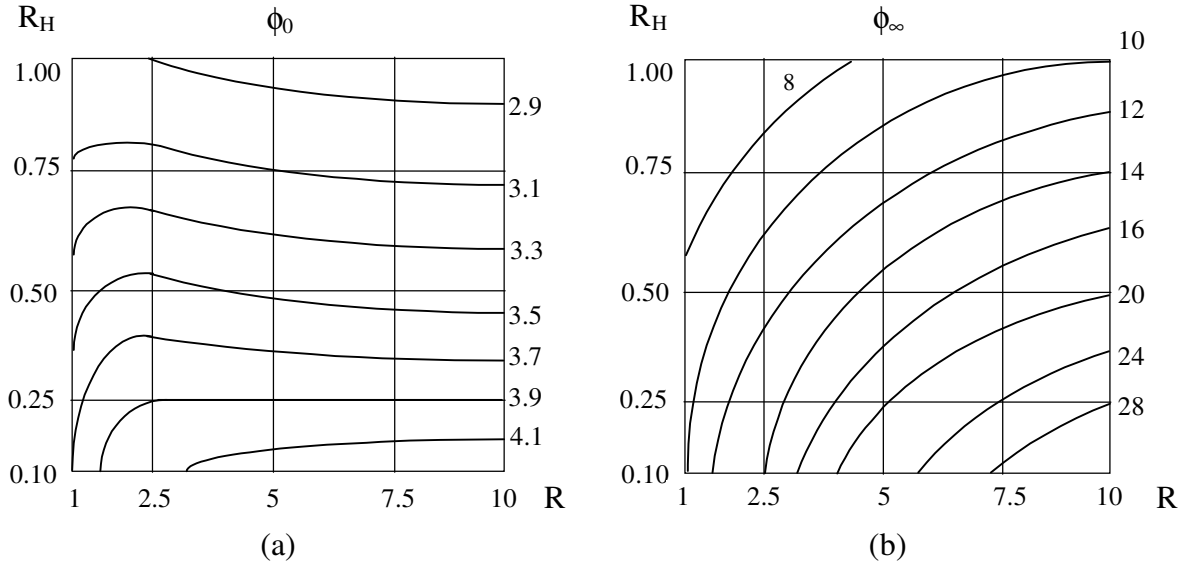

Figure 5: Charts to estimate the ratio $\phi=M_{SS.max}/M_{AS.max}$ in (a) fixed-base and (b) pinned-base pitched-roof frames

(i) Determination of the first-order member axial forces due to the applied vertical loads only[16].

(ii) Evaluation of the frame sway mode buckling loads $V_{AS}= \lambda_{AS} V_{Ed}$ and $F_S= \lambda_S V_{Ed}$, where V_{Ed} is the frame applied vertical loading.

(iii) Identification of the first-order deformed configuration, bending moment diagram, shear force diagram and axial force diagram components associated with (iii_1) the application of the vertical load in the braced frame, (iii_2) the sway displacements due to the vertical load and (iii_3) the sway displacements due to the horizontal loads (see Figs. 4(a)-(c)).

(iv) Estimation of the second order displacement and IFM values, by means of the expressions

$$d_{II} = d_{NS} + C_{SS} \cdot d_{SS} + C_{AS} \cdot d_{AS} \qquad M_{II} = M_{NS} + C_{SS} \cdot M_{SS} + C_{AS} \cdot M_{AS}$$

$$V_{II} = V_{NS} + C_{SS} \cdot V_{SS} + C_{AS} \cdot V_{AS} \qquad N_{II} = N_{NS} + N_{SS} + C_{AS} \cdot N_{AS} \quad , \quad (2)$$

$$C_{SS} = \frac{1}{1 - V_{Ed}/V_S} \qquad C_{AS} = \frac{1}{1 - V_{Ed}/V_{AS}} \quad . \quad (3)$$

Concerning the above sway amplification method, the following comments are appropriate:

(i) Unlike its anti-symmetric counterpart N_{AS}, the axial force component N_{SS} is not amplified – see Eq. $(2)_4$. This is due to the fact that the signs of the equal-valued additional bending moments generated by the *P-Δ* effects at the column bases are the same in the first case and opposite in the second one (see Figs. 6(a)-(b)). Thus, no additional "axial force binary" N_Δ is required to ensure equilibrium in the presence of the $(M_\Delta)_{SS}$ – they are self-equilibrated.

(ii) If the analytical expressions given in Eq. (1) and Table 1 are used to evaluate V_{AS} and V_S, it is possible to obtain second-order displacement and IFM estimates which including all relevant *P-Δ* effects and exclusively based on frame *first-order* results.

(iii) Unlike the usual sway amplification method, the proposed one involves the amplification of *two* first-order displacement and IFM components (instead of just one). The differences between the second-order estimates yielded by the two methods depend (iii_1) on V_S/V_{AS} and $M_{SS.max}/M_{AS.max}$ ratio values and (iii_2) on whether the symmetric sway component (not addressed in the usual method, most likely because it bears no relevance in orthogonal frames) is included in either the *non-sway* component (not amplified) or the anti-symmetric sway component (amplified by C_{AS}).

(iv) An extensive parametric study performed by Silvestre & Camotim (2007) showed that the sway amplification method yields very accurate and always safe second-order results for a wide variety of frame geometries and loadings.

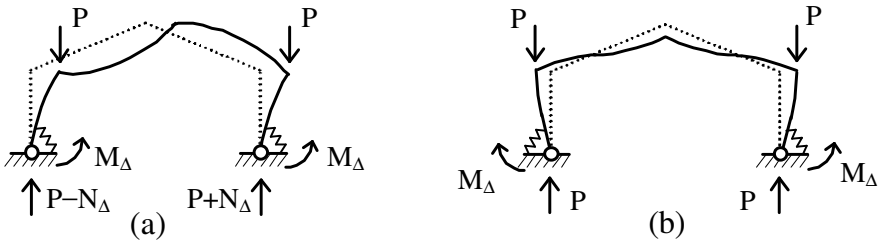

Figure 6: Equilibrium involving the additional (a) AS and (b) SS bending moments M_Δ

[16] Considering the column and rafter axial forces due to the horizontal loads has a negligible effect on the buckling load values.

2.3 Elastic Design

A novel rational approach to estimate the IFM design values in unbraced single-bay pitched-roof frames is formulated. In order to comply with the Eurocode 3 (CEN 2005) methodology, it comprises (i) a frame classification, with respect to its susceptibility to second-order effects (under a vertical loading) and, in "susceptible frames", (ii) the estimation of IFM design values incorporating the relevant *P-Δ* effects, by means of Eqs. (2)-(3). The frame classification is addressed next.

The basic concept behind the frame classification criterion is that *P-Δ* effects need only be taken into account when the ratio between the maximum second and first-order moments exceeds 1.10 (*i.e.*, if $M_{II.max}/M_{I.max} \geq 1.10$)[17]. In order to quantify of this concept, 36 pitched-roof frames were analyzed, all with E=210 *GPa*, HEB280 columns and L_c=5 *m*. The various frames correspond to all combinations of (i) IPE360-450 rafters, (ii) L=20-30-40 *m*, (iii) θ=6–12 ° and (iv) k_c=0–8090 *kNm-∞*. For each frame:

(i) ABAQUS was used to perform exact first and second-order analyses to obtain a large number of H_{Ed} and V_{Ed} values leading to a 10% moment increase due to *P-Δ* effects ($M_{II.max}/M_{I.max}$=1.10 at node D – see Fig. 2(c)).

(ii) For the V_{Ed} values determined in the previous item, linear stability analyses were performed to determine the corresponding V_{Ed}/V_{AS} and V_{Ed}/V_S values.

The results of this parametric study made it possible to establish that virtually all pitched-roof frames with common geometries are associated with the region comprised between the two "dash-dot" straight lines depicted in Figure 7(a), defined by V_S/V_{AS}=0.9 and V_S/V_{AS}=7.0. On the other hand, the five sets of points included in Figure 7(b) provide a representative sample of the numerical results obtained, namely those concerning frames (i) acted by applied loads satisfying H_{Ed}/V_{Ed}=0-0.1-0.2-0.3-0.4 and (ii) such that $M_{II.max}/M_{I.max}$=1.10 – the limit value for neglecting the *P-Δ* effects. On the basis of the above numerical investigation, the following classification criterion for pitched-roof frames was proposed: a frame is only classified as "non-susceptible to *P-Δ* effects" when the conditions

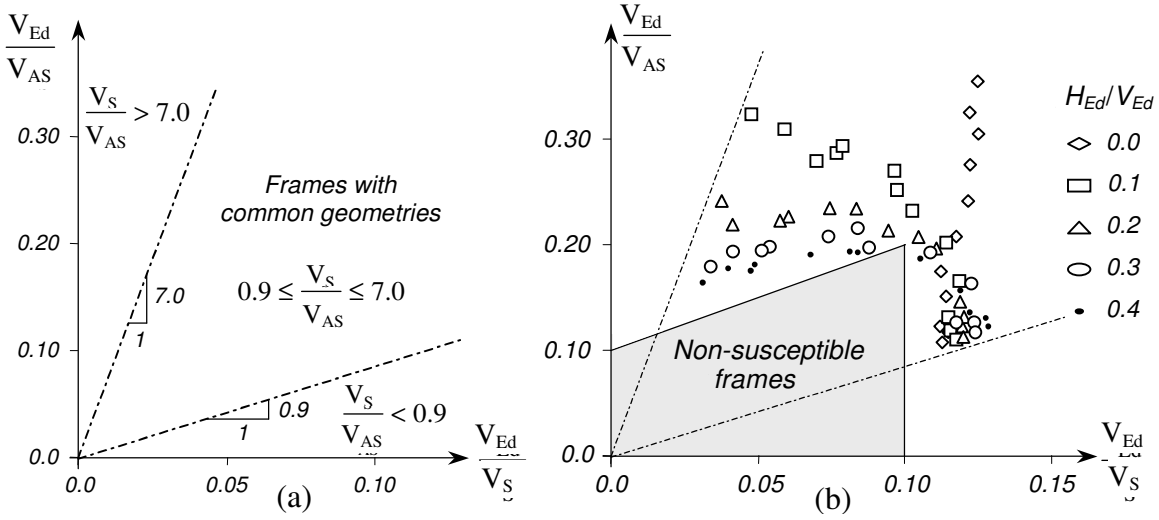

Figure 7: Pitched-roof frame (a) common buckling load ratios and (b) proposed classification criterion

[17] The methodology prescribed by Eurocode involves only V_{Ed}/V_{AS}: a frame classified as "susceptible" or "non-susceptible" to *P-Δ* effects depending on whether $V_{Ed}/V_{AS} > 0.1$ or ≤ 0.1, which means that (i) it is acceptable to underestimate the sway moments by about 11% and (ii) the relative magnitude of the non-sway and sway moments is completely ignored. Even if this last limitation cannot be avoided for arbitrary combinations of frame geometry and loading (it is not possible to quantify the ratio between non-sway and sway moments), it may be overcome in the particular case dealt with in this paper.

$$\frac{V_{Ed}}{V_{AS}} \le 0.1 + \frac{V_{Ed}}{V_S} \qquad \frac{V_{Ed}}{V_S} \le 0.1 \tag{4}$$

are satisfied – they define the shaded area shown in Figure 7(b) and ensure $M_{II.max}/M_{I.max} \le 1.10$. Note that this criterion (i) is quite conservative for many frame geometry-loading combinations and (ii) coincides with that prescribed in Eurocode 3 if symmetric sway buckling is omitted, which amounts to having $V_S = \infty$ – the second condition "vanishes" and the first one becomes equivalent to $\alpha_{cr} \ge 10$.

3. Distortional Behavior of Cold-Formed Steel Members

This section addresses three topics dealing with the non-linear behavior and strength of distortional cold-formed steel columns and beams buckling in distortional modes – recall that such buckling modes, which are critical in intermediate members, involve in-plane and out-of-plane cross-section deformation, combining wall transverse bending with internal edge motions and warping displacements (Figs. 8(a)-(b) show illustrative distortional buckling mode shapes and buckled cross-sections of zed-section columns and beams). The findings reported concern (i) the stable post-buckling asymmetry (a surprising unique phenomenon in bifurcation theory) and (ii) the influence of the end support conditions on the Direct Strength Method (DSM) design of cold-formed steel columns and beams against distortional failures.

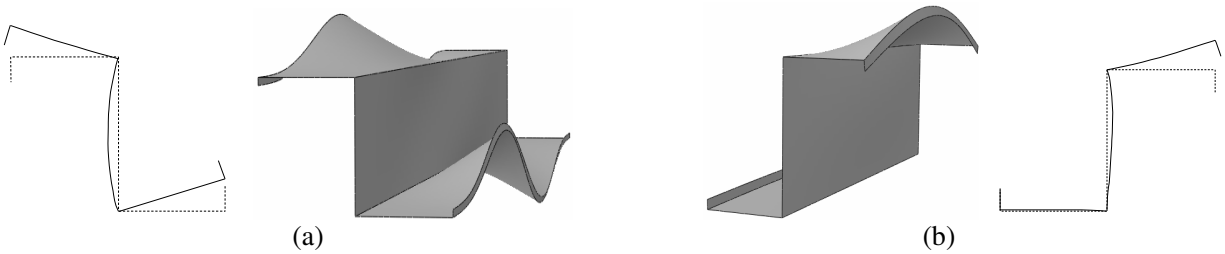

Figure 8: Illustrative distortional buckling mode shapes and buckled cross-sections of zed-section (a) columns and (b) beams

3.1 Post-Buckling Asymmetry

Almost two decades ago, Prola & Camotim (2002a,b) investigated the elastic distortional post-buckling behavior of initially imperfect lipped channel columns and beams, by means of spline finite strip non-linear analysis, and unveiled a highly surprising feature: the post-buckling strength may strongly depend on the (distortional) initial imperfection "sign", *i.e.*, on whether the compressed flange-lip assemblies move inward or outward[18] – in other words, there exists a "distortional post-buckling asymmetry"[19]. Figure 9 illustrates this asymmetry, by showing the equilibrium paths of lipped channel columns (left side) and beams (right side) containing initial geometrical imperfections involving inward and outward motions, respectively – it is clear that the stiffer behavior is associated with inward motions of the compressed flange-lip assemblies[20]. A bit later, Yang & Hancock (2004) provided experimental evidence of this asymmetry, in the context of web-flange-stiffened lipped channel columns. However, these authors reported that the stiffer behavior was associated with outward flange-lip assembly motions, *i.e.*, exactly the opposite that had been found for the plain lipped channel columns.

[18] This finding was obtained virtually "by accident": the "member distortional initial geometrical imperfection sign" was unintentionally changed and the post-buckling equilibrium path obtained differed significantly from the previous one. Until then, it had been tacitly assumed that the distortional post-buckling behavior was stable symmetric (like its local and global counterparts).

[19] This asymmetry is absent in zed-section columns, since one compressed flange-lip assembly moves inward and the other outward (see Fig.8(a)).

[20] The "cross-over" of the two beam equilibrium paths is due to the fact that the major-axis bending deformations "oppose"/"reinforce" the outward/inward compressed flange-lip motion. Thus, the post-buckling behavior associated with the outward compressed flange-lip motion appears stiffer in the early loading stages – this false appearance vanishes when the distortional buckling deformations become large enough.

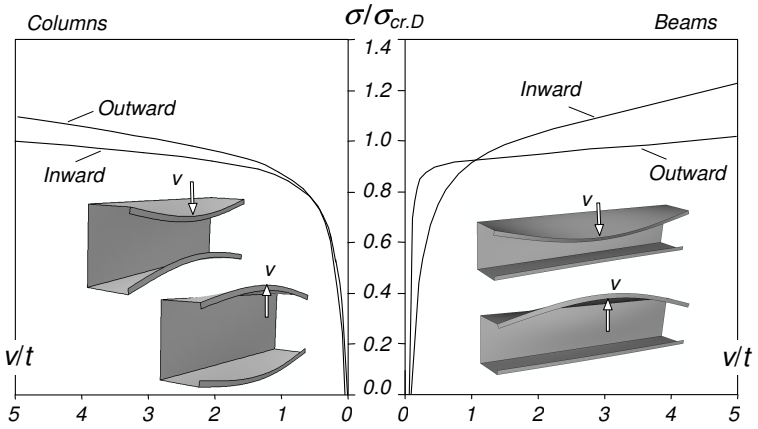

Figure 9: Elastic distortional post-buckling equilibrium paths of lipped channel columns (left side) and beams (right side) containing initial geometrical imperfections involving inward and outward motions of the compressed flange-lip assemblies

A mechanical explanation of the above post-buckling asymmetry and apparent discrepancy between the plain and stiffened lipped channel column behaviors is due to Silvestre & Camotim (2006). These authors performed similar GBT-based geometrically non-linear analyses of plain and web-flange-stiffened lipped channel columns buckling in distortional modes and (i) provided further numerical evidence of the post-buckling asymmetry, (ii) confirmed that this asymmetry is opposite in the columns with the two cross-section shapes (see Fig. 10, which also shows the deformed configurations of the stiffened columns) and, most of all, (iii) explained its origin: the normal stress distribution caused by the distortional deformations, which is opposite in the flanges and lips undergoing outward and inward motions – the post-buckling behavior is more or less stiff depending on whether the (quite high) stresses developing at the flanges and (mostly) lips are tensile or compressive, respectively. Figures 11(a)-(b) and 12(a)-(b), displaying the normal stress distributions (compressions are negative) developing at the plain and stiffened lipped

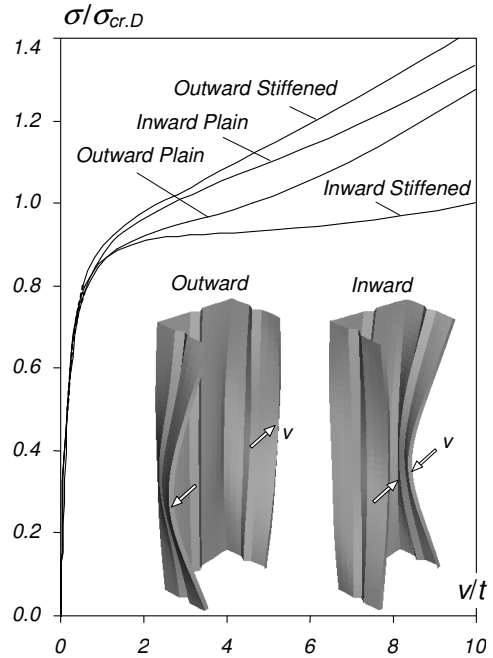

Figure 10: Distortional post-buckling equilibrium paths of plain and stiffened lipped channel columns associated with outward and inward flange-lip assembly motions, and (ii) deformed configurations of the stiffened lipped channel columns

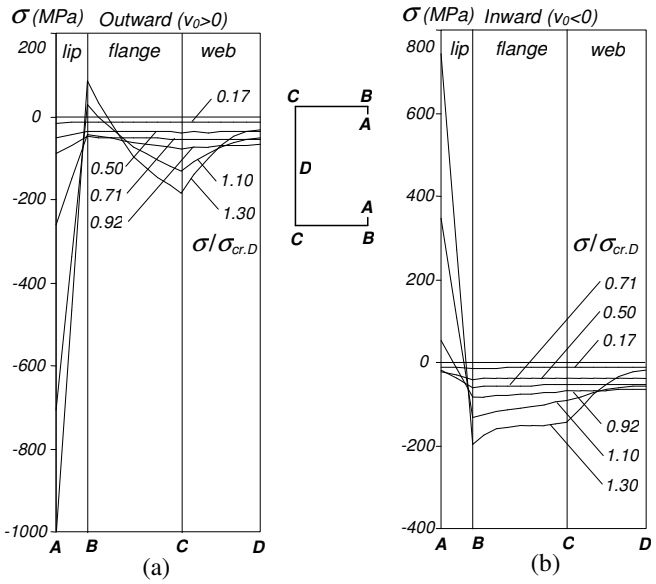

Figure 11: Mid-span normal stress distribution in plain lipped channel columns: (a) outward and (b) inward flange-lip motions

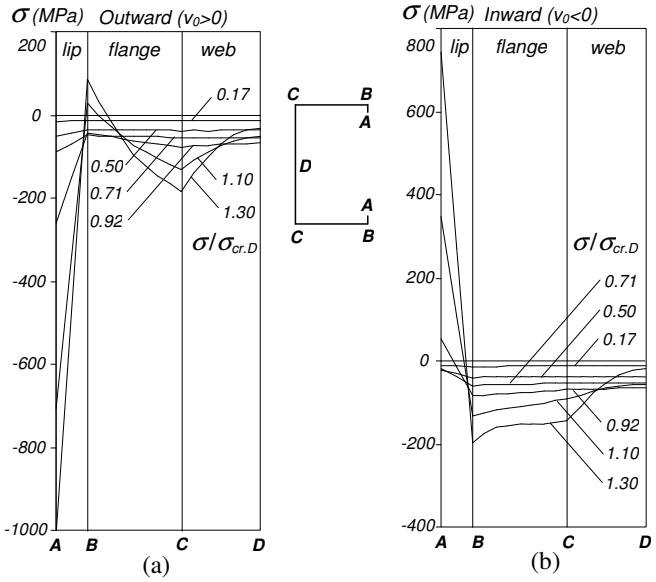

Figure 12: Mid-span normal stress distribution in stiffened lipped channel columns: (a) outward and (b) inward flange-lip motions

channel column mid-span cross-sections, attest the above assertion – note that high tensile or compressive stresses develop at the lip free end regions (the former associated with the stiffer post-buckling behavior in both situations). Naturally, the above post-buckling asymmetry is altered in members buckling in modes with more than one distortional half-wave: it either (i) vanishes, for even half-waves (equal outward and inward half-wave numbers), or (ii) becomes gradually less pronounced, for growing odd half-waves (the outward and inward half-wave numbers get progressively closer) – Figure 13, concerning a lipped channel column buckling in a three half-wave mode, illustrates the latter case.

It is still worth noting the absence of guidelines to predict which flange-lip motions lead to the stiffer post-buckling behavior in members with any given cross-section shape – *e.g.*, in rack-section members the stiffer post-buckling behavior is associated with outward flange-lip motions (Prola & Camotim 2002c).

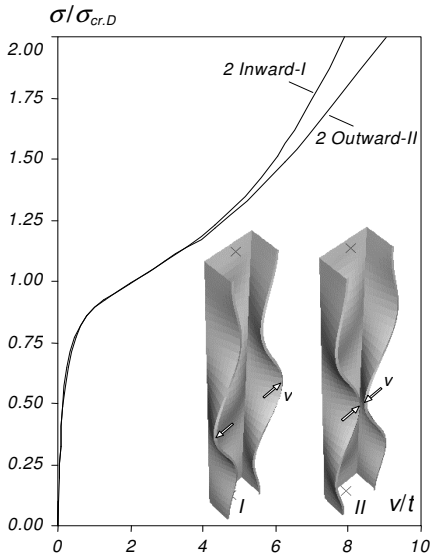

Figure 13: Distortional post-buckling equilibrium paths of plain lipped channel columns buckling in three half-wave modes, two of them exhibiting inward (I) and outward (II) flange-lip motions – the central half-wave "sign" is always "in minority"

3.2 Column DSM Design

In the course of a numerical investigation on the distortional post-buckling behavior and ultimate strength of pin-ended (simply supported) and fixed-ended lipped channel under fire conditions, Landesmann & Camotim (2011) "accidentally" found that, at least for the particular column geometries considered, the accuracy of the failure load estimates, at room temperature, yielded by the current DSM distortional is quite different for pin-ended and fixed columns: while the latter are predicted quite accurately, the former are clearly overestimated, particularly in the intermediate and high slenderness ranges[21]. This surprising finding provided the motivation to investigate whether the column end support conditions influence the safety and accuracy of the ultimate load estimates provided by the current DSM distortional design curve.

Based on distortional failure load data concerning lipped channel (C), hat-section (H), zed-section (Z) and rack-section (R) cold-formed steel columns exhibiting (i) various combinations of geometry and yield stress, and (ii) four end support conditions, namely fixed (F), pinned-fixed (P-F), pinned (P) and fixed-free (F-F) columns, these authors (Landesmann & Camotim 2013) assessed the quality of the corresponding DSM estimates – Figure 14 depicts the distortional failure modes of a representative sample of C-H-Z-R columns. The four plots in Figure 15 make it possible to compare the current DSM distortional design curve with (i) the numerical failure loads of 648 columns (162 per plot, *i.e.*, per end support condition considered)[22] and (ii) the experimental failure loads reported by Schafer (2008), concerning exclusively F columns. The observation of these four plots prompted the following remarks:

[21] Note that the calibration and validation of the current DSM distortional design curve involved almost exclusively columns with rigid plates attached to their end cross-sections. Although Schafer (2005) mentions that "they were tested in the pin-pin condition", this statement concerns the column *global* behavior (the rigid plates usually rest on spherical hinges, knife edges or wedges) – as far as the *distortional* behavior is concerned the columns are fixed. Indeed, it is not easy to test columns with other than fixed supports (*e.g.*, simply supported columns) that fail in distortional modes – it is extremely difficult to ensure that the column end sections are able to warp freely.

[22] It should be pointed out that some F (mostly) and P-F columns exhibit local-distortional interactive failure modes – those with yield stresses high enough to enable the "interference" of local buckling along the distortional post-buckling equilibrium path. However, the "quality" of the associated DSM failure load predictions remains perfectly in line with those concerning the columns exhibiting "pure" distortional failures. At this stage, it is worth noting that it was also recently found that the local-distortional interaction effects are fairly small when the critical local buckling exceeds its distortional counterpart (Martins *et al.* 2017a) Since, for the F and P-F columns analyzed by Landesmann & Camotim (2013), the ratio between these two critical buckling loads varies between 1.17 and 2.29, the above observation is not at all surprising.

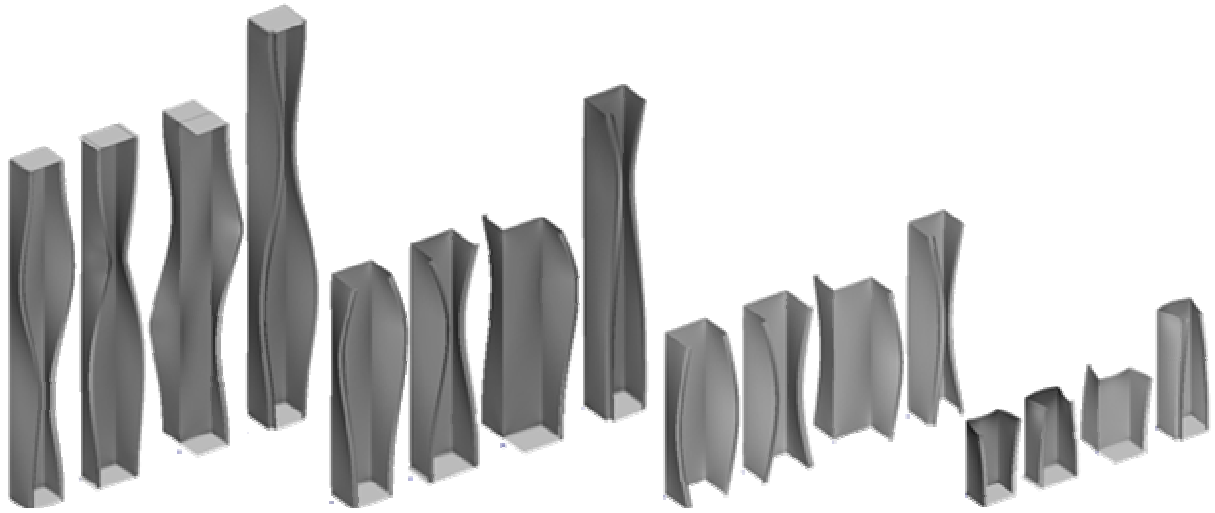

Figure 14: Distortional failure modes of a representative sample of C-H-Z-R columns with the four support conditions considered

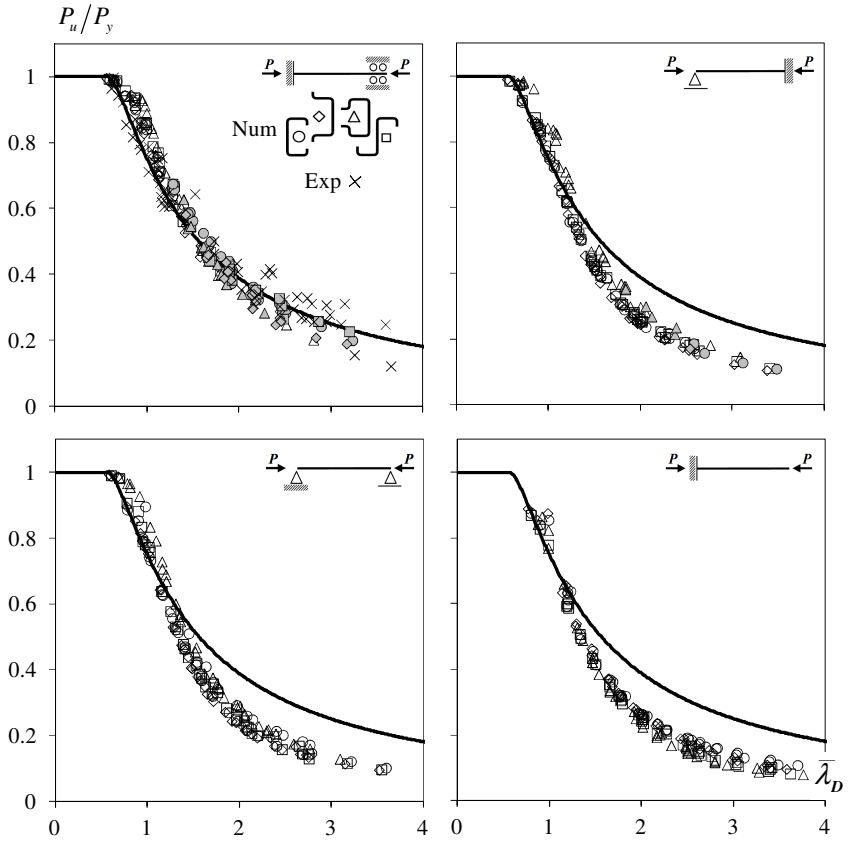

Figure 15: Comparison between the current DSM distortional curve and (i) the F, P-F, P and F-F column numerical failure loads obtained by Landesmann & Camotim (2013) and (ii) the F column experimental failure loads reported by Schafer (2008)

(i) As expected, the DSM design curve provides accurate and mostly safe predictions of the (F column) experimental failure loads. Moreover, it also predicts reasonably well the F column numerical failure loads – the corresponding $P_{n.D}/P_u$ ratio average, standard deviation, maximum and minimum values read 1.02-0.09-1.19-0.75.

(ii) Concerning the P-F, P and F-F columns, it is readily observed that their (numerical) failure loads are excessively overestimated by the DSM design curve in the moderate and high slenderness range ($\lambda_D \geq 1.5$). Accurate (safe or slightly unsafe) predictions only occur for low-to-moderate slenderness.

(iii) Although the DSM curve overestimations are qualitatively quite similar for the three "non-F" column sets, the number of $P_u/P_{n.D}$ values slightly above or below 0.5 grows as one "travels" from P-F to P and F-F columns. It is interesting to notice that the $P_u/P_{n.D}$ ratios below 0.5 do not concern any C column, but mostly H and R pinned columns and H, Z and C fixed-free columns – only one (R) pinned-fixed column falls in this category. The $P_u/P_{n.D}$ averages, standard deviations, maximum and minimum values are 0.83-0.18-1.17-0.48 (P-F columns), 0.79-0.19-1.17-0.45 (P columns) and 0.68-0.19-1.15-0.35 (F-F columns).

(iv) The relevant differences between the F and "non-F" column distortional post-critical strengths are not properly captured by their distortional critical buckling loads. This means that it is necessary to find other DSM-based design curve(s) to predict adequately "non-F" column distortional failure loads.

Guided by the failure load data acquired, Landesmann & Camotim (2013) proposed a (preliminary) additional single DSM design curve ($P^*_{n.D}$), which only modifies the current one for $\lambda_D \geq 1.188$ and retains the failure load prediction accuracy and safety for the less slender columns[23] – it reads

$$P^*_{n.D} = \begin{cases} P_y & for\ \lambda_D \leq 0.561 \\ \left[1 - 0.25\left(P_{cr.D}/P_y\right)^{0.6}\right]\left(P_{cr.D}/P_y\right)^{0.6} P_y & for\ 0.561 < \lambda_D \leq 1.188 \\ \left[0.55 + 0.4\left(P_{cr.D}/P_y\right)^{0.8}\right]\left(P_{cr.D}/P_y\right)^{0.8} P_y & for\ \lambda_D > 1.188 \end{cases} \quad . \quad (5)$$

Figure 16 compares this design curve with the previous P-F, P and F-F column numerical failure loads, and leads to $P^*_{n.D}/P_u$ averages, standard deviations, maximum and minimum values 1.11-0.11-1.41-0.93 (P-F columns), 1.10-0.10-1.39-0.95 (P columns) and 1.11-0.12-1.52-0.91 (F-F columns) – to avoid overestimating the failure loads of a few very slender ($\lambda_D > 2.0$) F-F columns, the design curve clearly underestimates many slender ($\lambda_D \geq 1.5$) P-F, P and F-F column failure loads. Further developments on this topic must be preceded by the performance of carefully planned experimental investigations.

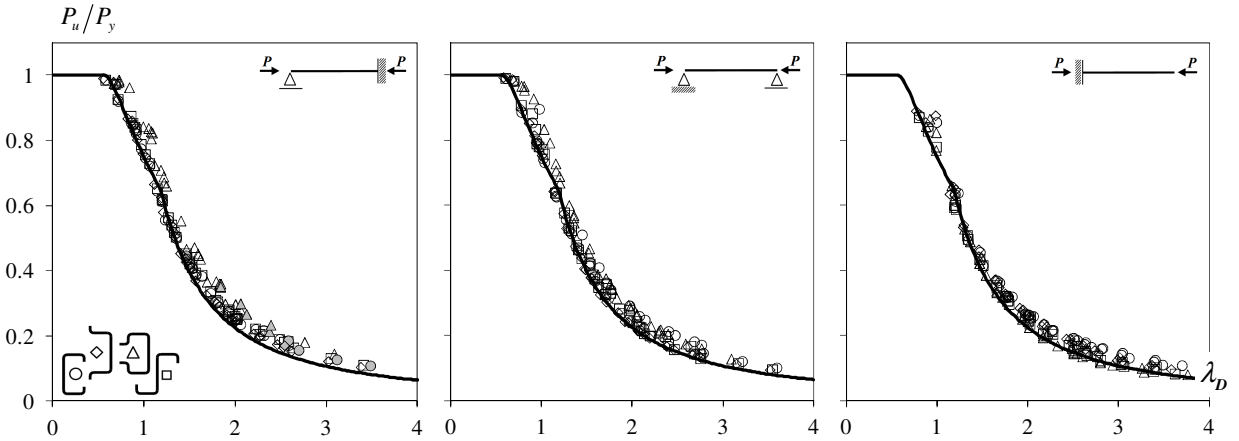

Figure 16: Comparison between the DSM distortional curve proposed by Landesmann & Camotim (2013) and the P-F, P and F-F column numerical failure loads obtained by these authors

[23] For simplicity, a single design curve covering P-F, P and F-F columns was sought – a further refinement is possible for the P-F and P columns.

3.3 Beam DSM Design

The current DSM distortional design curve was developed essentially on the basis of experimental failure moment data concerning 4-point bending tests, involving uniformly bent beam segments (i) laterally restrained, (ii) with "warping continuity" at their end cross-sections, *i.e.*, end support conditions lying in-between "free warping" and "prevented warping", and (iii) exhibiting small-to-moderate distortional slenderness ($\lambda_D \leq 1.5$) (Yu & Schafer 2006, Schafer 2008). More specifically, these failure moments were reported by 17 researchers who tested (i) lipped channel beams bent about the major-axis, (ii) zed-section beams under skew bending (axis parallel to the flanges) and (iii) hat-section and trapezoidal beams (with or without intermediate stiffeners) bent about the minor-axis. Figure 17, adapted from Schafer (2008), plots, against the local or distortional slenderness, the 574 normalized failure moments considered to develop the current local and distortional beam DSM design curves. In this figure, $\lambda_{max}=(M_y/M_{cr})^{0.5}$, where M_{cr} is the beam critical/lowest (local or distortional) buckling moment – this "mixed slenderness" was used because to difficulties in distinguishing between local and distortional failures, due to the bracing and support conditions. These difficulties led Schafer to perform tests on beams designed to exhibit clear local (Yu & Schafer 2003) and distortional (Yu & Schafer 2006) failures. However, the latter beams exhibited again small-to-moderate distortional slenderness values (between 0.68 and 1.53). In view of what was mentioned above, it is not surprising that the current DSM beam distortional design curve (M_{ND}) yields quite good estimates for beams such that $\lambda_D \leq 1.5$.

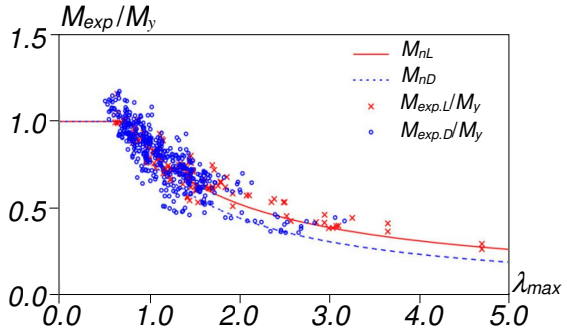

Figure 17: DSM beam local and distortional design curves and experimental local/distortional failure moments (Schafer 2008)

Recently, numerical simulations reported by Landesmann & Camotim (2016) provided solid evidence that M_{ND} overestimates the failure moments of simply supported lipped channel beams with intermediate and high slenderness values. They also showed that the amount of overestimation depends on the beam cross-section geometry (dimension ratios) and end support conditions. Moreover, very recent work on the distortional post-buckling behavior of simply supported lipped channel beams (Martins *et al.* 2018a) has shown that minor-axis flexural and torsional deformations emerge at the vicinity of the critical distortional buckling moment level and gradually grow as loading progresses – they stem from the stress redistribution occurring in the compressed/top half cross-section, caused by the increasing distortional deformations. Restraining (reducing) these flexural-torsional deformations, which are intrinsic to the distortional post-buckling behavior and responsible for the associated beam rapid stiffness erosion, certainly leads to a failure moment increase. Therefore, these authors concluded that the discrepancy between the numerical distortional failure moments and their DSM-based predictions stems from three features of the specimens tested to obtain the experimental failure moments used to develop the M_{ND} strength curve: (i) low-to-intermediate slenderness values ($\lambda_D \leq 1.5$), (ii) warping restraint and (iii) lateral restraint.

The above facts led Martins *et al.* (2017b) to carry out a detailed numerical investigation on the behavior of simply supported uniformly bent cold-formed steel beams exhibiting different cross-sections shapes

and failing in pure distortional modes. This study involved over 4000 beams with three cross-section shapes, namely (i) lipped channels bent about the major-axis (C), (ii) zed-sections under skew bending causing uniform flange compression (worst case) (Z), and (iii) hat-sections subjected to either major-axis (H_M) or minor-axis (H_m) bending (compressed lips in the latter case) – Figures 18(a)-(d) show the various cross-section shapes, buckled in beam distortional modes. Two end support conditions were considered, differing in the warping and local displacement/rotation restraints, either completely free (SCA) or fully prevented (SCB) – see Figures 19(a)-(b). The beams analyzed had several cross-section dimension ratios and lengths, in order to assess their influence on the distortional post-buckling behavior and ultimate strength – particular attention was paid to (i) the web-flange and flange-lip width ratios[24], and (ii) the critical (distortional) half-wave number. In addition, the beams had different yield stresses, making it possible to cover wide slenderness ranges (0.25-4.00 intervals).

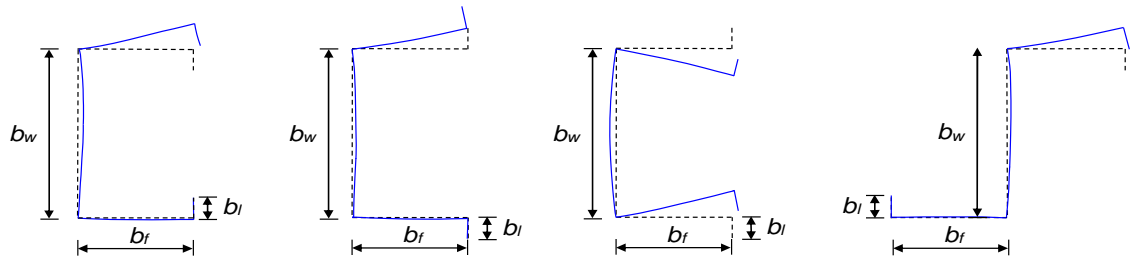

Figure 18: Uniformly bent beam cross-sections buckled in distortional modes: (a) lipped channel (major-axis bending), (b) hat-section (major-axis bending), (c) hat-section (minor-axis bending) and (d) zed-section (skew bending – horizontal neutral axis)

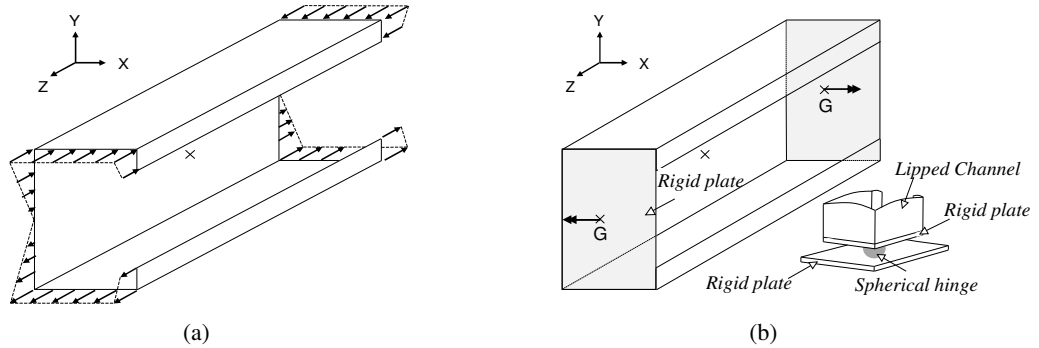

Figure 19: Loading and (a) SCA and (b) SCB support conditions of the beams analyzed by Martins *et al.* (2017b)

This investigation showed that the elastic and elastic-plastic distortional post-buckling behaviors of SCA and SCB beams sharing the same geometry and yield stress are markedly distinct in stiffness and strength. For instance, unlike their SCB beam counterparts, the non-stocky SCA beams exhibit practically no elastic-plastic strength reserve and, therefore, their failure moments are fairly well predicted by the elastic buckling strength curve. Moreover, it was also clearly shown/confirmed that (i) the current DSM distortional design curve is unable to predict adequately the failure moments of both the SCA and SCB simply supported beams analyzed by Martins *et al.* (2017b) with intermediate and high slenderness, (ii) the same DSM-based design curve cannot handle the two beam support conditions considered and (iii) beams bent about the major and minor axis must be treated separately. Therefore, it was necessary to develop novel DSM strength curves to provide better quality predictions of all the numerical failure moments available. This was done by means of the following procedure:

[24] In the context of columns, Silvestre *et al.* (2005) showed that the cross-section dimensions influence the distortional post-buckling behavior.

(i) Definition of the initial "plateau", on the basis of the numerical failure moment data concerning the stocky beams, whose collapse is governed exclusively by plasticity (negligible instability effects) – it was decided to keep the plateau of the current curve (λ_D=0.673).

(ii) Determination of a "Winter-type" curve, cast in the form[25]

$$M_{ND} = \begin{cases} M_y + (1 - C_{yd}^{-2})(M_p - M_y) & \lambda_D \le 0.673 \\ (1 - a\lambda_D^{-b})\lambda_D^{-c} M_y & \lambda_D > 0.673 \end{cases} , \quad (6)$$

where parameters a, b and c are obtained from the solution of an optimization problem.

It was found that the failure moments of the C, H_M and Z beams with the same end support conditions may be estimated through single design curves defined by a=0.28, b=1.60, and c=1.85 (SCA beams) or a=0.25, b=1.40, and c=1.40 (SCB beams). On the other hand, the H_m beams must be handled separately, by means of design curves defined by a=0.27, b=1.70, and c=1.92 (SCA beams) or a=0.30, b=1.60, and c=2.10 (SCB beams). Figures 20(a)-(d) compare the obtained M_U/M_y values, concerning SCA and SCB C+H_M+Z and H_m beams[26] with the current and proposed DSM distortional design curves. Their close observation prompts the following remarks:

(i) Almost all M_U/M_y values are well aligned along "Winter-type" curves with a small "vertical dispersion" (although more pronounced in the SCB beams).

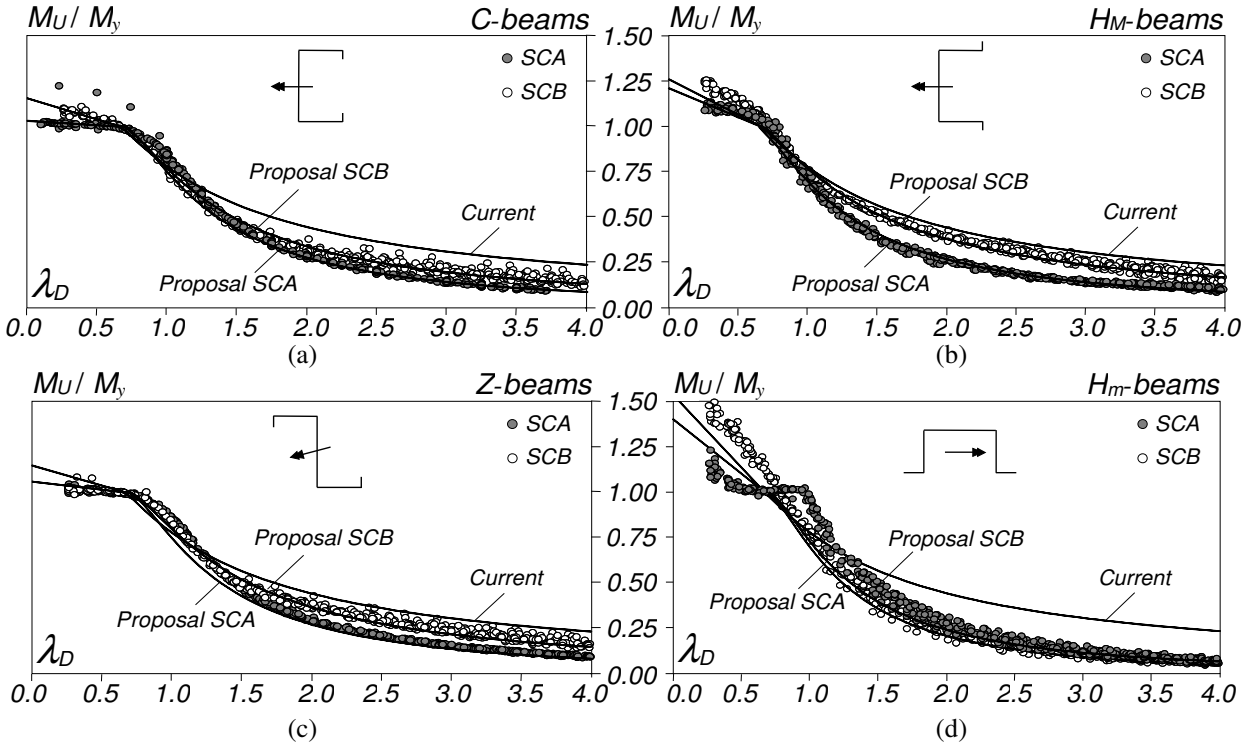

Figure 20: Comparison between the obtained M_U/M_y values, concerning (a) C, (b) H_M, (c) Z and (d) H_m beams, and the current and proposed DSM design curves

[25] Following the work carried out by Shifferaw & Schafer (2012), the strength curve initial horizontal plateau was replaced by an inclined straight line in the latest version of the North-American specification (AISI 2016), thus accounting for the beam cross-section inelastic strength reserve.

[26] For each beam geometry selected, 17 distortional slenderness values were generated randomly, following a continuously uniform distribution in the interval [0.25,4].

(ii) As anticipated, the current DSM design curve provides very large failure moment overestimations for beams with moderate and high slenderness (λ_D>1.25), including the SCB beams – the H_M+SCB M_U/M_y values are those lying closer to this curve.

(iii) The consideration of the inelastic strength reserve for $\lambda_D \leq 0.673$, recently included in AISI (2016), may lead to unsafe designs, particularly in Z-beams. In fact, the work of Shifferaw & Schafer (2012), which is at the root of this design feature, dealt only with C and Z-beams with end support conditions simulating those exhibited by the central beam segment in a 4-point bending test arrangement. While the C+SCB beam results evidence the presence of an additional strength reserve, the same is not true for their Z-beam counterparts – note also that the Z-beams analyzed in this work have their top flanges uniformly compressed, a more severe loading condition. As for the H_M and H_m beams (SCA and SCB), they exhibit a non-negligible inelastic strength reserve, naturally higher in the SCB beams.

(iv) Concerning the SCA beams, it is noted that, for λ_D>1.0 and regardless of the beam type, the M_U/M_y values are fairly well predicted by the elastic buckling curve $(1/\lambda_D)^2$. This is because failure is reached almost simultaneously with the onset of yielding (no visible elastic-plastic strength reserve is available), making it logical that the elastic buckling curve provides good failure moment estimates.

(v) A clear failure moment prediction is achieved by the proposed design curves, along the whole distortional slenderness range considered, as attested by the associated M_U/M_{ND} value statistical indicators: averages, standard deviations, maximum and minimum values of 1.13-0.11-1.59-0.90 (C+H_M+Z SCA beams), 1.09-0.12-1.54-0.83 (C+H_M+Z SCB beams), 1.11-0.13-1.34-0.84 (H_m SCA beams) and 1.10-0.07-1.20-0.86 (H_m SCB beams).

(vi) The "vertical dispersion" is much higher in the SCB beams, due to the different post-critical strength reserve exhibited by the various beam types – such strength reserve is absent in all SCA beams.

(vii) The proposed DSM design curves are more adequate than the current one to estimate the failure moments of simply supported beams failing in distortional modes. However, it is recognized that there is dependence on the cross-section dimensions and length (through the critical distortional buckling mode half-wave number) that cannot be explicitly accounted by the DSM without "soiling" its roots and elegance, since such dependence cannot be captured only by the distortional slenderness – this implies unavoidable excessive failure moment underestimations.

Lastly, Figure 21(a) revisits Fig. 17 and adds the two strength curves proposed by Martins *et al.* (2017b), thus making it possible to compare the quality of their experimental failure moment predictions with that of the current strength curve. Figure 21(b), on the other hand, plots, against the λ_D, the experimental and numerical failure moments reported by Yu & Schafer (2006). The observation of these results shows that:

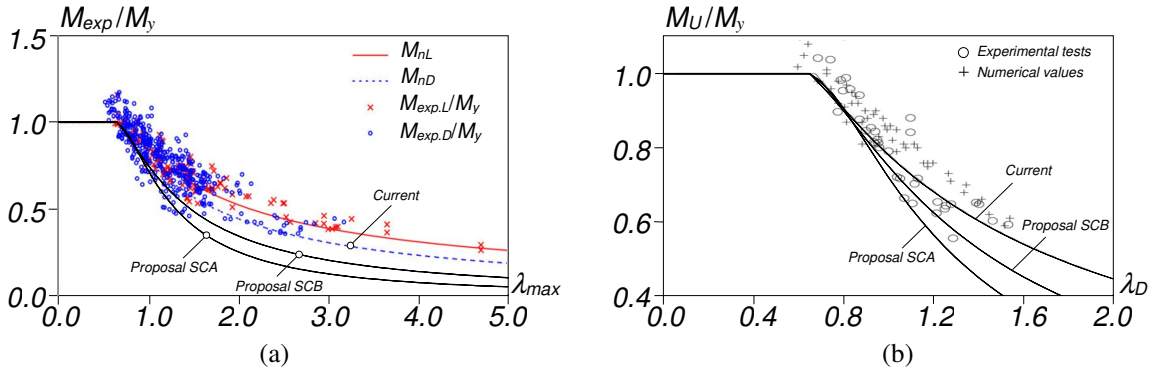

Figure 21: DSM beam distortional design curves (current and proposed) and experimental distortional failure moments (a) used to develop the current strength curve and (b) reported by Yu & Schafer (2006) (both figures adapted from Schafer 2008)

(i) The overwhelming majority of the tests results considered to calibrate the current strength curve are also fairly well predicted by the two proposed curves, even if a bit more on the safe side for λ_D>1.0 (see Fig. 21(a)). Most of these test results concern rather stocky beams, for which the failure moment predictions yielded by the current and proposed strength curves differ by small amounts.

(ii) The two proposed curves underestimate considerably the failure moments of a small number of reasonably slender beams – this may be due to the bracing arrangement adopted in the tests, which restrains lateral-torsional deformations (in the central span) that are intrinsic to the distortional post-buckling behavior, thus leading to higher failure moments.

(iii) Figure 21(b) readily shoes that the two proposed design curves underestimate a considerable fraction of the experimental results reported by Yu & Schafer (2006) by larger margins than the current strength curve. However, note that none of these results concerns beams with slenderness above 1.5, the range for which the current strength curve has been shown to be inadequate. Moreover, there is a quite significant variability in the experimental test results, mostly likely due to the influence of the cross-section dimensions on the ultimate strength of these beams.

Finally, one last word to mention that further developments on this topic, namely the codification of an improved DSM beam distortional design curve, must be preceded by experimental studies – experimental test campaigns focusing on slender beams (λ_D>1.5) failing in distortional modes are clearly needed.

4. Lateral-Torsional Stability of Web-Tapered Beams

Tapered members are widely used in the steel construction industry, because of their (i) structural efficiency (leading to significant material savings), (ii) ability to meet architectural and functional demands and (iii) competitive fabrication costs. However, designers can only take full advantage of the benefits of beam tapering if they are able to accurately predict the tapered member structural behavior, without needing to resort to computer effort prohibitive for routine applications.

The structural behavior of most laterally unrestrained beams, either prismatic or tapered, is governed by lateral-torsional stability/buckling (LTB), which combines minor-axis bending and torsion. For the sake of uniformity and ease-of-use, it is desirable to have design methodologies valid for both prismatic and tapered beams. In order to achieve this goal, the most "logical" approach is to modify the currently codified rules and procedures for prismatic beams, extending their range of validity to tapered beams. One crucial aspect is the need to have efficient (*i.e.*, as accurate and "simple" as possible) methods to evaluate the elastic critical load factor of any given tapered beam, indispensable step to determine its normalized slenderness. Andrade & Camotim (2005) proposed a one-dimensional model to analyze the elastic LTB behavior of singly symmetric tapered thin-walled open beams, which can be viewed as an extension of Vlassov's theory (applicable to prismatic bars) – subsequently, the model was extended to account for the influence of the pre-buckling deflections (Andrade & Camotim 2004). The elastic critical load factors and corresponding buckling modes provided by this model, numerically implemented by means of the Rayleigh-Ritz method and later put to test to corroborate its underlying assumptions and LTB predictions (Andrade *et al.* 2007), made it possible to show that:

(i) The LTB behaviors of prismatic and tapered beams are, in general, qualitatively different. Indeed, a certain geometrical feature of tapered beams (see Section 4.1) makes it impossible to capture their LTB behavior by analyzing piecewise prismatic beams – the results of the latter do not converge to the solution of the former, regardless of the number of prismatic segments considered.

(ii) For a specific beam (tapered) geometry and loading conditions, the minimum buckling resistance is not necessarily associated with the beam containing the least amount of material.

Next, the paper briefly addresses the one-dimensional model to analyze the elastic LTB behavior of singly symmetric tapered thin-walled open beams that was originally developed and subsequently validated and improved by Andrade & Camotim (2004, 2005) and Andrade *et al.* (2007, 2010), focusing on the specific geometrical and mechanical characteristics exhibited by web-tapered beams. Then, a few illustrative numerical results are presented and discussed, highlighting the most surprising and "non-intuitive" features associated with the LTB behavior of this type of beams.

4.1 One-Dimensional Model

The central objective of any beam theory is to achieve a one-dimensional characterization (*i.e.*, have the parameter of a certain curve as the only independent variable) of the behavior of bodies with two characteristic dimensions much smaller than the third one (the length). The need for tractable and accurate lower-dimensional theories stems from the formidable mathematical obstacles (analytical and numerical) posed by the three-dimensional continuum models. Nevertheless, it must be emphasized that beam models are intrinsically approximate, since the actual bodies dealt with are three-dimensional. The so-called technical/engineering beam theories are typically obtained by incorporating a set of *a priori* assumptions into a three-dimensional continuum model. Such assumptions, which concern mostly the "form" of some unknowns (displacement/stress components), are more or less realistic and always lead to simplifications, even if some inconsistencies may possibly arise.

Next, the assumptions underlying the one-dimensional model developed and numerically implemented by Andrade & Camotim (2004, 2005), to characterize the elastic LTB behavior of singly symmetric tapered thin-walled open beams (see Fig. 22(a)) are briefly presented. Note that thin-walled open beams have a wall thickness an order of magnitude smaller than the cross-section mid-line length and resist torsion as a spatial system: the cross-sections exhibit out-of-plane warping, generally varying along the beam axis and, thus, causing non-negligible longitudinal normal strains and stresses. First, it is assumed that both the strains and displacement derivatives are small (negligible with respect to unity) and the tapered beam is (i) made of a St. Venant-Kirchhoff material (Young's modulus E and Poisson's ratio ν) and (ii) subjected to the generic system of conservative loads depicted in Figure 22(b), which act initially on the undeformed beam plane of symmetry and are proportional to a single load factor λ.

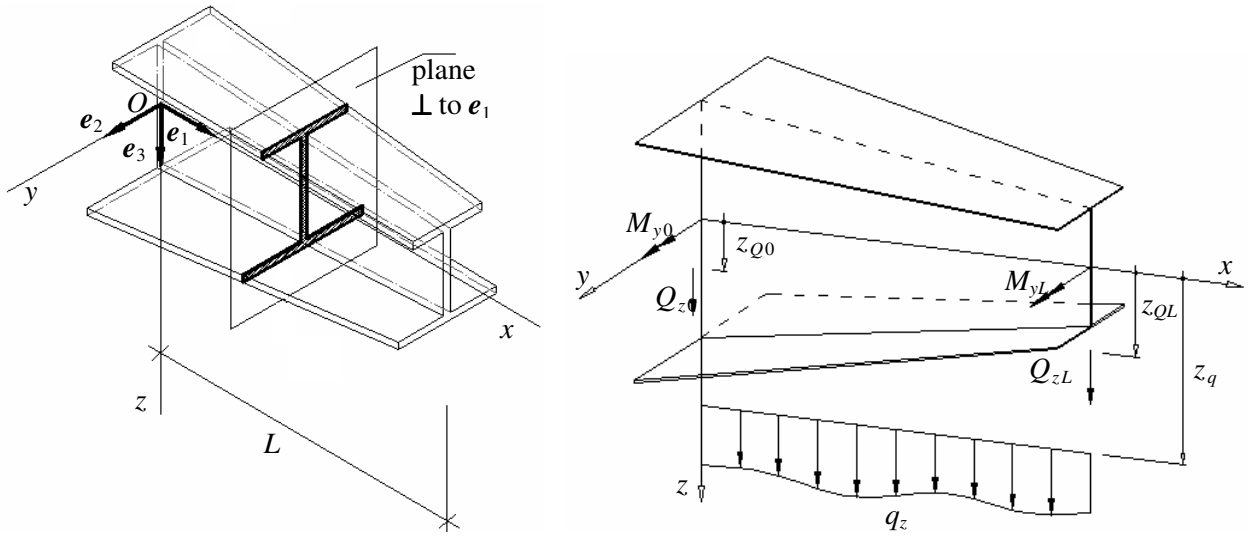

(a) (b)

Figure 22: Symmetric tapered I-section beam (a) geometry and (b) generic external conservative loading

The beams are regarded as membrane shells, upon which the following kinematical constraints are imposed: (i) the projection of each cross-section mid-line on a plane perpendicular to the beam axis experiences no distortion throughout the whole deformation process and (ii) the mid-surface shear strains are negligible. These kinematical constraints extend, to tapered beams, the classical Vlassov's hypotheses commonly adopted in prismatic thin-walled open beams. Note that the first constraint inevitably implies that the beam is constrained to buckle in a "pure" global mode (LTB), *i.e.*, the transverse motion of any given cross-section mid-line is described by rigid-body kinematics – it may be broken down into a rotation Φ about $\boldsymbol{e}_1$, followed by a translation with components V and W along $\boldsymbol{e}_2$ and $\boldsymbol{e}_3$, respectively (see Fig. 22(a)). As for the second constraint, it enables expressing the mid-line displacements along $\boldsymbol{e}_1$ as a function of V, W, Φ, to within an uniform longitudinal displacement U. Concerning the beam strain energy, which is the sum of the membrane and uniform torsion strain energies, it is worth noting that the latter contribution, completely disregarded in the membrane shell model, is added separately by means of the expression valid for prismatic beams, but accounting for the variation of the cross-section property J along the beam axis – this procedure is backed by both theoretical and experimental evidence (Lee & Szabo 1967).

The taper effect is dealt with through (i) additional, non-standard, mechanical properties $EI^*_{\omega\psi}$ and EI^*_{ψ}, and (ii) a modification of the minor-axis bending and warping rigidities by a "reduced flange thickness" $t^*_f = t_f \cos^3\varphi$, where φ is the flange slope, related to the web taper parameter α through the relation $\mathrm{tg}\,\varphi=(1-\alpha)h_0/L$ (h_0 and L: reference web height and beam length) – asterisks identify the tapered beam properties. To help grasping the physical meaning of the above properties, Figures 23(a)-(f) show a comparison between the linearized warping-torsion behaviors of prismatic and web-tapered doubly symmetric I-beams (Andrade *et al.* 2010). The following aspects deserve to be specially mentioned:

(i) In both cases, the linearized version of the aforementioned constraints, together with symmetry considerations, imply qualitatively similar cross-section mid-line displacement fields (see Fig. 23(a)): (i_1) the mid-line rotates ϕ about the centroidal x-axis and (i_2) the flanges warp out of the plane, by rotating $\pm(h/2)\,\phi_{,x}$ about the z-axis. To reach this conclusion, recall that, in web-tapered beams, (i_1) the displacements along z are obviously *not* orthogonal to the flange mid-planes, as shown in the zoomed detail in Figure 23(a), and (i_2) the flange centroidal lines are not parallel to the x-axis, which implies that the derivatives with respect to these line arc-lengths and to x are not identical. Denoting the former and latter by $(\cdot)_{,s}$ and $(\cdot)_{,x}$, respectively, the two are related by $(\cdot)_{,s}=\pm\cos\varphi\,(\cdot)_{,x}$ – the sign depends on the flange centroidal line slope (recall that $h_{,x}=-2\,\mathrm{tg}\,\varphi$).

(ii) The above displacement field can then be used to obtain the flange membrane extensions – see Fig. 23(b). Comparing the ensuing strain-displacement relations for prismatic and web-tapered beams, it is readily observed that the latter contain a corrective factor ($\cos^2\varphi$) and an additional term. The same holds for the flange normal membrane forces, as shown in Figure 23(c).

(iii) The flange membrane shear forces displayed in Figure 23(d) may be determined by considering the equilibrium of a "flange slice" acted by the previously obtained flange membrane normal forces.

(iv) The membrane normal (shear) forces are statically equivalent to a bending moment (shear force) in each flange – see Figures 23(e)-(f). In web-tapered beams, the modified warping stiffness EI^*_{ω}, calculated with the reduced flange thickness $t^*_f = t_f \cos^3\varphi$, and the non-standard mechanical property $EI^*_{\omega\psi}$ arise naturally from this static equivalence.

(v) Finally, note that, in web-tapered beams, the flange bending moments have an axial component that (v_1) features $EI^*_{\omega\psi}$ and EI^*_{ψ}, and (v_2) contributes to the total torque. This added torque contribution is obviously absent in prismatic beams (see Fig. 23(e)) and cannot be captured if a web-tapered beam is replaced by a piecewise prismatic one (regardless of the number of segments considered).

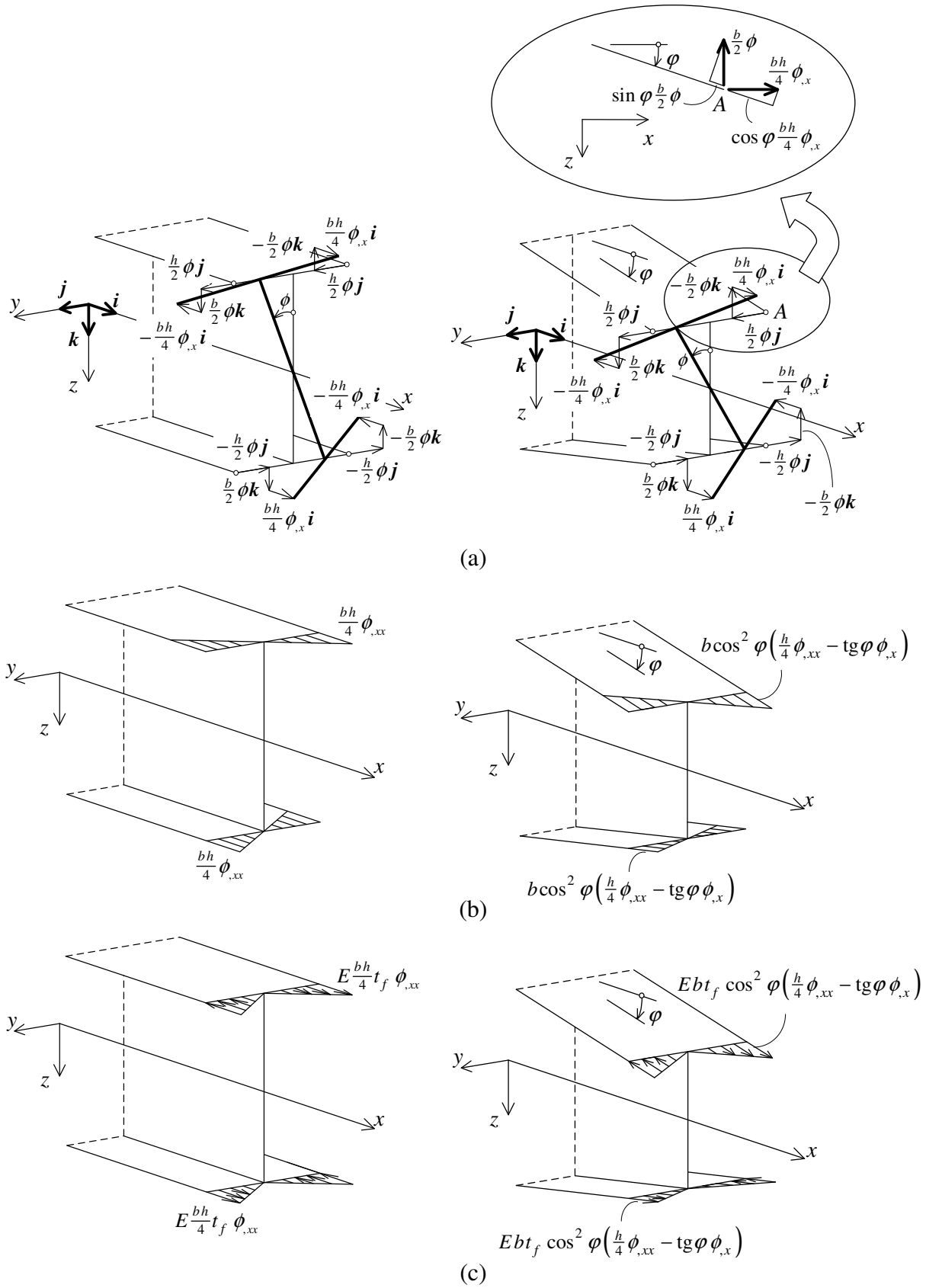

Figure 23: Linearized warping-torsion behaviors of prismatic and web-tapered doubly symmetric I-beams compared: (a) linearized cross-section mid-line displacement field, (b) flange membrane extensions and (c) flange membrane normal forces (Andrade *et al.* 2010)

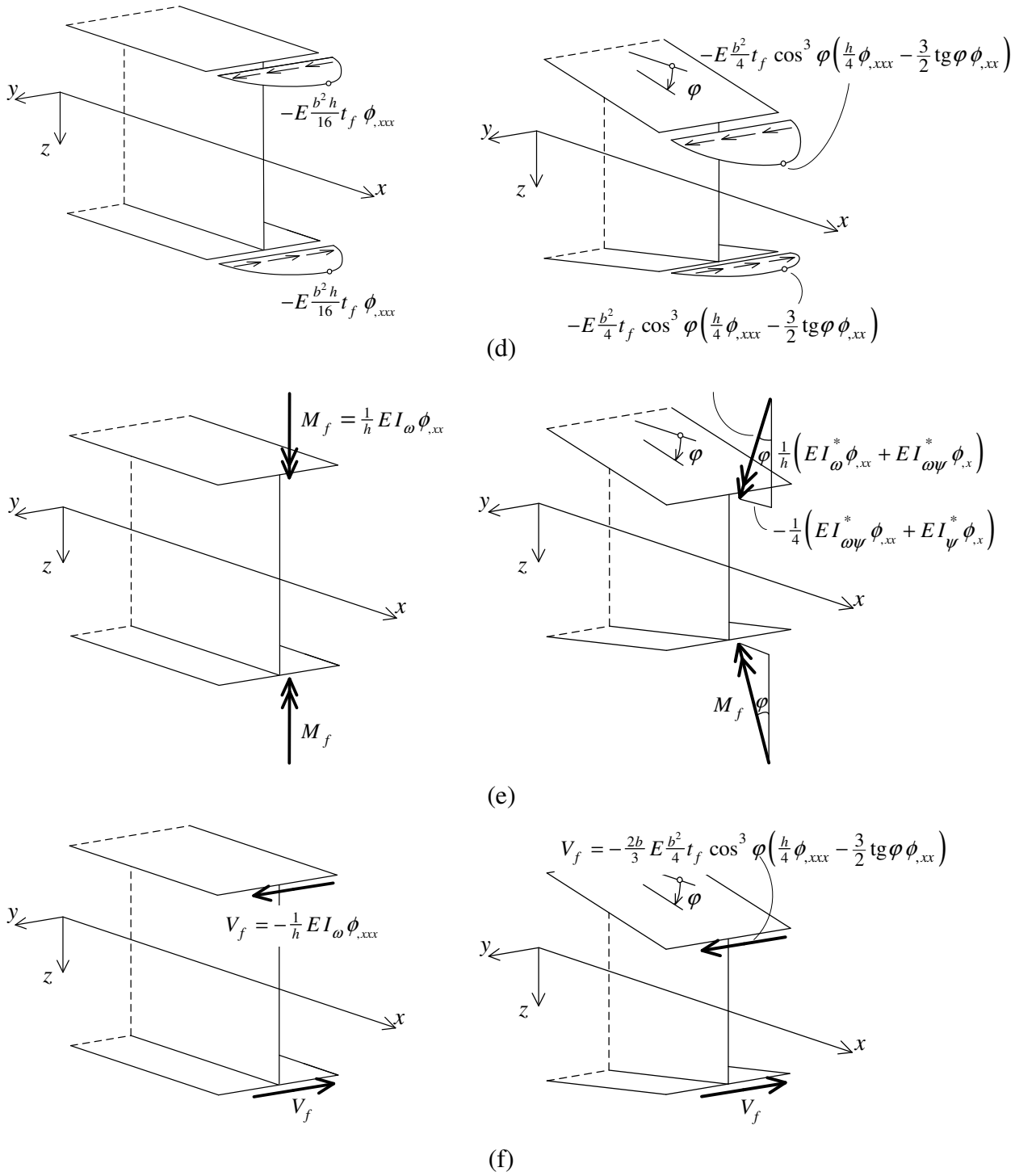

Figure 23 (cont.): Linearized warping-torsion behaviors of prismatic and web-tapered doubly symmetric I-beams compared: (d) flange membrane shear forces, (e) flange bending moments M_f and (f) flange shear forces V_f (Andrade *et al.* 2010)

4.2 Illustrative Numerical Results

In order to illustrate the application and capabilities of the one-dimensional model developed and numerically implemented, the paper presents and discusses a set of critical moments M_{cr} concerning the web-tapered I-section simply supported beam displayed in Figure 24, which (i) has uniform flanges

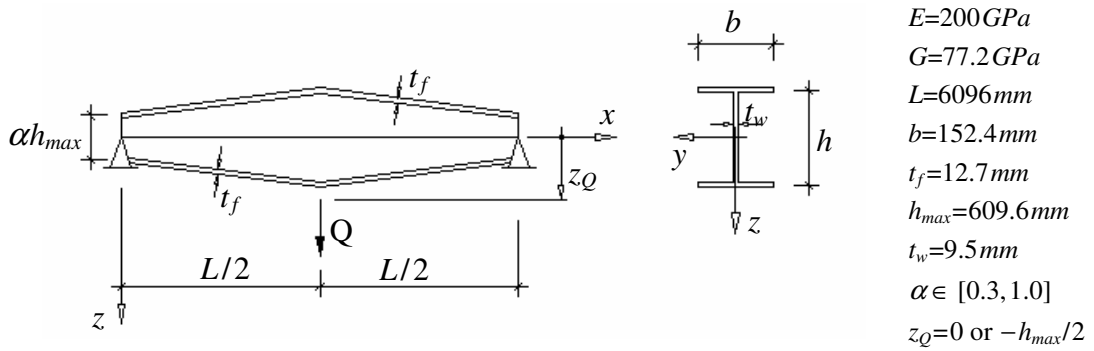

Figure 24: Simply supported beam geometry, loading and material constants

and a linearly tapered web of constant thickness, and (ii) is acted by a mid-span vertical point load applied at either the web mid-height or the top flange mid-line (Andrade & Camotim 2005). The beam (i) has two longitudinal planes of symmetry (equal flanges and symmetric tapering slopes) and (ii) exhibits different tapering parameter values α (ratio between the mid-span and end cross-section web heights, measured between flange mid-lines). Since the x and polar axes are chosen to be coincident and defined by the intersection of the two longitudinal symmetry planes, they contain the line segment uniting the cross-section centroids and shear centers (in the undeformed configuration), which means that S_y^* (and z_G^*), $I_{\omega z}^*$, $I_{\psi z}^*$ and β_y^* are identically zero.

Two different analyses were performed: (i) one employing the one-model model developed specifically for web-tapered beams and (ii) the other equivalent to a prismatic beam FE analysis (adopting a fine enough mesh). It is still worth noting that only half a beam is analyzed, due to the following symmetries with respect to $x=L/2$: (i) undeformed beam configuration, (ii) loading and (iii) critical buckling mode – this last symmetry implies that only odd-number shape function terms need to be retained. The curves presented in Figure 25 show the variation of $Q_{cr}=4M_{cr}/l$ with the tapering parameter α. The observation of these curves, and their comparison with results reported in the literature, leads to the following comments:

(i) When the one-dimension model developed/implemented is employed, the two curves Q_{cr} *vs.* α (i_1) are clearly non-linear, (i_2) virtually coincide with those available in the literature (Yang & Yau 1987,

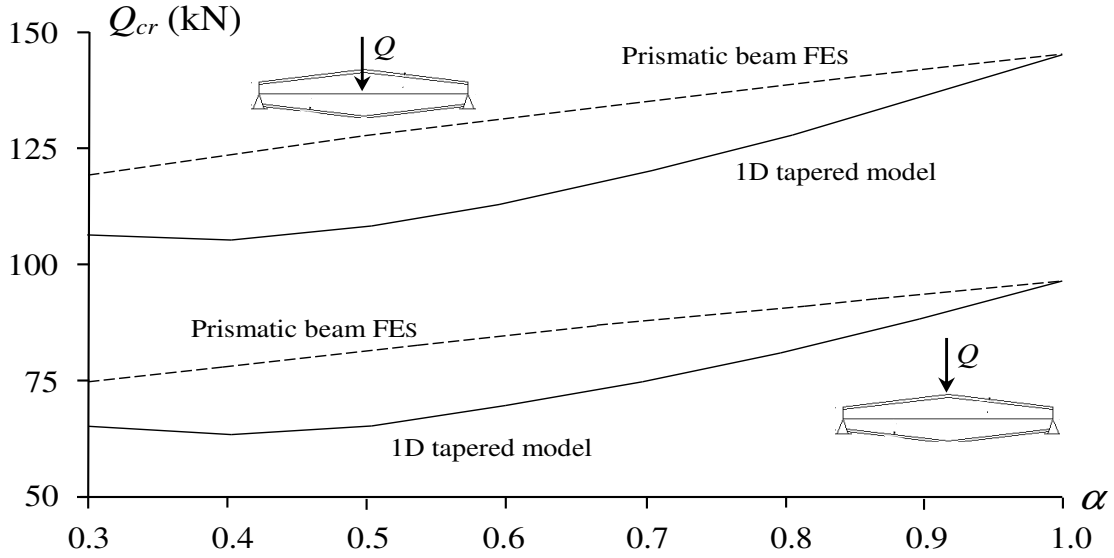

Figure 25: Variation of Q_{cr} with α for the simply supported beams analyzed

Boissonnade & Muzeau 2001[27]) and (i_3) exhibit a minimum value for $\alpha \approx 0.4$ – this last observation means that the beam with the least amount of material does not have the minimum Q_{cr}. This surprising last result can be explained by the variation of the stiffness values as α increases: while (i_1) the average values of GJ, EI_{ω}^{*}, $EI_{\omega\psi}^{*}$ *increase*, (i_2) EI_{ψ}^{*}, constant along the x-axis, *decreases* and (i_3) EI_{z}^{*} remains *constant* – as a result of the joint influence of the above two conflicting variations, the minimum Q_{cr} value occurs for an intermediate α value.

(ii) When a prismatic beam FE analysis is carried out, (ii_1) the variation of Q_{cr} with α becomes almost linear and (ii_2) the correct Q_{cr} value is considerably overestimated – the error goes up to about 25%, for $\alpha = 0.5$ and top flange loading.

(iii) The Q_{cr} values are significantly reduced when the load is applied at the top flange ($z_Q < 0$), a well-known effect in prismatic beams that is due to the additional destabilizing torque (about the shear center line) exerted in the adjacent configuration.

(iv) In order to achieve convergence to the results displayed in Figure 25, it was necessary to approximate the critical buckling mode by means of between 2 and 12 shape functions. It was found that, when the tapering effects are fully taken into account, the rate of convergence gradually decreases as the flange slope increases. On the other hand, when the prismatic beam FE model is used, the flange slope does not affect convergence.

5. Generalized Beam Theory (GBT)

It seems very fair to argue that I am the recipient of the 2018 Lynn S. Beedle Award mostly due to the research activity carried out at the University of Lisbon on Generalized Beam Theory (GBT) in the last 15 years, which contributed decisively to the "scientifically resurrection" and worldwide dissemination of this theory among the technical/scientific community working with thin-walled members and structural systems, particularly cold-formed steel ones[28]. Indeed, this unique approach to the structural analysis of prismatic thin-walled members had significant impact in the academic world and provided great impetus for many research efforts "inspired" by the GBT modal concepts and procedures – this assertion can be readily attested by the growing number of publications on a wide variety of topics that either are devoted to develop new GBT formulations/applications or use GBT-based results/approaches to tackle particular structural engineering problems[29].

Although the available GBT formulations and applications cover (i) different types of structural analysis (first-order, buckling, post-buckling, vibration, dynamic), (ii) several materials (carbon steel, stainless steel, aluminum, steel-concrete composite, FRP composites), mainly modeled by means of elastic or elastic-plastic constitutive laws, (iii) thin-walled profiles with distinct cross-section shapes (open, closed, arbitrary flat-walled, curved) and (iv) various structural elements/systems (isolated members, continuous beams, trusses, frames), this paper addresses only work dealing with the two structural analyses most related to the SSRC activity (buckling and post-buckling analyses) and all the illustrative numerical results presented concern (i) the buckling behavior of isolated members or simple frames and (ii) the post-buckling behavior of isolated steel members, always involving open cross-sections. In addition, a few paragraphs are devoted to the *cross-sections analysis*, which constitutes the first step and "trademark" of a

[27] The last authors only analyzed beams acted by loads applied at mid-height.

[28] A procedure initiated a few years earlier by Prof. J. M. Davies, at the Universities of Salford and Manchester (Camotim *et al.* 2004).

[29] About 10 years ago, an overwhelming majority of the publications addressing or using GBT originated from the University of Lisbon. This situation has drastically changed in the last few years, following the fast growth of the amount of research word devoted to or involving GBT – even if the number the publications on GBT coming from the University of Lisbon has not diminished, nowadays they are only a decreasing fraction of the total number (as it should be).

GBT analysis[30], and leads to the determination of cross-section *deformation modes* with well-defined structural/mechanical meanings.

5.1 Cross-Section Analysis

As just mentioned, the purpose of the *Cross-Section Analysis* is to obtain the cross-section deformation modes and associated mechanical properties through a systematic procedure – its most recent version, applicable to arbitrary flat-walled cross-sections, has been described in detail by Gonçalves *et al.* (2014) and Bebiano *et al.* (2015). After specifying the cross-section nodal discretization, involving (i) natural intermediate, (ii) natural end and (iii) intermediate (user-defined) nodes, the associated deformation modes and corresponding mechanical properties are automatically computed – they may be grouped into 3 main families: (i) Vlassov modes, with null membrane transverse extensions and shear strains, (ii) Shear modes, with non-null membrane shear strains (and null transverse extensions) and (iii) (linear) Transverse Extension modes, with non-null membrane transverse extensions (these families can still be further divided into three sub-families each –see Table 2).

Table 2: GBT deformation mode families and sub-families

Family	Sub-family	Mechanical characteristics
Vlassov	*Global*	4 classic rigid-body modes (extension, major/minor-axis bending and torsion). In cross-section with closed cells, the torsion mode integrates the cell shear flow sub-family
	Distortional	Warping and wall transverse bending, including in-plane fold-line displacement
	Local	Only wall transverse bending (no fold line displacements)
Shear	*Global*	Warping shear deformations
	Cell Shear Flow	Constant shear flows on the cross-section cells (including torsion)
	Local	Localized warping shear deformations
Transverse Extension	*Global*	Wall transverse extensions
	Distortional	Transverse extensions and closed cell distortions
	Local	Localized transverse extensions

Figure 26 shows the deformation modes of a lipped channel, corresponding to the nodal discretization indicated, which involves 21 nodes, namely 4 natural intermediate, 2 natural end and 13 intermediate (9 in the web, 3 in the top flange, 1 in the bottom flange and none in the lips). This discretization is intended for the local post-buckling analysis of a beam subjected to positive major-axis bending (Martins *et al.* 2018b), which explains why (i) the web is heavily discretized and (ii) the top flange has more intermediate nodes than the bottom one – naturally, a discretization intended to analyze the post-buckling behavior of a lipped channel column is symmetric with respect to the major-axis. It is worth noting that Figure 26 includes quadratic transverse extensions modes, which are needed to overcome membrane locking problems and do not stem from the cross-sections analysis procedure (Gonçalves & Camotim 2012) – each of them involves a single wall segment and makes it possible to account more accurately for the "bowing effect" associated with the transverse bending of that wall segment.

Depending on the particular problem under consideration, the user may select any sub-set of deformation modes to be included in the structural analysis, making it possible to (i) reduce the number of degrees of freedom and (ii) specify the nature of the deformations to be considered. This last capability is particularly

[30] The performance of a GBT structural analysis of a thin-walled member involves (i) the *cross-section analysis*, leading to the determination of the deformation mode shapes and corresponding modal mechanical properties, and (ii) the *member analysis*, which consists of solving the equilibrium equation system governing the behavior under consideration.

Figure 26: Lipped channel nodal discretization and most relevant displacements of the (ii) Vlassov and Transverse Extension (linear and quadratic), and (iii) Shear deformation modes

useful when employing the DSM to design cold-formed steel members, since it is necessary to determine buckling loads/moments associated with "pure" local, distortional or global modes. Finally, one last word to mention that the most recent version of the freely available GBT-based code GBTUL[31] (Bebiano *et al.* 2018a) performs the cross-sections briefly outlined in this section.

5.2 Buckling Analysis

The buckling results presented and discussed in this section are intended to illustrate GBT developments dealing with loading and support conditions, extension to structural systems, namely frames, and design applications – these developments are first succinctly described (a more detailed account can be found in Camotim & Basaglia 2013). Concerning the loading conditions, the developments make it possible to

[31] Acronym for "**G**eneralized **B**eam **T**heory at the **U**niversity of **L**isbon".

perform rigorous GBT buckling analyses of members subjected to loadings (i) causing non-uniform internal force and moment diagrams, namely variable bending and/or torsional moments, and (ii) including transverse forces applied away from the cross-section shear center – the locations of the such forces points of application are known to heavily influence the beam buckling behavior and, moreover, may be responsible for localized buckling phenomena (*e.g.*, web crippling). In this case, the differential equilibrium equation system governing the member buckling behavior must include terms that account for the geometric stiffness stemming from the pre-buckling (non-uniform) (i) longitudinal normal stresses, (ii) shear stresses and (iii) transverse normal stresses (Bebiano *et al.* 2007, Basaglia & Camotim 2013). Figure 27 displays all the pre-bucking stresses that are taken into account in the most general GBT buckling analyses – their accurate determination requires the performance of preliminary GBT first-order analyses, usually including all the deformation modes (unlike the ensuing buckling analyses, often carried out with only a fraction of the deformation modes determined) (Bebiano *et al.* 2018b).

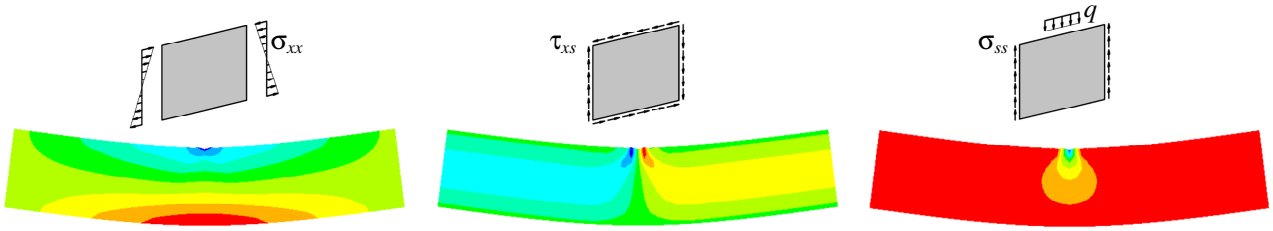

Figure 27: Pre-buckling stresses incorporated in the geometric stiffness of the most general GBT buckling analysis: non-uniform longitudinal normal stresses (σ_{xx}), shear stresses (τ_{xs}) and transverse normal stresses (σ_{ss})

Concerning the support conditions, (i) continuous members (with intermediate supports) and (ii) members exhibiting arbitrary combinations of global and/or local displacement or rotation restraints can now be analyzed. Indeed, it is possible to handle members with rigid or flexible localized supports, thus enabling the simulation of bracing systems and/or discrete connection arrangements (*e.g.*, bolted connections) – Figure 28 illustrates localized support conditions that can be modelled with GBT (Camotim *et al.* 2008). These localized supports are incorporated into the buckling analysis through constraint conditions involving displacements or rotations of member points and expressed in "modal language" – the buckling eigenvalue problem is then solved subject to the satisfaction of those constraint conditions.

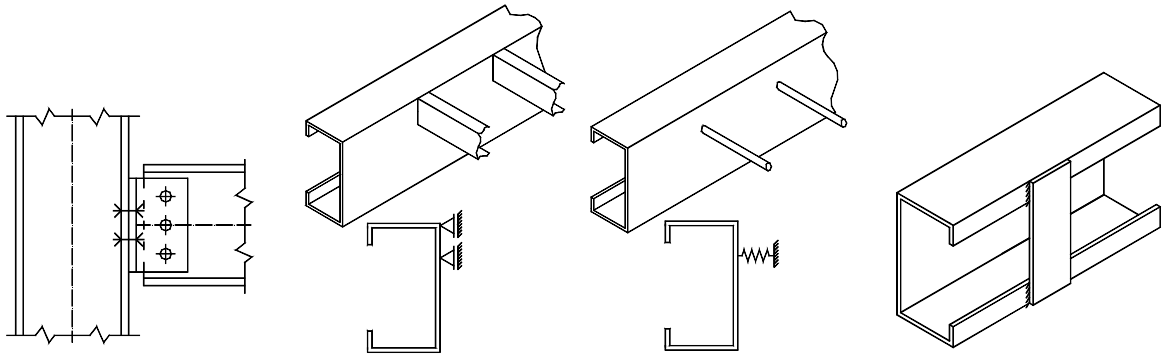

Figure 28: Localized supports modeled with GBT: (a) bolted connections, (b) rigid/flexible bracings, and (c) batten plates

The possibility of analyzing the buckling behavior of thin-walled reticulated structures, such as trusses or frames, constitutes another significant GBT advance. When addressing structural systems formed by members with distinct orientations, it is necessary to model rigorously the displacement compatibility

between the two (or more) end cross-sections converging at a structural system joint – in the case of the warping displacements due to torsion, such compatibility is ensured through the "warping transmission" concept (Basaglia *et al.* 2012). The performance of this task requires (i) transforming the *modal* degrees of freedom of the connected end cross-sections into generalized *nodal* displacements of the point where the joint is deemed materialized (often the intersection of the connected member centroidal axes), which can be done by resorting to a "joint element" concept (Basaglia *et al.* 2008), and (ii) establishing restraint conditions to simulate the compatibility between the displacements, due to wall transverse bending and cross-section distortion, at the connected end cross-sections (Basaglia *et al.* 2009). In thin-walled frames, kinematic models were developed to simulate the structural behavior of joints (i) connecting two or more I, U and C-section members, and (ii) exhibiting the various configurations depicted in Figure 29 – unstiffened, diagonal-stiffened, box-stiffened and diagonal+box-stiffened connections.

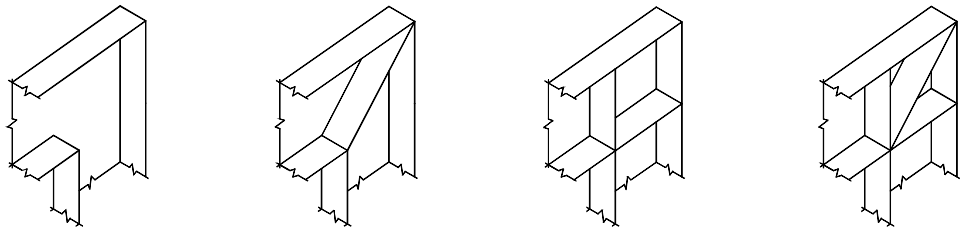

Figure 29: Localized supports modeled with GBT: (a) bolted connections, (b) rigid/flexible bracings, and (c) batten plates

Some of the most recent cold-formed steel design codes (*e.g.*, AISI 2016) either allow or prescribe the determination of a thin-walled member ultimate strength by means of the Direct Strength Method (DSM – *e.g.*, Schafer 2008, Camotim *et al.* 2016). Since its application requires knowing the member critical buckling loads/moments, as well as the nature of the associated buckling modes, GBT is ideally suited to equip designers with easy-to-use tools to obtain accurate buckling results. In this context, it is worth noting the derivation of analytical formulae to obtain approximate (but accurate) distortional buckling loads and moments of cold-formed steel lipped channel, zed-section and rack-section columns, beams and beam-columns with four support conditions (Silvestre & Camotim 2004a-c) – the formulae are based on buckling analyses involving one (columns) or two (beam and beam-columns) deformation modes and Figure 30 illustrates this concept for lipped channel beam-columns. Moreover, as already mentioned, the computer code GBTUL (Bebiano *et al.* 2018a) has been continuously developed in the last few years and is freely available at *http://www.civil.ist.utl.pt/gbt/*.

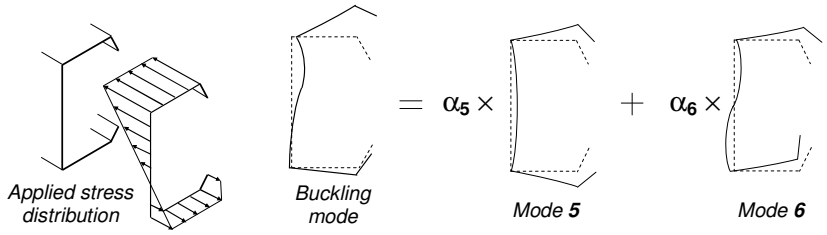

Figure 30: Lipped channel beam-column distortional buckling mode: linear combination of the GBT deformation modes **5** and **6** (symmetric and anti-symmetric distortion)

5.2.1 Illustrative numerical results

The illustrative numerical results presented and discussed concern the buckling behavior of (i) a two span I-section beam (Basaglia & Camotim 2013) and (ii) an L-shaped frame built with lipped channel members

(Camotim *et al.* 2010). For validation purposes, most GBT-based critical buckling loadings and mode shapes are compared with values yielded by ANSYS shell finite element analyses.

The symmetric two-span beam (i) has length L=400*cm* (2×200*cm*) and an I-section with web height h_w=300*mm*, flange width b_f=150*mm* and wall thickness t=5*mm*, and (ii) is acted by two identical mid-span

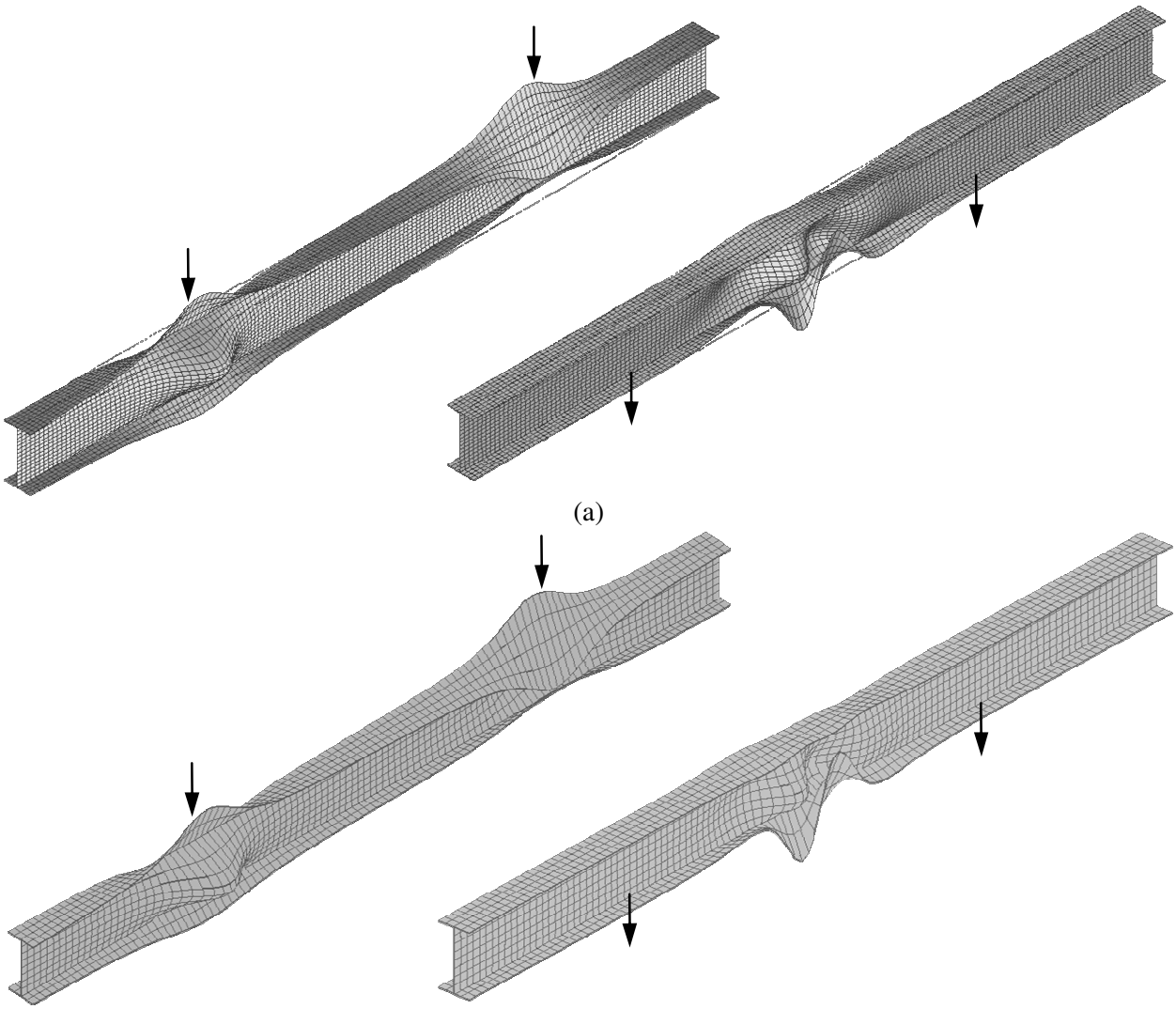

Figure 31: Two-span beam with top and bottom loading: critical buckling mode shapes yielded by (a) ANSYS and (b) GBT analyses, and (c) GBT modal amplitude functions

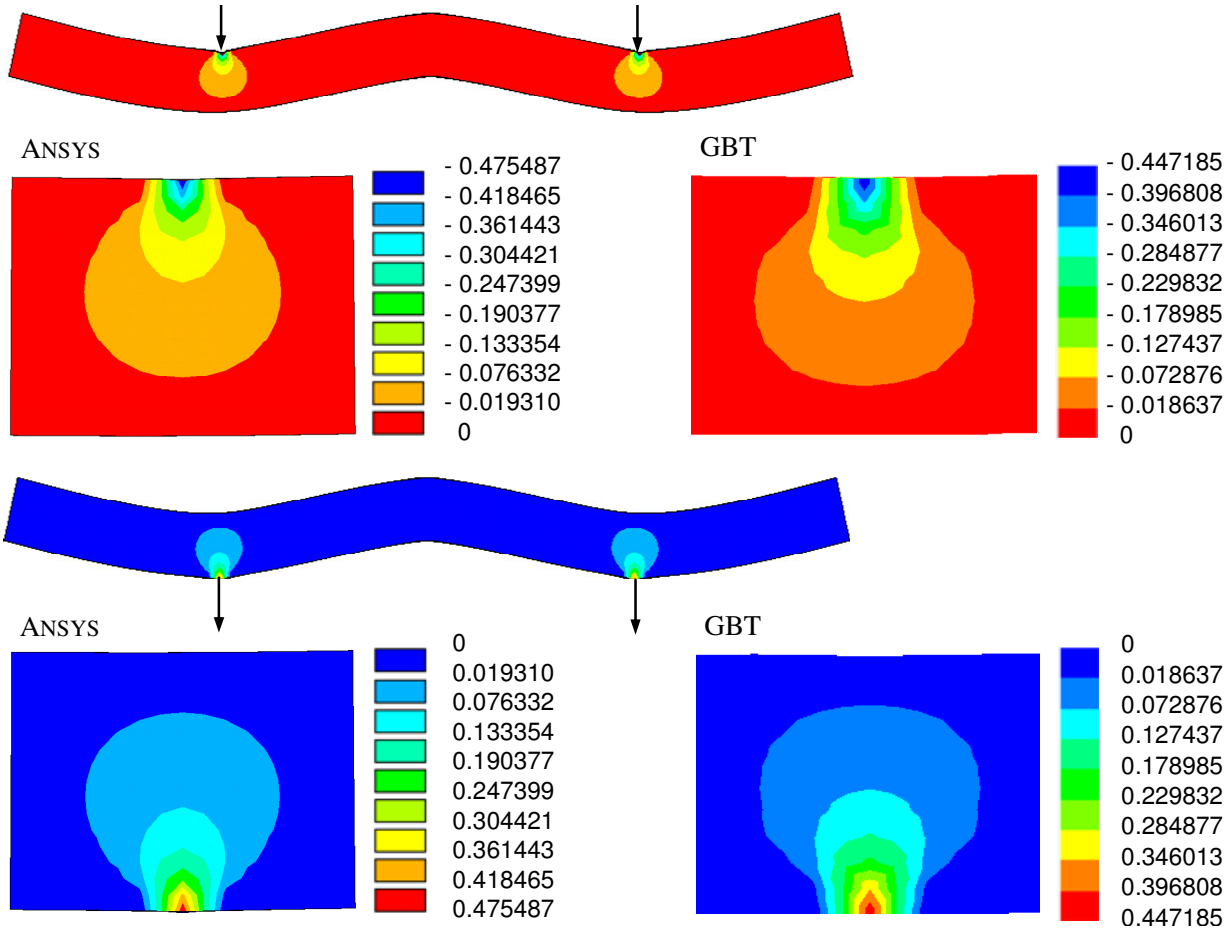

Figure 32: ANSYS and GBT mid-span region pre-buckling transverse normal stresses caused by top and bottom flange loading

transverse point loads F, applied at either the top or bottom flange-web corner. Concerning the support conditions, (i) the end sections are locally/globally pinned and can warp freely, and (ii) all in-plane cross-section displacements are fully restrained at the intermediate support. The critical buckling loads obtained are F_{cr}=250.96kN (GBT) and F_{cr}=244.69kN (ANSYS), for top flange loading, and F_{cr}=644.37kN (GBT) and F_{cr}=652.56kN (ANSYS), for bottom flange loading – differences of +1.75% and −1.26%, respectively. Figures 31(a)-(c) display three representations of the two beam critical buckling modes: (i) ANSYS and GBT 3D views, and (ii) GBT amplitude functions concerning the participating deformation modes ($\phi_k(x)$). It is observed that the two buckling mode representations are remarkably similar (recall that the GBT views in Fig. 31(b) are 3D representations of buckling modes yielded by *beam* finite element analyses). The closeness between the critical buckling loads and modes obtained from the ANSYS and GBT analyses stems from the ability of the latter in capturing the pre-buckling web transverse normal stresses accurately – Figure 32 shows these stress distributions, in the beam mid-span region, as provided by the ANSYS and GBT first-order analyses. Finally, the GBT results show that the local deformation modes (**5**,**6**,**7**,**10**,**11**) have visible contributions to the beam critical buckling modes – while the instability of the beam loaded at the top flange is triggered by localized web buckling occurring close to the loaded cross-sections, that of the beam loaded at the bottom flange is governed by the local deformation of the web and compressed flange local near the intermediate support.

The L-shaped frame analyzed is formed by two orthogonal lipped channel members A and B (L_A=70cm and L_B=105cm) with identical cross-sections (web height h_w=200mm, flange width b_f=120mm, lip width

b_f=15*mm* and wall thickness t=0.7*mm*) and exhibits the geometry and loading displayed in Figure 33. The members are connected with flange continuity and acted by axial compressive forces only: $N_A=P$ and $N_B=0.5P$. The end supports of members *A* and *B* are (i) fixed with prevented warping and (ii) pinned (locally and globally) with free warping, respectively.

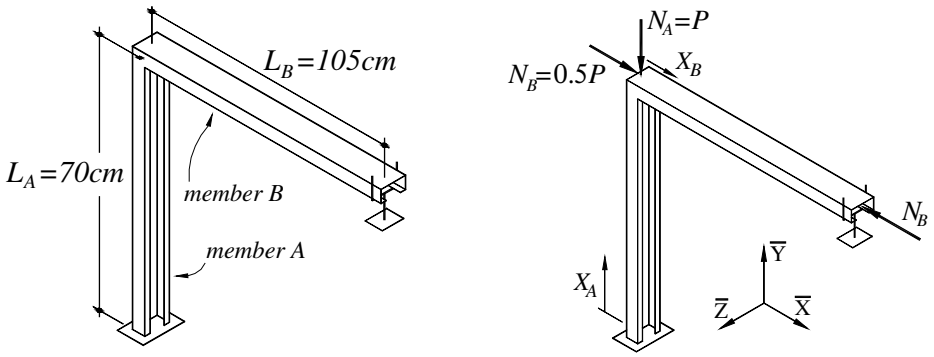

Figure 33: L-shaped frame: geometry, loading and boundary conditions

While Figures 34(a)-(b) display the corresponding representations obtained by means of GBT and ANSYS analyses, Figure 35 provides the member *A* and *B* modal amplitude functions describing the frame critical buckling mode – note again that Figure 34(a) is a 3D representation of *beam* finite element results. The two frame critical buckling loads practically coincide again: P_{cr}=4.177*kN* (GBT) and P_{cr}=4.196*kN* (ANSYS) – 0.45% difference, even if the numbers of degrees of freedom involved are orders

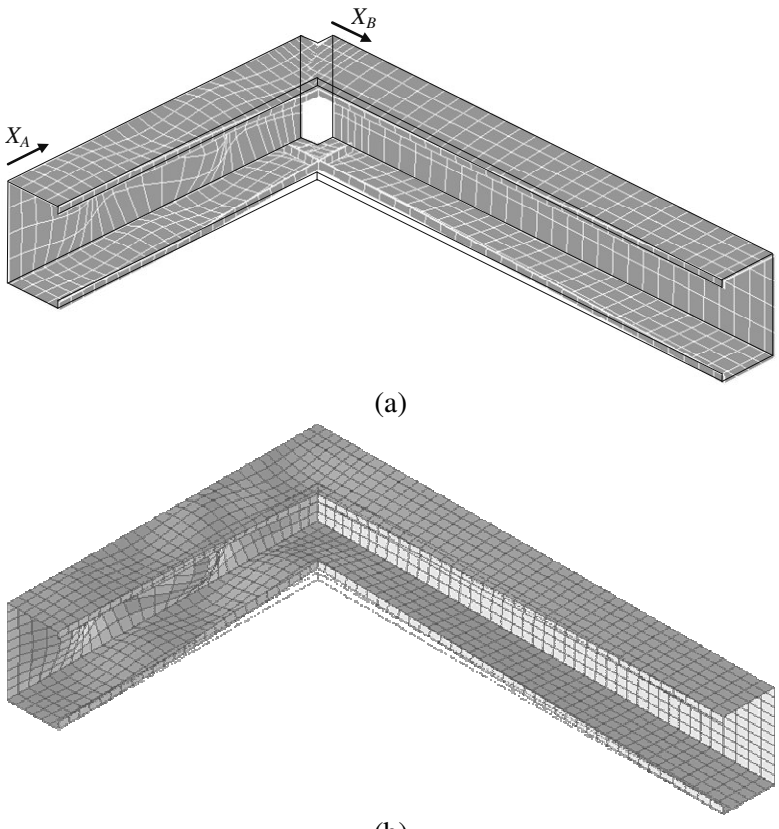

Figure 34: L-shaped frame: (a) GBT and (ii) ANSYS 3D critical buckling mode representations

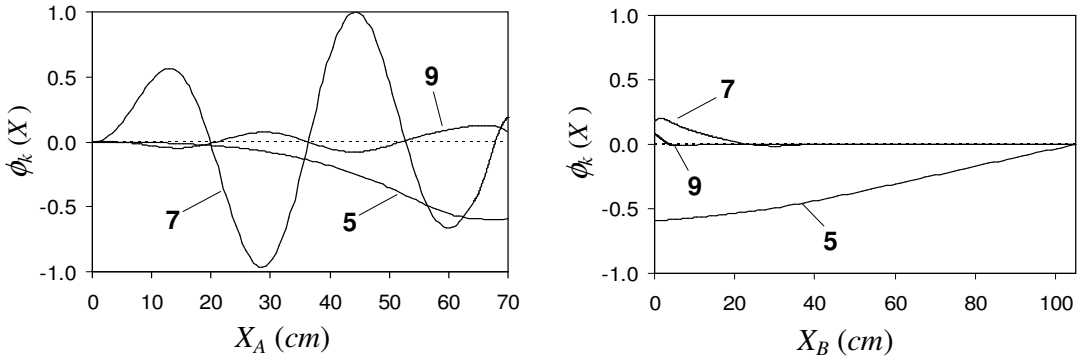

Figure 35: L-shaped frame: member *A* and *B* modal amplitude functions $\phi_k(X)$

of magnitude apart: (i) 164 (GBT – 12 elements in member A and 5 in member B) and (ii) 10500 (ANSYS). It is also observed that the two buckling mode shapes are remarkably similar, even if the GBT model has only 13 equations constraining the joint displacements (involving solely 9 end section nodes: 4 lip end and 5 intermediate nodes). The frame buckles in a local mode triggered by member *A* (shorter but more heavily compressed), involving also member *B* and with participations from deformation modes **5** (distortional) and **7**, **9** (local). There are major contributions from modes **7** and **5** in member *A*, whose maximum values occur at about 1/4-span from the joint and at the joint itself. Only mode **5** has a visible contribution in member *B*, which decreases from the joint to the support – the small participations from modes **7** and **9** have maximum values at the joint and virtually vanish as the 1/4-span mark is reached.

5.3 Post-Buckling Analysis

The first relevant work concerning development of a GBT geometrically non-linear formulation is due to Silvestre & Camotim (2003), who included the presence of arbitrary initial geometrical imperfections and adopted a total Lagrangian kinematic description. This formulation, based on a strain decomposition into Green-Lagrange membrane terms (some of them disregarded) and small-strain bending terms, was later extended to cover members with "non-standard" support conditions by Basaglia *et al.* (2011). A few years ago, Gonçalves & Camotim (2012)[32], in the context on non-linear elastic-plastic GBT analysis, found that several non-linear membrane strain terms previously disregarded play an important role in the non-linear behavior of thin-walled members, particularly in the moderate-to-large displacement range, and, therefore, must be included in the non-linear analysis. Very recently, Martins *et al.* (2018b), prompted by the need to tackle mode interaction problems, which often unavoidably involve moderate-to-large displacements, developed and implemented an enhanced GBT geometrically non-linear formulation able to provide accurate results in this displacement range. It includes (i) the whole set of non-linear membrane strain terms, adopting an approach equivalent (but not similar) to that employed by Gonçalves & Camotim (2012), and (ii) the non-linear bending strain terms – these last terms were subsequently found to have virtually no impact inside the sought domain of validity (*i.e.*, only matter in the large displacement range).

Back in 2012, Gonçalves & Camotim (2012) developed and implemented the first GBT formulations to conduct geometrically and materially non-linear analyses of prismatic thin-walled metal members, using two distinct approaches: either (i) the traditional stress-based approach, using small-strain J_2-flow theory (von Mises' yield criterion) with the associated flow rule and isotropic hardening, or (ii) a stress resultant-based approach that uses a modified Ilyushin yield function. More recently Abambres *et al.* (2013, 2014) also developed a geometrically and materially non-linear GBT formulation for thin-walled metal members

[32] These authors included, for the first time, quadratic transverse extension deformation modes in the GBT post-buckling analysis.

exhibiting isotropic hardening, based on J_2-flow plasticity theory combined with the backward Euler return-mapping algorithm (as the traditional approach of Gonçalves & Camotim 2012). They applied it to study the non-linear behavior of carbon steel, stainless steel and aluminum members with several loading and/or support conditions and exhibiting a few constitutive laws (perfectly plastic, bi-linear or non-linear).

5.3.1 Illustrative numerical results

The illustrative numerical results presented and discussed concern (i) the elastic distortional post-buckling buckling behavior of a fixed-ended zed-column (Martins *et al.* 2018b) and (ii) the elastic-plastic distortional post-buckling buckling behavior of an I-section beam (Abambres *et al.* 2013). For validation purposes, most GBT results are compared with values yielded by ABAQUS shell finite element analyses.

The first example concerns the "pure" distortional post-buckling behavior of a fixed-ended zed-column. The GBT nodal discretization adopted, which involves 15 nodes (4 natural intermediate, 2 natural end and 9 intermediate – 3 in the web and flanges), leads to (i) 17 conventional modes (4 global, 2 distortional and 11 local – modes **1**-**17**), (ii) 14 shear modes (5 global and *9* local – modes **18**-**31**), (iii) 14 linear transverse extension modes (1 global isotropic, 4 global deviatoric and 9 local – modes **32**-**45**), and (iv) 14 quadratic transverse extension modes (modes **46**-**59**). Figures 36(a)-(b) show the column geometry and critical distortional buckling mode shape (exhibiting three half-waves), as well as the most relevant modal amplitude functions $\bar{\phi}_k(x)$ participating in it. As for Figures 37(a)-(b), they display (i) several equilibrium paths P/P_{crD} vs. $(v+v_0)/t$, where v is the vertical displacement of the top flange-lip corner at the central half-wave and v_0=0.94t defines is initial geometrical imperfection amplitude (associated with outward v), and (ii) the modal participation diagram associated with the most rigorous GBT equilibrium path (up to P/P_{crD}=1.50 – for comparison/validation purposes, the equilibrium path provided by a rigorous ABAQUS SFEA is also presented. The equilibrium paths displayed are obtained from "approximate analyses" that either (i) adopt 8 beam finite elements and include various sub-sets of the 59 deformation modes (including all of them) or (ii) adopt 16 beam finite elements and all the 59 deformation modes – the modal participation diagram shown in Figure 37(b) concerns this last analysis. In order to illustrate the capabilities of the GBT intrinsic modal nature, Figures 38(a)-(f) and 39(a)-(f) provide the evolutions of (i) mid-web transverse bending displacement profiles $w(x)$, obtained with the contributions from modes **2**, **3**, **5+6**, **7-17**, **32-45** and **1-59** ($w_{1\text{-}59}(x)\equiv w(x)$), and (ii) top flange-lip corner vertical displacement profiles $v(x)$, obtained with contributions from modes **2**, **3**, **4**, **5+6**, **32-45** and **1-59** ($v_{1\text{-}59}(x)\equiv v(x)$). Finally, Figure 40 displays GBT and ABAQUS column deformed configurations corresponding to P/P_{crD}=1.00, 1.25. 1.50. The observation of all these post-buckling results prompts the following remarks:

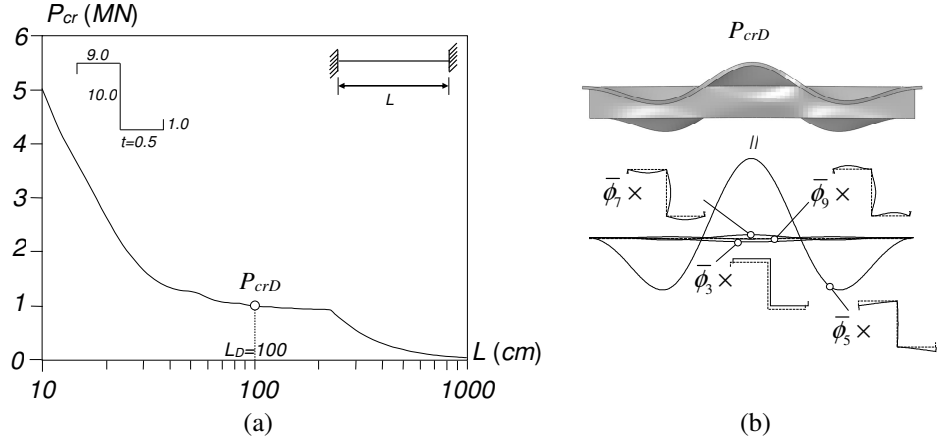

Figure 36: Fixed-ended zed-column (a) geometry and P_{cr} vs. L curve, and (b) critical mode and GBT modal amplitude functions

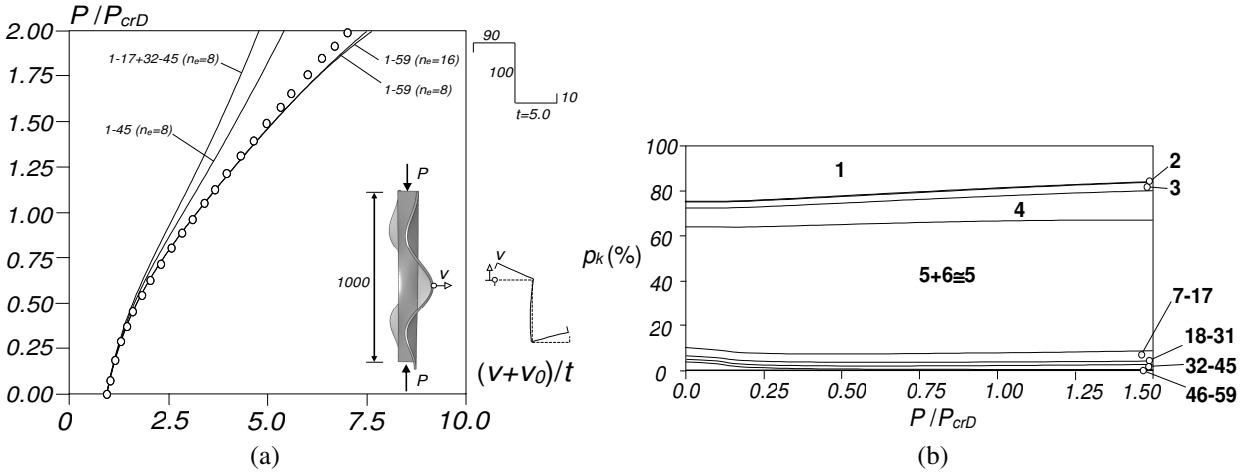

Figure 37: (a) ABAQUS and GBT P/P_{crD} vs. $(v+v_0)/t$ post-buckling equilibrium paths and (b) modal participation diagram (n_e=16)

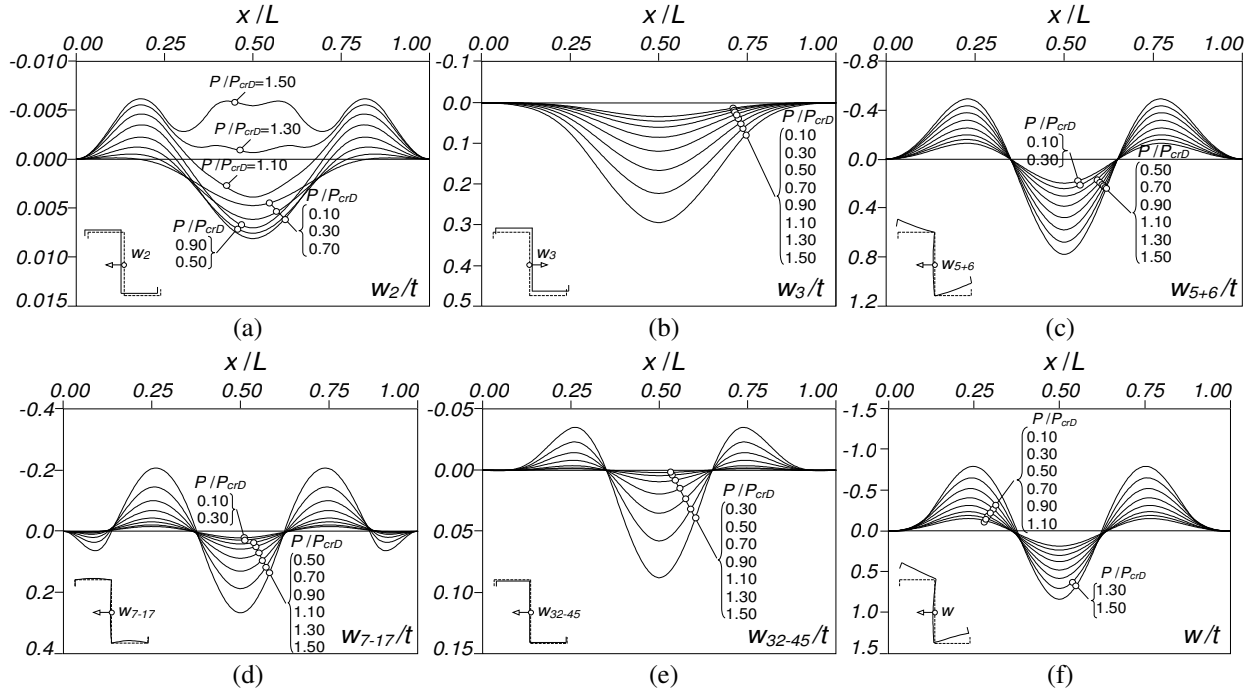

Figure 38: Zed-column $w(x)$ displacement profiles due to modes (a) **2**, (b) **3**, (c) **5+6**, (d) **7-17**, (e) **32-45**, (f) **1-59** ($w_{1\text{-}59}(x)\equiv w(x)$)

(i) Figure 37(a) makes it possible to assess the relevance of the quadratic transverse extension modes (**46**-**59**) in capturing the column distortional post-buckling behavior: their removal causes severe membrane locking effects and leads to overly stiff solutions (Gonçalves & Camotim 2012) – *e.g.*, compare the solutions "**1**-**45**+n_e=8" and "**1**-**59**+n_e=8". Moreover, note that the solutions obtained with 16 and 8 beam finite elements are virtually identical up to P/P_{crD}=1.50 – therefore, the "n_e=8" results can be viewed as the "best GBT ones" within this loading/displacement range.

(ii) The modal participation diagram of Figure 37(c) shows that, naturally, mode **5** (symmetric distortion) governs the column response – its participation remains practically constant along the equilibrium path, varying between 53% and 58% (the participation of mode **6** never exceeds 1%). As loading increases, mode **1** is gradually replaced by other modes – mode **4** (torsion) provides the largest contribution up until P/P_{crD}=1.50, while the remaining ones almost do not vary.

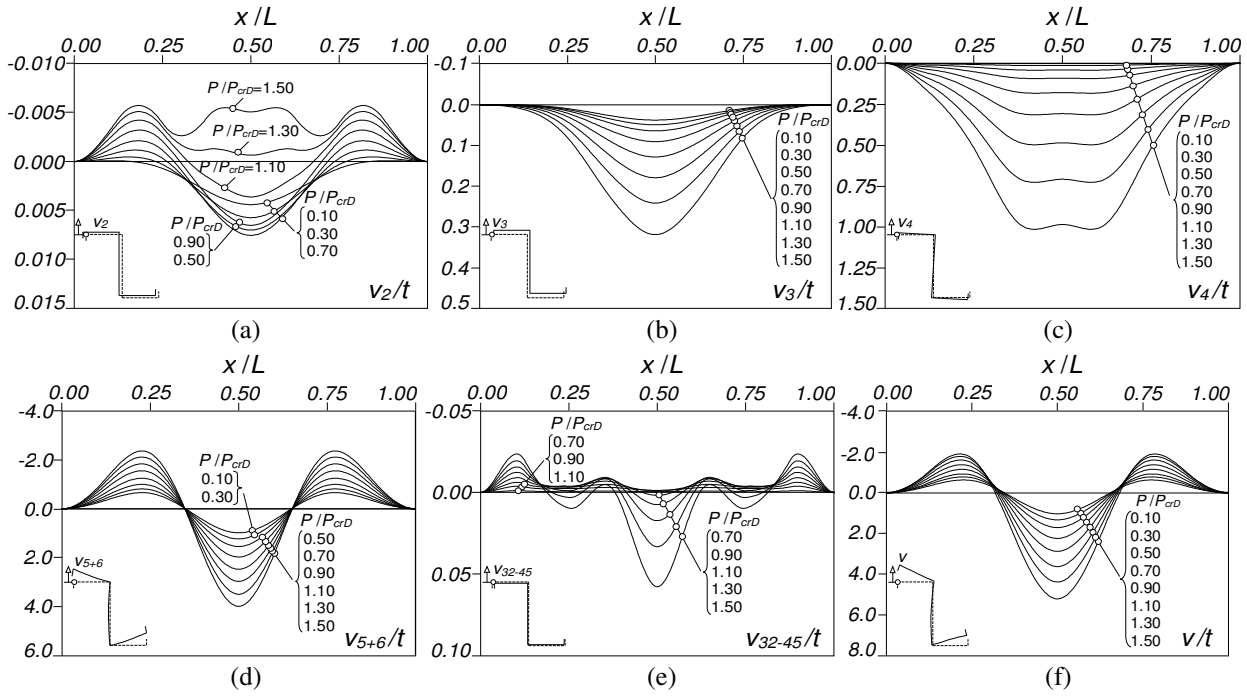

Figure 39: Zed-column $v(x)$ displacement profiles due to modes (a) **2**, (b) **3**, (c) **4**, (d) **5+6**, (e) **32-45**, (f) **1-59** ($v_{1\text{-}59}(x) \equiv v(x)$)

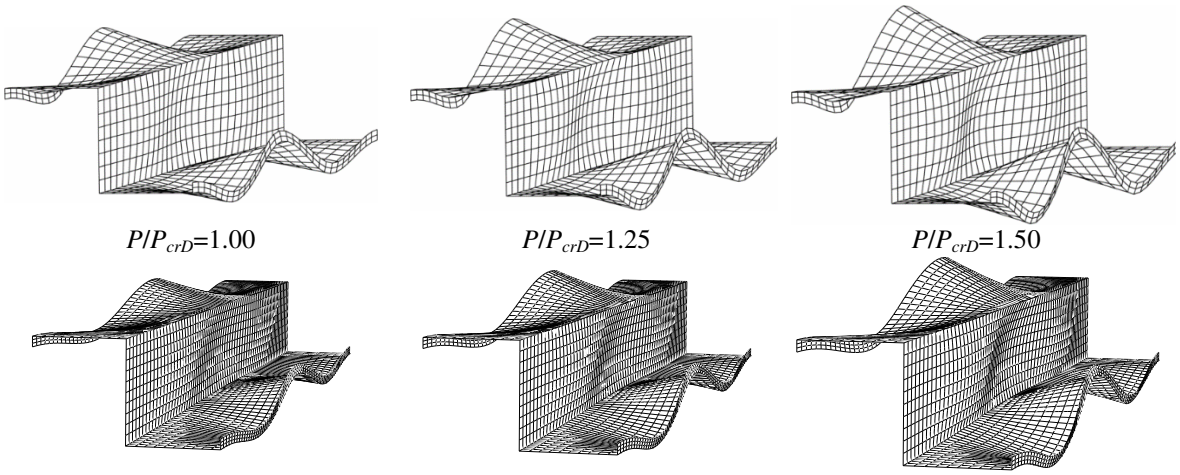

Figure 40: GBT vs. ABAQUS zed-column deformed configurations at P/P_{crD}=1.00, 1.25, 1.50 (amplified twice)

(iii) Figures 38(f) and 39(f) show that $w(x)$ and $v(x)$ are mostly due to mode **5** (see Figs. 38(d) and 39(d)), whose contribution involves three half-waves and is akin to the initial geometrical imperfection (see Fig. 36(b)). This modal contribution grows steadily as loading progresses, while retaining its configuration – this feature is shared by the contribution of mode **3** (minor-axis bending – one half-wave) and **7-17** (local – five half-waves). Besides the small contribution from mode **2** (see Figs. 38(a) and 39(a)), it is clear that mode **4** (see Fig. 39(c)), exhibiting clockwise rotations, plays a significant role – it is responsible for the difference between the top and bottom flange-lip motions, a behavioral feature not occurring in singly symmetric columns (*e.g.*, lipped channels).

(iv) Lastly, Figure 40 provides clear evidence of the virtual coincidence between the column deformed configurations obtained with GBT (1D beam model) and ABAQUS (shell finite element model), despite the huge disparity between the numbers of degrees of freedom involved in each of them.

The elastic-plastic post-buckling analysis deals with a fixed-pinned I-section beam acted by a vertical load, uniformly distributed on the mid-span top flange area (see Figs. 41(a)-(b)), exhibiting a bi-linear material behavior, characterized by E=210GPa, ν=0.3, f_y=235MPa and E_{sh}=E/100, with length L=2850mm and the cross-section mid-line dimensions given in Figure 41(b). The beam contains critical-mode (lateral-torsional) initial geometrical imperfection with a 3.02mm amplitude (maximum in-plane displacement).

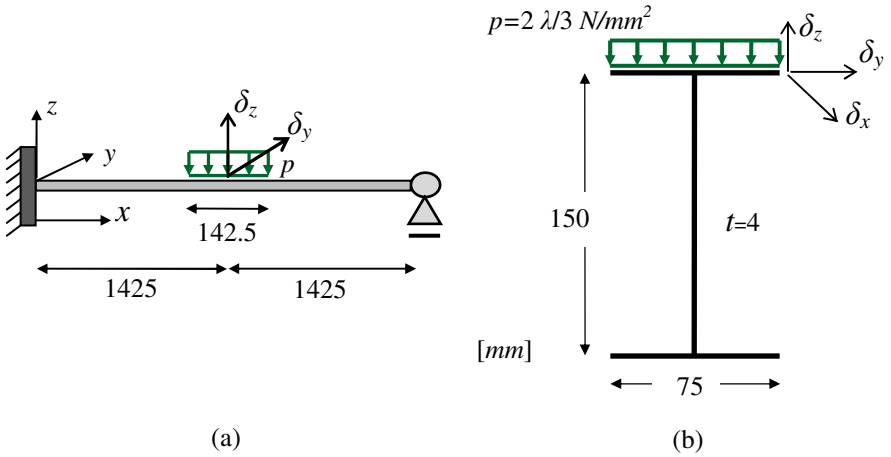

Figure 41: Fixed-pinned I-section beam (a) overall view and loading, and (b) cross-section dimensions.

The cross-section discretization adopted is shown together with the transverse extension mode shapes in Figure 42 – this figure provides also the in-plane and out-of-plane configurations of the deformation modes most relevant for this analysis. It is worth mentioning that, out of the 202 deformations modes associated with the nodal discretization shown in Figure 42, the analysis includes only 137, namely 4 global, 13 local, 81 shear and 39 transverse extension deformation modes.

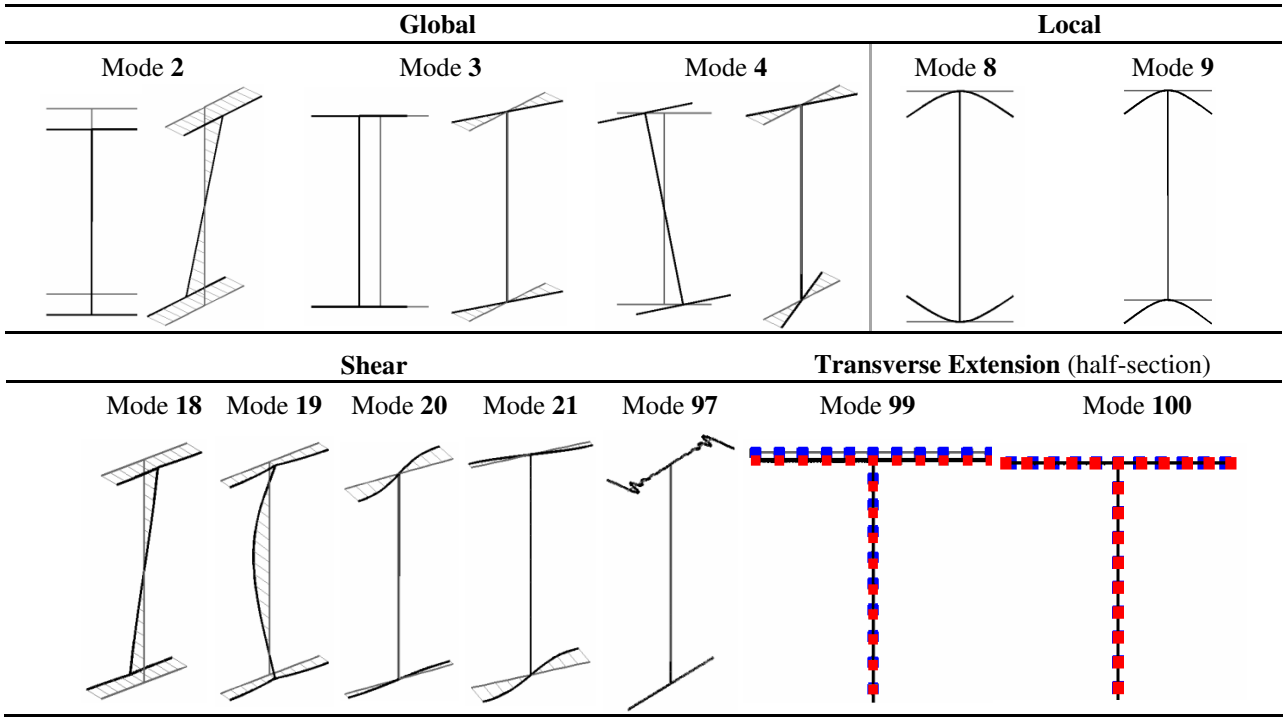

Figure 42: I-section beam in-plane and out-of-plane configurations of the 12 most relevant GBTdeformation modes

Figure 43(a) shows the GBT and ABAQUS equilibrium paths $\lambda(|\delta_y|)$, where $|\delta_y|$ is the absolute value of the mid-span top flange node lateral displacement, indicated in Fig. 41(b). Figure 43(b) shows the GBT modal participation diagram concerning the evolution, as $|\delta_y|$ increases, of the beam most deformed (mid-span) cross-section configuration. Lastly, Figure 44 shows the beam collapse mechanism (AP equilibrium state indicated in Fig. 43(a)). The observation of these results prompts the following comments:

(i) The GBT and ABAQUS equilibrium paths are in very good agreement – the maximum difference is 4.8% and occurs well into the descending branch (AP equilibrium state).

(ii) Global deformation clearly governs the beam behavior, through the contributions from modes **2** (15.4-60.7%), **3** (12.0-28.7%) and **4** (21.6-44.9%). The combined participation of the transverse extension modes **99** (web) and **100** (flanges) rises gradually along the equilibrium path, reaching 13% in the descending branch – excluding these two deformation modes from the analysis would considerably "stiffen" the beam global behavior, by severely restraining the significant wall in-plane motions clearly observed in Figure 44. Finally, local modes **8** and **9**, associated with the top/loaded flange transverse bending due to the patch loading (see Fig. 42 – note that the modes counteract each other in the bottom flange), only have perceptible contributions up to the peak load (their maximum joint participation is 4.3%).

(iii) The dominant global behavior and the early onset of yielding ($\lambda \approx 2.0$, at the beam mid-surface) explain the absence of post-critical strength ($\lambda_u / \lambda_{cr} = 0.774$).

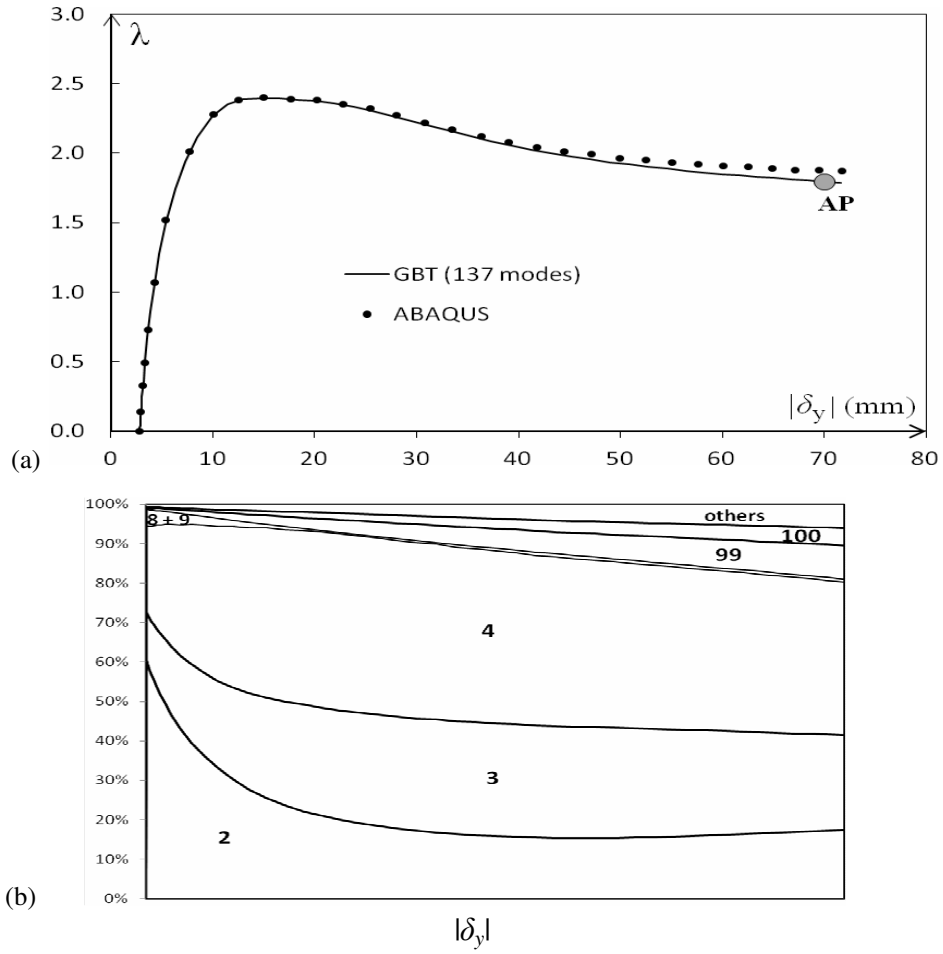

Figure 43: I-section beam (a) GBT and ABAQUS equilibrium paths λ vs. $|\delta_y|$ and (b) GBT modal participation diagram

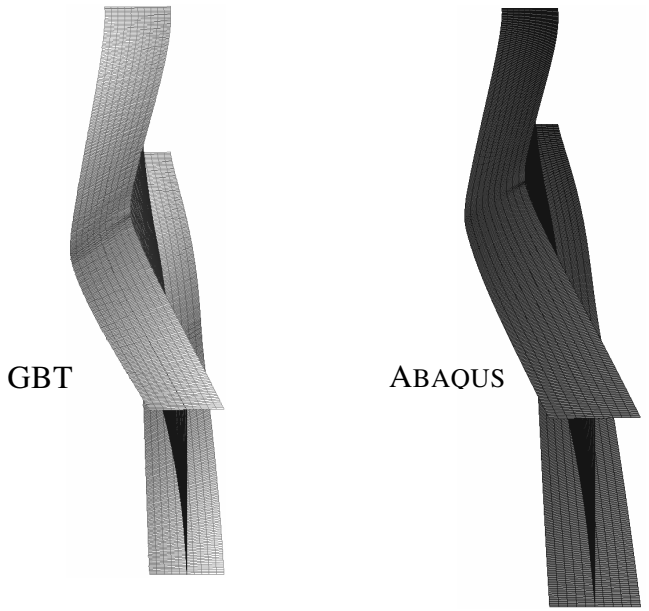

Figure 44: GBT and ABAQUS I-section beam collapse mechanism (AP equilibrium state)

(iv) Besides the remarkable resemblance between the GBT and ABAQUS beam collapse mechanism representations, note (iv_1) the yield-line at the most deformed cross-section top flange (close to the loaded area), and (iv_2) the visible (not visible) top (bottom) flange warping at the pinned end support – the modes **3** and **4** warping contributions reinforce (oppose) each other at this support (see Fig. 42).

6. Cold-Formed Steel Angle Columns

The geometrical simplicity of angles is only matched by the complexity of their structural behavior, as attested by the fact that the design of angle members has provided a continuous challenge to researchers and designers for many decades – last year's Beedle Award lecture (Lutz 2017) provides an excellent testimony of the hardships angle members have brought to the structural engineering profession! In the particular case of concentrically loaded cold-formed steel equal-leg angle short-to-intermediate columns (those buckling in flexural-torsional modes), their behavior, strength and design eluded the technical and scientific communities for a long time and prompted the use of specific design procedures (not used in columns with other cross-section shapes), very often involving safety factors higher than usual, which reflects the lack of knowledge about their structural behavior (*e.g.*, Ganesan & Moen 2012)[33]. For instance, up until 2012 angle columns were not pre-qualified to be designed by means of the Direct Strength Method (DSM) in the North American Specification (AISI 2012) – although the concept of pre-qualification was removed from the latest version of this specification (AISI 2016), no novel provisions or guidelines for the DSM design of angle columns were added (*i.e.*, no new knowledge has been included).

Up until quite recently, the most successful attempts to develop DSM-based design for equal-leg angle columns, namely those due to Young (2004), for fixed-ended columns, Rasmussen (2006), for pin-ended columns, and Silvestre *et al*. (2013), for fixed and pin-ended columns, were based on local strength concepts, in view of the belief that such columns fail in local-global interactive modes – therefore, they involved using either the current DSM local and global design curves or slightly modified (empirically) versions of these curves. In spite of the quite positive performance indicators of the above DSM design

[33] Note that the structural behavior of (long) equal-leg angle columns buckling and failing in minor-axis flexural modes is perfectly understood. Therefore, the design of such columns is straightforward and performed through the usual procedure for compression members.

approaches, it is now clear that they were founded on an erroneous mechanical model. Indeed, the findings of Dinis *et al.* (2012a) and Mesacasa *et al.* (2014) provided clear numerical evidence that the column failure stems from the interaction between major-axis flexural-torsional[34] and minor-axis flexural buckling, a kind of unique global coupling phenomenon that (i) does not involve local deformations and (ii) is highly sensitive to the "sign" of the minor-axis flexural initial geometrical imperfections. Based on these findings, Dinis & Camotim (2015a) proposed a rational DSM-based design approach that was found to provide safe and reliable predictions of all available experimental and numerical failure loads concerning both fixed-ended and pin-ended columns. At this stage, it should be mentioned that these two support conditions only differ in the restraint of the end-section minor-axis flexural rotations, which are either fully restrained (fixed end) or completely free (pinned end) – in both cases, the columns are fixed-ended with respect to major-axis flexure and have the (secondary) warping of their end cross-sections fully restrained. In the experimental studies, warping fixity is achieved by attaching thick/rigid plates to the column end cross-sections and the pin-ended support conditions correspond to "cylindrical hinges".

After briefly addressing the key features of the fixed-ended and pin-ended short-to-intermediate angle column buckling and post-buckling behaviors, the paper provides an overview of the above DSM-based novel design approach and presents the quality assessment of its failure load estimates.

6.1 Buckling and Post-Buckling Behavior

Figures 45(a)-(b) provide the signature curve P_{cr} vs. L (P_{cr} and L are the critical buckling load and length, the latter in logarithmic scale) and corresponding GBT modal participation diagram of fixed-ended (F) and pin-ended (P) columns with the cross-section dimensions indicated – note that the two P_{cr} vs. L. only differ for moderate and long columns. As for Figure 45(c), it shows the buckling modes of P columns with L=100;364;1000 *cm* and the in-plane shapes of the first 5 GBT deformation modes. It is clear that the "plateau" in these signature curves correspond always to flexural-torsional buckling – the amount of major-axis flexure (mode **2**) is initially minute and increases visibly with L. Moreover, the flexural-torsional buckling loads and mode shapes of F and P columns with the same length are identical.

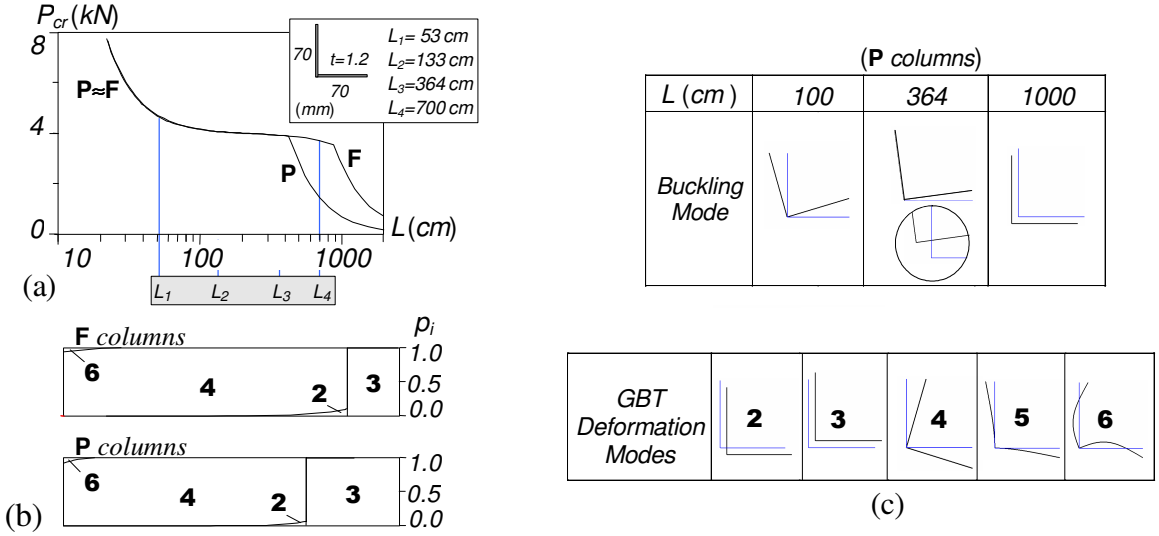

Figure 45: (a) P_{cr} vs. L curves and (b) GBT modal participation diagrams (F and P columns), and (c) in-plane shapes of 3 buckling modes and first 5 GBT deformations modes (P columns)

[34] In equal-leg angle columns, (i) local and torsional deformations are indistinguishable and (ii) the flexural-torsional buckling modes are predominantly torsional, which explains why they were erroneously viewed as "local".

ABAQUS shell finite element (SFEA) analyses were used to investigate the elastic and elastic-plastic post-buckling behavior of F and P columns (i) with lengths L_1=53*cm*, L_2=133*cm*, L_3=364*cm* and L_4=700*cm* (F_1-F_4 and P_1-P_3 columns), (ii) containing critical-mode (flexural-torsional) initial imperfections with small amplitude and, in the elastic-plastic case, (iii) with various yield-to-critical stress ratios. Figures 46(a)-(f) show the upper parts of the F_1-F_4 and P_1-P_3 column elastic equilibrium paths P/P_{cr} *vs.* β, P/P_{cr} *vs.* d_M/t and P/P_{cr} *vs.* $d_m/t - \beta$, d_M and d_m are the mid-span rigid-body torsional rotation and flexural displacements due to major and minor-axis flexure, respectively. These post-buckling paths prompt the following comments:

(i) All post-buckling behaviors involve the occurrence of torsional rotations and flexural displacements. The relative importance of the latter has strong impact on the column post-critical strength reserve.

(ii) Two F-column and P-column post-buckling behaviors are identified: while (ii_1) the shorter F_1-F_3 and P_1 columns are clearly stable and exhibit minute displacements, and (ii_2) the longer F_4 and P_2-P_3 columns are barely stable, exhibit significant displacements and have limit points – either abrupt and followed by a torsional rotation reversal (F_4 and P_2 columns) or smooth with no rotation reversal (P_3 column). The displacement magnitude plays a key role in separating the two post-buckling behaviors.

(iii) In both the F and P-column equilibrium paths the d_M values remain always very small (they grow with L and retain the fixed-ended critical buckling mode shape). However, the P column d_m values are significantly higher (about ten times) than their d_M counterparts – their magnitude are similar (both small) in F columns (before the interaction with minor-axis flexure buckling occurs, of course)

(iv) The difference described in the previous item stems from the absence of minor-axis end bending moments in the P columns, making it impossible to oppose the minor-axis bending due the "effective centroid shift" effects caused by the normal stress redistribution (*e.g.*, Young & Rasmussen 1999).

Next, the influence of plasticity effects on the column post-buckling behavior and collapse is addressed. Figures 47(a_1)-(a_3) show the upper portions of the F_3, F_4 and P_2 column elastic-plastic equilibrium paths

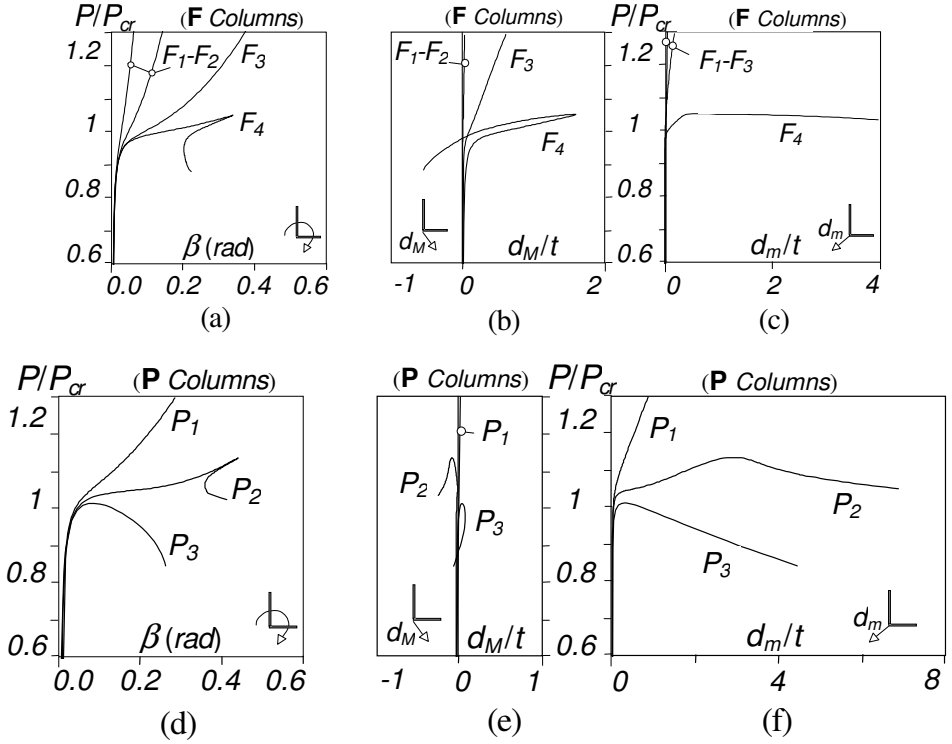

Figure 46: F_1-F_4 and P_1-P_3 column (a+d) P/P_{cr} *vs.* β, (b+e) P/P_{cr} *vs.* d_M/t and (c+f) P/P_{cr} *vs.* d_m/t equilibrium paths

P/P_{cr} *vs.* β paths for yield-to-critical stress ratios f_y/f_{cr}≈1.3,2.5,5.0 (plus the elastic path). As for Figures 47(b_1)-(b_3), they display plastic strain diagrams at the three equilibrium states indicated in Figures 47(a_1)-(a_3), located on the f_y/f_{cr}≈2.5 equilibrium paths (including the collapse modes). It is worth noting that:

(i) The F_3 column failure load grows noticeably with f_y – *e.g.*, a f_y/f_{cr} increase from 1.3 to 5.0 more than doubles the load-carrying capacity.

(ii) The longer F_4 and P_2 column failure loads are practically insensitive to f_y, as their collapses are mostly due to geometrically non-linear effects – *e.g.*, a f_y/f_{cr} rise from 1.3 to 5.0 entails only a 9.4% failure load increase in the P_2 column. Indeed, for f_y/f_{cr}≈2.5,5.0 the F_4 and P_2 columns remain elastic up to failure – the onset of yielding only takes place well inside the equilibrium path descending branch.

The markedly different elastic and elastic-plastic length-dependent post-buckling behaviors exhibited by the F and P short-to-intermediate angle columns implies significant differences between their failure loads P_u (for any given yield stress). Since all these columns have virtually identical critical buckling stresses, *i.e.*, share a common critical slenderness $\lambda=(f_y/f_{cr})^{0.5}$, the corresponding P_u/P_y values are likely to be highly scattered for each λ value – this behavioral feature is adequately accounted for by the DSM design approach originally proposed by Dinis & Camotim (2015a), then slightly improved by Landesmann *et al.* (2016) and, finally, cast in a simpler form by Dinis & Camotim (2016a) – it is addressed next.

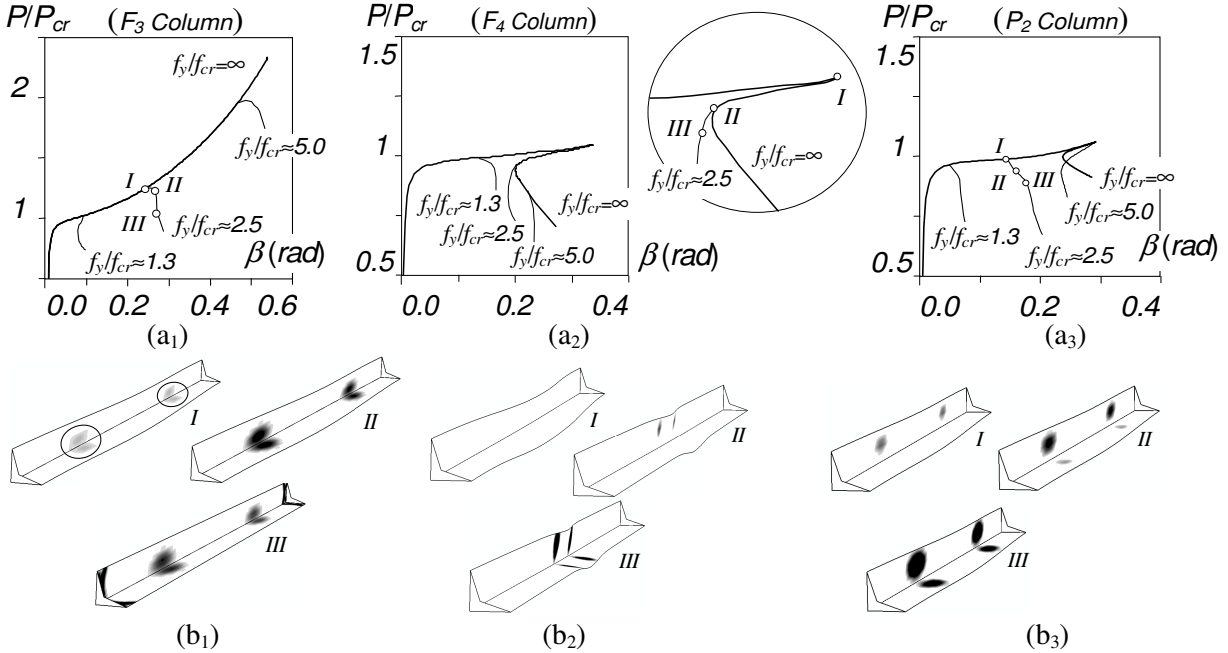

Figure 47: (a) P/P_{cr} *vs.* β elastic-plastic equilibrium paths, for f_y/f_{cr}≈*1.3, 2.5, 5.0*, and (b) plastic strain diagrams and collapse modes, for f_y/f_{cr}≈*2.5*, of the ($_1$) F_3, ($_2$) F_4 and ($_3$) P_2 columns

6.2 DSM Design Approach

The main aspects and characteristics of the DSM-based design approach are the following:

(i) It is based on the fact that most short-to-intermediate angle columns fail in interactive modes combining major-axis flexural-torsional and minor-axis flexural deformations.

(ii) It involves (ii_1) the current DSM global strength curve and (ii_2) genuine flexural-torsional strength curves (P_{nft}), developed on the basis of failure loads of columns with fully prevented minor-axis bending displacements (see Fig. 48(a)), which replace the current DSM local strength curve in the

currently codified design against local-global interactive failures, are applicable to F and P columns, and capture the flexural-torsional post-buckling strength drop as the column length increases.

(iii) The effective centroid shift effects, which strongly influence the P column failure loads (not the F column ones), are incorporated through a "reduction parameter" β that only comes into play for P columns (idea put forward by Rasmussen 2006) and must reflect, as closely as possible, the length-dependence of the difference between the P and F column flexural-torsional behaviors.

Therefore, the DSM design approach requires (i) developing a set of genuine flexural-torsional strength curves, covering adequately the whole $P_{cr}(L)$ curve plateau, and (ii) quantifying the effective centroid shift effects (in P columns), which was done through a "reduction factor" based on the relation between the elastic post-buckling strengths of otherwise identical P and F columns. The main concepts and procedures involved in the performance of these tasks are addressed next.

6.2.1 Flexural-torsional strength curves

Figure 48(a) plots, against λ_{ft}, the P_u/P_y values corresponding to the fairly large flexural-torsional failure load data obtained by Dinis & Camotim (2015a) – also displayed is the current DSM local strength curve. The clear and huge "vertical dispersion" of the P_u/P_y values makes it easy to understand that no single Winter-type curve is able to predict safely and accurately all of them. It is also clear that a large number of those values fall well below the current DSM local strength curve. The above "vertical dispersion" is closely linked to the column length. Indeed, the P_u/P_y values gradually drop as L increases along the $P_{cr}(L)$ curve "plateau", which is completely in line with the findings obtained for the unrestrained columns (see Figs 46(a)-(f)). Figure 48(b) illustrates the length-dependence of the restrained column post-buckling strength: the four elastic equilibrium paths displayed, concerning columns with increasing lengths L_1-L_4, evidence a very clear post-critical strength drop.

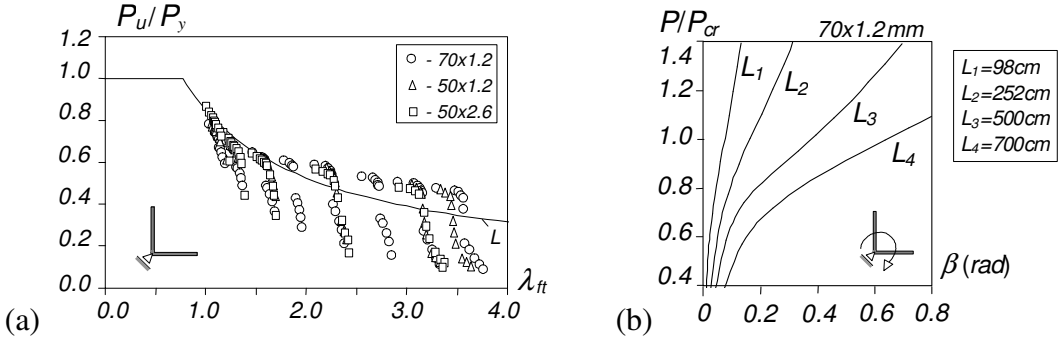

Figure 48: (a) Plot P_u/P_y vs. λ_{ft} (P_u are column flexural-torsional failure loads) and (b) elastic equilibrium paths P/P_{cr} vs. β of restrained $70\times1.2mm$ columns with lengths L=98,252,500,700cm

An in-depth study of the column pure flexural-torsional behavior unveiled that the participation of major-axis flexure (mode **2**) in the column critical buckling mode (i) increases gradually with L (see Fig. 45(b)) and (ii) is directly linked to the difference between the pure torsional (f_{bt}) and flexural-torsional (f_{crft} – critical) buckling stresses, provided exactly by analytical expressions given by Dinis & Camotim (2015a). In view of these findings, it was decided to group the columns according to the percentage difference between f_{bt} and f_{crft} (*i.e.*, to $\Delta_f=[(f_{bt}-f_{crft})/f_{bt}]\times100$ – this parameter "measures" the relative importance of major-axis flexure on the flexural-torsional buckling behavior and, therefore, is ideally suited to quantify the length dependence of the column post-critical strength along the $P_{cr}(L)$ curve plateau[35].

[35] This expression, proposed by Landesmann *et al.* (2016), differs slightly from the original Δ_f definition put forward by Dinis & Camotim (2015).

The proposed flexural-torsional strength curves (P_{nft}) are defined by "Winter-type" expressions, which incorporate parameter Δ_f to account for the length-dependence and read (Dinis & Camotim 2016)

$$P_{nft} = \begin{cases} P_y & if \quad \lambda_{ft} \le \left(0.5 + \sqrt{0.25 - b}\right)^{\frac{1}{2a}} \\ P_y \left(\frac{P_{crft}}{P_y}\right)^a \left[1 - b\left(\frac{P_{crft}}{P_y}\right)^a\right] & if \quad \lambda_{ft} > \left(0.5 + \sqrt{0.25 - b}\right)^{\frac{1}{2a}} \end{cases} \tag{7}$$

$$a = \begin{cases} 0.19\,\Delta_f + 0.4 & if \quad \Delta_f < 3 \\ 0.97 & if \quad \Delta_f \ge 3 \end{cases} \qquad b = \begin{cases} 0.014\,\Delta_f + 0.15 & if \quad \Delta_f \le 7 \\ 0.248 & if \quad \Delta_f > 7 \end{cases}, \tag{8}$$

where each combination of parameters a and b[36] leads to a different curve – the length-dependence is captured through these two parameters, both expressed in terms of Δ_f. Note that a=0.4 and b=0.15 are adopted for Δ_f=0, which amounts to saying that Eq. (7) coincides with the current DSM local strength curve for the very short columns (f_{bt}/f_{crft} very close to 1.00).

It was found that the proposed P_{nft} strength curve set is able to capture quite well the "vertical dispersion" of the numerical failure load data displayed in Fig. 48(a) – Figures 49(a)-(b), showing two individual flexural-torsional strength curves obtained from Eq. (7), associated with Δ_f=1.80; 7.20, illustrate this assertion: the numerical failure loads of the columns exhibiting those Δ_f values are reasonably well predicted by them – naturally, the prediction quality varies with Δ_f (in this case, it is better for Δ_f=7.20).

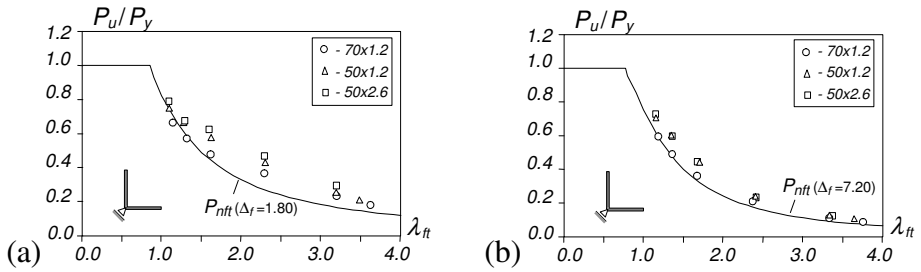

Figure 49: Plots of P_u/P_y vs. λ_{ft} and proposed flexural-torsional (P_{nft}) strength curves for columns with minor-axis bending displacements fully prevented such that (a) Δ_f=1.80 and (b) Δ_f=7.20

Recalling that the mechanical reasoning behind the DSM design approach is based on the fact that the columns fail in global-global interactive modes, combing major-axis flexural-torsional and minor-axis flexural deformations, it is now possible to obtain strength curves providing the nominal strength against the above failures (P_{nfte}) of fixed-ended (F) short-to-intermediate angle columns. It suffices to replace P_y by P_{ne} (nominal failure load provided by the current DSM global design curve) in Eq. (7) – the ensuing strength curve set is expressed in terms of the "interactive" slenderness $\lambda_{fte}=(P_{ne}/P_{crft})^{0.5}$.

6.2.2 Reduction parameter β

The next step consists of finding a length-dependent "reduction parameter" β that, when multiplied by the F column nominal strength P_{nfte}, provides its P column counterpart. The procedure adopted to search for this parameter is based on an "elastic reduction factor" concept and involves the following steps:

[36] Do not confuse with the angle leg width, also designated as b.

(i) Perform elastic post-buckling analyses of identical F and P columns (same f_{bl}/f_{crft} ratio, *i.e.*, Δ_f value), both containing critical-mode initial geometrical imperfections with amplitude $L/1000$, and record the evolution, as the applied load increases, of the maximum longitudinal normal stresses at mid-span (f_{max}) – the P vs. f_{max} curves of F and P columns associated with Δ_f=0.16 are displayed in Figure 50(a).

(ii) Calculate, for any given f_{max} value, the ratio between the F and P column applied loads causing it (P_F and P_P) – note that difference between P_F and P_P stems solely from the effective centroid shift effects, which make the interaction with minor-axis flexural buckling much more pronounced in the P column. If f_{max} is equal to the column yield stress ($f_{max}=f_y$), the corresponding P_P/P_F ratio provides the strength reduction parameter at the column "elastic limit state".

(iii) Assume that the above P_P/P_F ratio is a good enough approximation of the sought strength reduction parameter at the column elastic-plastic failure (β) – in other words, assume that $\beta \approx P_P/P_F$.

(iv) Take f_{max} as the column global nominal strength f_{ne}, which implies that its "interactive" slenderness is given by $\lambda_{fte}=(f_{max}/f_{crft})^{0.5}$, making it possible to establish a relationship between β and λ_{fte}. Then, it is possible to obtain a set of length-dependent $\beta(\lambda_{fte})$ curves, one per Δ_f value – Figure 50(b) shows the $\beta(\lambda_{fte})$ curves of columns associated with Δ_f=0.16, 0.84; 2.41. The differences between these curves clearly evidence the length-dependence of $\beta(\lambda_{fte})$ – β decreases substantially as L (*i.e.*, Δ_f) increases.

(v) Using a "trial-and-error curve-fitting procedure", search for "Winter-type" expressions relating β to λ_{fte} – it was found (Dinis & Camotim 2016) that the simpler output of this search is

$$\beta = \frac{0.68}{(\lambda_{fte} - c)^d} \leq 1 \tag{9}$$

$$c = -0.2\ \Delta_f + 0.55 \qquad d = 0.08\ \Delta_f + 0.72 \quad . \tag{10}$$

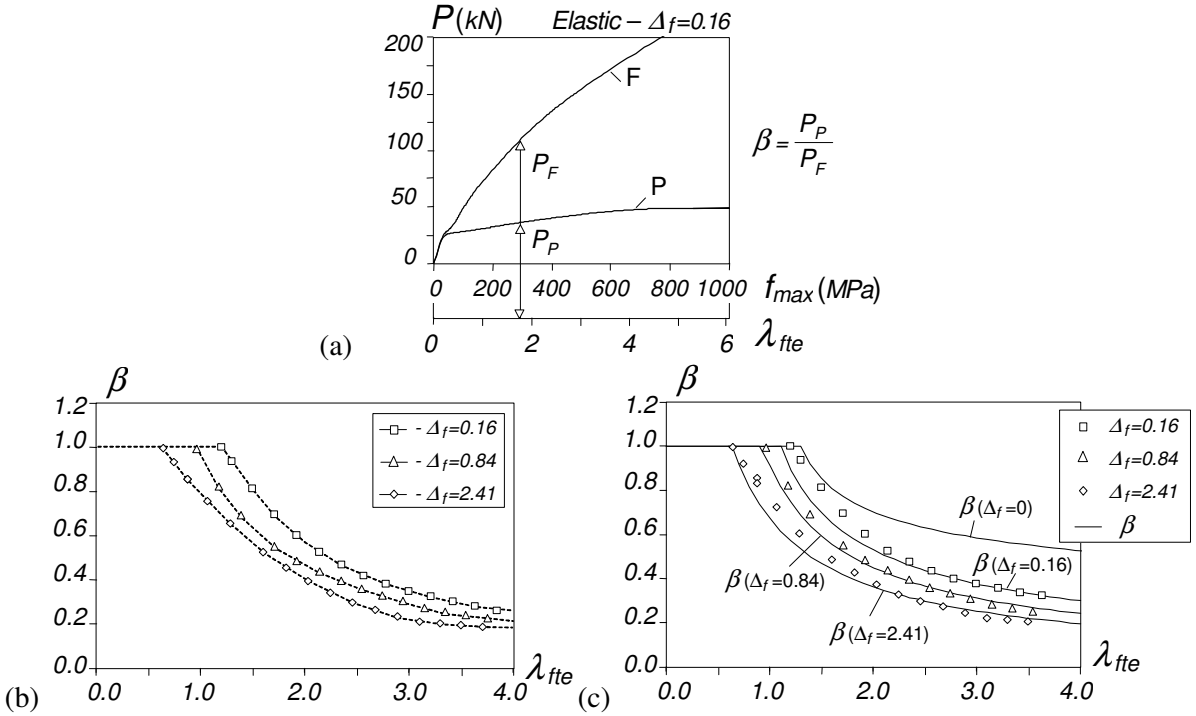

Figure 50: (a) P vs. f_{max} curves concerning F and P columns with Δ_f=0.16, (b) numerically obtained β values, plotted against λ_{fte}, and (c) proposed $\beta(\lambda_{fte})$ curves relating P and F columns with Δ_f=0.16, 0.84 and 2.41

6.3 DSM Design Proposal

Combining now (i) the strength curves for F columns, previously obtained in Section 6.2.1 and consisting of Eqs. (7)-(8) with P_y replaced by P_{ne}, and (ii) the reduction parameter β, just obtained in Section 6.2.2, it is possible to propose DSM-based strength curves providing nominal failure loads (P_{nfte}) of short-to-intermediate fixed-ended and pin-ended angle columns, which fail in interactive "global-global" modes combining torsional rotations with major- and minor-axis translations – they are defined by the expressions

$$P_{nfte} = \begin{cases} \beta \cdot P_{ne} & if \quad \lambda_{fte} \le \left(0.5 + \sqrt{0.25 - b}\right)^{\frac{1}{2a}} \\ \beta \cdot P_{ne} \left(\frac{P_{crft}}{P_{ne}}\right)^{a} \left[1 - b\left(\frac{P_{crft}}{P_{ne}}\right)^{a}\right] & if \quad \lambda_{fte} > \left(0.5 + \sqrt{0.25 - b}\right)^{\frac{1}{2a}} \end{cases} \tag{11}$$

$$\beta = \begin{cases} 1 & for\ F\ columns \\ \dfrac{0.68}{(\lambda_{fte} - c)^{d}} \le 1 & for\ P\ columns \end{cases} , \tag{12}$$

where (i) a, b and c, d are given by Eqs. (8) and (10), and (ii) $\lambda_{fte}=(f_{ne}/f_{crft})^{0.5}$ is the "interactive" slenderness.

6.3.1 Merit assessment

The above DSM-based strength curves provide quite accurate and reliable failure load predictions. Figures 51(a)-(b) plot, against λ_{fte}, the exact-to-predicted failure load ratios (P_u/P_{nfte}) concerning the whole set of F and P column experimental and numerical failure loads assembled (either obtained or collected from the literature) by Dinis & Camotim (2016a) – the P_u/P_{nfte} performance indicators (average, standard deviation, maximum and minimum values) are also given in those figures, as well as the corresponding LRFD resistance factors ϕ_c, evaluated by means of the expression prescribed by AISI (2016). When both the experimental and numerical failure loads are considered, the LRFD resistance factors read ϕ_c=0.88

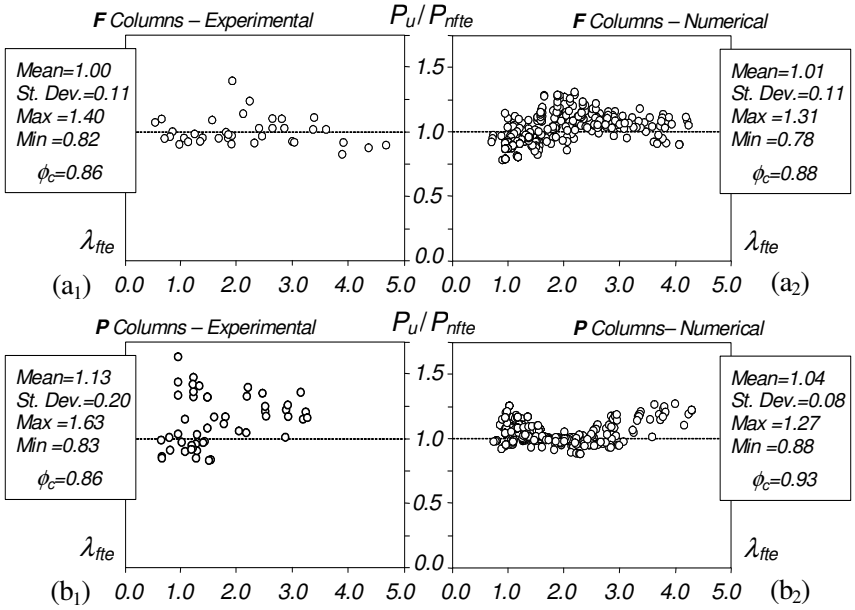

Figure 51: Plots P_u/P_{nfte} vs. λ_{fte} concerning the (a) F and (b) P column ($_1$) experimental and ($_2$) numerical failure loads

(F columns) and ϕ_c=0.91 (P columns). In view of these results, a DSM design proposal for fixed-ended and pin-ended equal-leg angle columns establishing that the nominal strength is $P_n=min\{P_{ne}; P_{nfte}\}$, where P_{ne} and P_{nfte} are provided by the current DSM global design curve and Eqs. (11)-(12), respectively, is ready for codification in the North American Specification (NAS) for the Design of Cold-Formed Steel Structural Members (AISI 2016) – moreover, it can be used together ϕ_c=0.85, thus completely unifying the treatment of compression members in this specification.

7. Cold-Formed Steel Members Undergoing Mode Interaction

The complex shape and high wall slenderness exhibited by the open thin-walled cross-sections commonly used in cold-formed steel (CFS) members make them highly susceptible to several instability phenomena, involving either individual and/or coupled buckling modes. The efficient design of such members is far from well established, as interactive buckling phenomena may emerge even when the associated critical buckling loads/moments are significantly apart. Thus, in order to assess the structural response of such members it does not suffice to acquire in-depth knowledge about their "pure"/individual buckling and post-buckling behaviors, since couplings involving two (or even three) buckling modes may occur. Naturally, such coupling effects may erode, to a smaller or larger extent, the member ultimate strength, thus leading to a high likelihood of reaching unsafe designs. Concerning mode interaction phenomena that may affect CFS members, those involving local and global buckling are, by far, the better understood – their effects are currently taken into account in the design of slender members, through either the classical "plate effective width" concept or the more recent Direct Strength Method (*e.g.*, AISI 2016)[37]. However, in the context of the DSM, the picture changes for columns and beam undergoing interaction phenomena involving distortional buckling, namely local-distortional (L-D), local-distortional-global (L-D-G) or distortional-global (D-G) interaction, which are potential additional sources of failure load or moment erosion not yet adequately covered by any cold-formed steel specification around the world. This fact is particularly worrisome with the advent and progressively widespread use of high-strength steels, which makes mode interaction phenomena much more relevant, in the sense that are much more likely to govern the failure of non-stocky CFS members.

An extensive research effort has been carried out in the last few years at the University of Lisbon on mode interaction in CFS columns and beams prone to distortional buckling. This investigation, comprising experimental tests (performed at the Federal University of Rio de Janeiro and University of Hong Kong – FURJ and UHK), numerical (shell finite element analysis – SFEA) simulations and design proposals, is intended to (i) acquire in-depth knowledge on the post-buckling behavior (elastic and elastic-plastic), ultimate strength and failure mode nature of CFS columns and beams experiencing L-D, L-D-G or D-G interaction, (ii) obtain and/or collect experimental and numerical ultimate strength data, and (iii) use this information to develop, calibrate, validate and proposes efficient (safe and accurate) DSM-based design approaches to predict the ultimate strengths of the members under consideration.

In view of the really enormous amount of work available (and also under way) on this topic, it is virtually impossible to address in this paper more than a very small fraction of the results and findings obtained. Therefore, a lot of thought has gone into how to organize this section, so that it (i) projects a clear image of the whole ongoing research endeavor, (ii) provides an account as detailed as possible of the methodology employed to achieve the established goals and (iii) presents and discusses a representative (but small)

[37] It should be pointed out that, currently, the DSM covers only the design of CFS columns and beams failing in local, distortional, global and local-global interactive modes. Concerning CFS beam-columns, a DSM-based design approach for "pure" failures is being sought by Torabian & Schafer (2018) – in view of the promising results already reported its codification should be expected for the not too distant future. Naturally, the DSM design of CFS beam-columns failing in interactive modes will only be addressed a bit further down the road.

sample of the knowledge acquired in the course of such an extensive investigation. The outcome of this "brain storming procedure": after presenting a few fundamental concepts that are common to all the coupling phenomena investigated, (i) identify and characterize the main steps and procedures involved in the methodology adopted to study the various mode interaction behaviors addressed and, for each of those steps and procedures, (ii) provide an illustration concerning one member coupling phenomenon. This means that no complete account of the work carried out concerning a particular member interactive behavior will be presented – instead, the paper includes a "mix" of the results and findings obtained for the several member coupling phenomena addressed. Recall that these phenomena consist of (i) L-D, L-D-G and D-G interaction in simply supported and (mostly) fixed-ended columns, and (ii) L-D and D-G interaction in simply supported beams with the two end support conditions shown in Figure 19.

7.1 Fundamental Concepts

In order to illustrate mode coupling phenomena involving distortional buckling, Figures 52(a_1)-(a_3) display "signature curves" (P_{cr} vs. L in logarithmic scale) that concern simply supported lipped channel columns with particular cross-section dimensions and make it possible to identify lengths associated L-D, D-G and L-D-G mode interaction (Camotim & Dinis 2011) – note the virtually coincident local, distortional and/or global critical buckling loads, which ensure maximum interaction effects and characterize the so-called "true interactive behaviors". As for Figures 52(b_1)-(b_3), they show possible critical buckling modes of the columns indicated in Figures 52(a_1)-(a_3), which combine the deformation patterns corresponding to the competing critical buckling modes: (i) 3 L half-waves + 1 D half-wave, (ii) 3 D half-waves + 1 G half-wave and (iii) 19 L half-waves + 3 D half-waves +1 G half-wave.

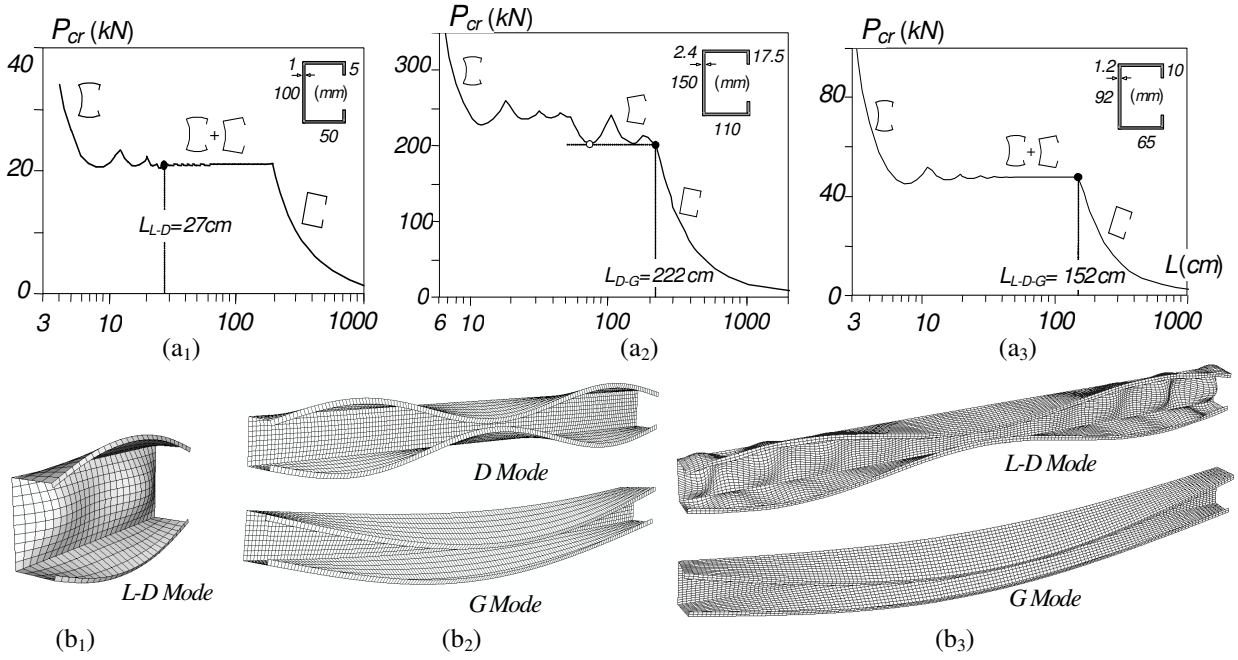

Figure 52: (a) P_{cr} vs. L signature curve and (b) local and/or distortional and global (flexural-torsional) buckling modes for lipped channel columns cross-section geometries and lengths that maximize the ($_1$) L-D, ($_2$) D-G and ($_3$) L-D-G mode interaction effects

However, it should be made clear that mode interaction involving distortional buckling may also occur in members exhibiting cross-sections and lengths such that either the competing local and/or distortional critical buckling stresses are visibly lower than the remaining one(s), provided that the yield stress exceeds the highest critical buckling stress by a large enough amount (*i.e.*, $f_y > f_{cr,max}$), which characterizes

the so-called "secondary bifurcation interactive behavior". It is worth noting that, as shown by Dinis *et al.* (2012b) in the context of L-D-G coupling, no secondary bifurcation interaction takes place when global buckling is critical, due to the associated minute post-critical strength, which precludes reaching applied stress levels close to the critical local and/or distortional buckling stresses. Naturally, the most pronounced secondary bifurcation interaction effects arise when local buckling is critical, due to the ensuing large post-critical strength – when $f_{cr.min}=f_{crD}$ the post-critical strength is just moderate (but still visible).

In order to illustrate the difference between the two above mode interaction types, Figures 53(a)-(b) display the elastic equilibrium paths (f vs. d) and six cross-section buckled configurations concerning lipped channel columns exhibiting true and secondary distortional/global-bifurcation L-D-G interaction, respectively – the latter corresponds to $f_{cr.min}=f_{crL}$ and $f_{cr.max}=f_{crD}\approx f_{crG}$. In the first case, coupling starts at the early loading stages and evolves as loading progresses – local, distortional and global (flexural-torsional) deformations develop along the whole equilibrium path, provided that the column has initial geometrical imperfections with L, D and G components. In the second case, the deformation is essentially local up to the vicinity of the critical distortional/global buckling applied stress level, when visible distortional and global deformations emerge and develop. Of course, this only occurs in elastic-plastic columns if f_y is "high enough" to allow for the above emergence and/or development (otherwise, plasticity kicks in and precipitates a local failure before distortional and global deformations become significant).

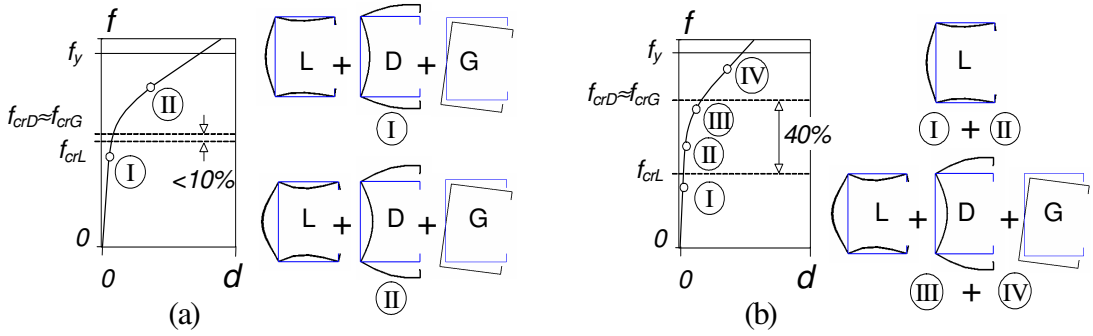

Figure 53: Equilibrium paths and cross-section buckled shapes of lipped channel columns exhibiting (a) true and (b) secondary distortional/global-bifurcation L-D-G interaction

Finally, it must be pointed out that the column and beam D-G and L-D-G interaction phenomena addressed in this work often really involve flexural-torsional-distortional critical buckling modes, even if they are termed here "global" (Camotim & Dinis 2011, Martins *et al.* 2018c). In columns, the presence of anti-symmetric distortion (GBT deformation mode **6**) is responsible for a significant decrease in post-buckling stiffness, with respect to that of columns buckling in flexural-torsional modes – it may even cause unstable elastic behavior in columns that are not fixed-ended (Camotim & Dinis 2013). Beams, on the other hand, symmetric distortional deformations (GBT deformation mode **5**) provide added post-buckling stiffness, with respect to that exhibited by beams buckling in flexural/lateral-torsional modes. In addition, the design procedures developed for beams undergoing L-D or D-G interaction are based on the DSM-based distortional strength curve proposed by Martins *et al.* (2017b) and addressed in Section 3.3 (instead of the currently codified design curve – AISI 2016).

7.2 Methodology

The investigation on the behavior and DSM design of columns or beams undergoing a particular coupling phenomenon involving distortional buckling comprises the performance of the following successive tasks:

(I) Member Geometry Selection. The first step in an investigation on a particular coupling phenomenon consists of selecting/identify column or beam geometries (cross-section shape/dimensions and lengths) prone to "true" or "secondary bifurcation" interaction. This selection is made through a "trial-and-error" procedure involving sequences of elastic linear buckling/bifurcation analyses involving members exhibiting a given cross-section shape and gradually varying cross-section dimension ratios and/or lengths. In most cases, such buckling/bifurcation analyses are performed using the code GBTUL (Bebiano *et al.* 2018a).

(II) Determination of Most Detrimental Initial Geometrical Imperfection Shape. A very important issue in mode interaction investigations is the identification of the most detrimental initial imperfection shape, in the sense that it leads to the lowest member strength. Due to the presence of two or three competing critical buckling modes, the commonly used approach of considering critical-mode initial imperfections ceases to be well defined, since infinite shapes satisfy this condition. Therefore, it is necessary to obtain and compare equilibrium paths of members containing initial geometrical imperfections (i) spanning the whole critical-mode shape range and (ii) sharing a common amplitude (otherwise, no meaningful comparison can be made). A systematic approach to identify such initial geometrical imperfection shape has been devised and the interested reader can find its detailed description in the work of Camotim & Dinis (2011). It involves (i) determining the pure critical buckling mode shapes, normalized to exhibit a unit maximum displacement, (ii) scaling the above pure modes, so that they exhibit pre-established magnitudes, which may differ for local, distortional and global imperfections, (iii) obtaining sets of initial geometrical imperfection shapes that consist of linear combination of the scaled competing buckling modes shapes and span the whole critical-mode (2-D or 3-D) space, and (iv) perform elastic post-buckling analyses of members containing the various initial geometrical imperfections obtained (all sharing the same amplitude).

(III) Investigation on the Underlying Mechanics. In order to shed new light on the mechanics underlying a given coupling phenomenon, GBT-based geometrically non-linear analyses are performed. Taking advantage of their unique modal features, it is possible (i) to provide a structural characterization of the mode interaction under consideration, (ii) to make a clear mechanical distinction between the "true" and "secondary bifurcation" interactive behaviors, (iii) to make an in-depth assessment of the influence of the initial geometrical imperfection shape, and (iv) to detect and explain "false interactive behaviors" that are associated with the emergence of global deformations stemming from the normal stress redistribution due to high local/distortional deformations (*e.g.*, Martins *et al.* 2018c). This knowledge is acquired through the in-depth study of the evolutions, as loading progresses, of the GBT deformation mode contributions to the longitudinal profiles of displacement components playing a key role in the member deformed configuration (Martins *et al.* 2018b).

(IV) Assembly of Ultimate Strength Data. Once the mechanics underlying a given coupling phenomenon are well understood, on the basis of GBT-based numerical results[38], it is essential to acquire experimental results, either collected from the literature or obtained from test campaigns planned and carried out with this specific purpose, intended to provide (i) experimental evidence of the interactive behavior under consideration and (ii) ultimate strength data to be used in the calibration of shell finite models and the search for efficient design approaches against the interactive failures. The calibrated numerical models are then used to perform parametric studies, aimed at gathering extensive ultimate strength data concerning members with a wide variety of geometries and covering large slenderness ranges – these data are essential to develop the aforementioned efficient design approaches.

[38] Before the development and numerical implementation of the GBT non-linear formulation reported by Martins *et al.* (2018b), the knowledge on the coupling phenomenon mechanics was acquired through shell finite element results (naturally, less clarifying).

(V) Development and Assessment of DSM-Based Design Approaches. Finally, the experimental and numerical ultimate strength data assembled, concerning columns or beams undergoing a particular coupling phenomenon, are used to search for and assess the merits of efficient DSM-based design approaches capable to handle the associated interactive failures. Generally speaking, the search for such a design approach follows the procedure currently adopted in AISI (2016) for the design against local-global interactive failures, which was first suggested by Schafer (2002) and later carried a step further by Yap & Hancock (2011). The comparison between the gathered ultimate strengths and their estimates provided by the developed/proposed DSM-based design approach makes it possible to assess its merits (safety and reliability). In particular, the expressions included in the current North American Specification (AISI 2016) are employed to obtain the LFRD resistance factors ϕ associated with the available set of failure-to-predicted ultimate strength ratios.

7.2.1 Geometry selection – beams under L-D interaction

The identification of uniformly bent beam geometries prone to L-D interaction is quite straightforward, since there exist a fair number of short-to-intermediate beams with close local and distortional buckling moments. In order to illustrate the geometry selection procedure, Figure 54(a_1) shows, for lipped channel beams bent about the major-axis with cross-section dimensions b_w=100, b_f=65, b_l=12.5 and t=1.0mm and SCA boundary conditions (see Section 3.3), the variation of the single half-wave ($M_{b.1}$) and critical (M_{cr}) buckling moments with the length L (logarithmic scale). On the other hand, Figure 54(a_2) displays the M_{cr} vs. L signature curve again, together with GBT-based "approximate" buckling curves obtained from analyses including three deformation mode sets, namely modes **7-17** (local), **5+6** (distortional) and **3+4** (global: lateral-torsional). Since the first two analyses yield (i) practically exact critical local buckling moments and (ii) slight overestimations of the critical distortional buckling moments, respectively, Figure 54(a_2) readily shows that beams with lengths such that 45<L<250cm are highly prone to L-D interaction (the global critical buckling moments are much higher) – this quite large length interval evidences the relevance of this coupling phenomenon. Figure 54(b) shows the local and distortional critical buckling modes of the L=L_{DL}=50cm beam, with very close local and distortional buckling moments (201kNcm vs. 203kNcm) – they exhibit 8 and one half-waves, respectively. Naturally, the post-buckling behavior (elastic or elastic-plastic) of such beam is bound to be strongly affected by L-D interaction. Concerning the signature curve descending branch, it falls a bit below the solution obtained with only modes **3+4** (exact lateral-torsional buckling moments) – the gap reflects the fact that, for the associated lengths, the beam "global" critical buckling mode contains distortional deformations (see the last paragraph in Section 7.1). Moreover, beams with lengths close to the transition between the signature curve "horizontal plateau" and descending branch are prone to L-D-G interaction (the global critical buckling moments are much closer).

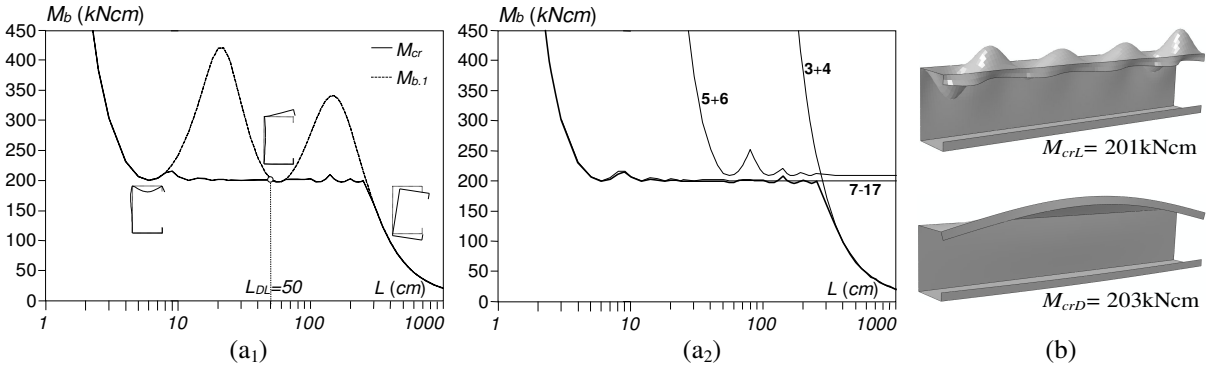

Figure 54: Lipped channel beam (a_1) signature (M_{cr} vs. L) and single half-wave buckling ($M_{b.1}$ vs. L) curves, (a_2) M_{cr} vs. L curve and its GBT-based local/distortional/global "approximations", and (b) L_{DL}=50cm beam local/distortional critical buckling modes

The output of this selection were 43 lipped channel, hat-section and zed-section beam geometries, which can be found in Martins *et al.* (2017c), both for SCA and SCB support conditions. All these beams (i) exhibit $R_{DL}=M_{crD}/M_{crL}$ values in the range $0.50 \leq R_{DL} \leq 2.00$ and (ii) have global buckling moments (M_{crG}) much higher than both their local and distortional counterparts ($M_{crG}/M_{cr.Max} >> 1.0$, where $M_{cr.Max}=max\{M_{crD};M_{crL}\}$) and the yield moments ($M_{crG}/M_{y.Max} >> 1.0$), thus ensuring that no interaction with global buckling occurs. Local buckling is always triggered by the compressed flange (most common situation in practice) and, in order to study the effect of strong ("true") L-D interaction, 26 beams were selected in the $0.85 < R_{DL} < 1.15$ range – the remaining 17 beams were obtained by varying this ratio in 0.10/0.05 steps up to 2.00 and down to 0.50, respectively, making it possible to investigate also "secondary (local or distortional) bifurcation" L-D interaction.

7.2.2 Most detrimental initial imperfection – columns under D-G interaction

The procedure outlined in Section 7.2 (item (II)) was applied to identify the most detrimental initial geometrical imperfection shape in columns affected by D-G interaction (Martins *et al.* 2018d). The numerical results presented concern fixed-ended zed-section columns with length L=625cm and cross-section dimensions b_w=140, b_f=140, b_l=13 and t=3.55mm, corresponding to very close critical distortional and "global"[39] buckling loads (R_{GD}=0.95 – strong "true" D-G interaction). The initial imperfection shapes considered consist of linear combinations of the normalized pure distortional (10 half-waves) and "global" (one half-wave) buckling mode shapes, and share the same overall amplitude. A given imperfection shape is associated with coefficients $v_{D.0}$ and $v_{G.90}$ lying on the ellipse depicted in Figure 55(a), which covers every possible combination – it lies on this ellipse and corresponds to an angle θ, measured counter-clockwise from the $v_{D.0}$ axis, so that $v_{D.90}=r\sin\theta$ and $v_{D.0}=r\cos\theta$ (r is the ellipse polar coordinate). The amplitudes of the pure distortional (θ=0º or θ=180º – Fig. 55(b)) and "global" (θ=90º or θ=270º – Fig. 55(b)) initial imperfections are equal to 0.94t (50% probability that a random imperfection amplitude is below this value – Schafer & Peköz 1998) and L/1000, respectively.

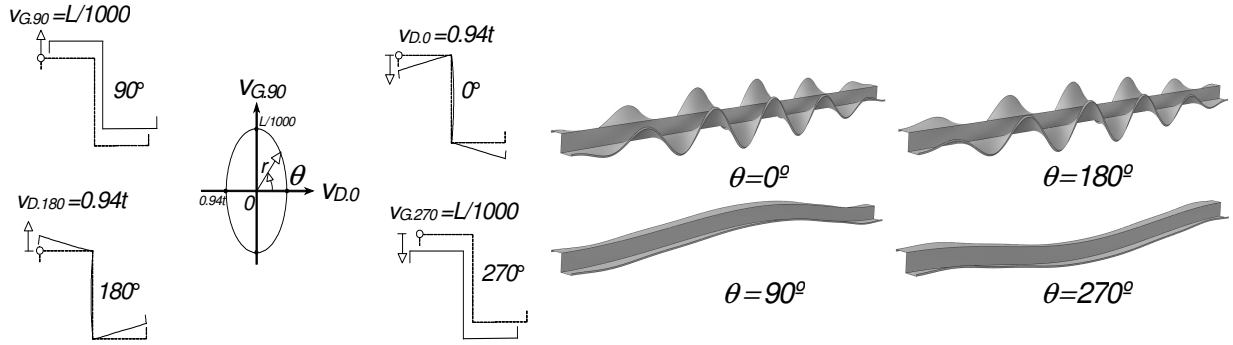

(a) (b)

Figure 55: Initial imperfection (a) $v_{D.0}$-$v_{G.90}$ plane representation and (b) θ=0º, 90º, 180º, 270º shapes

After having defined "the full set of possible initial geometrical imperfections", it becomes possible to assess and compare the elastic post-buckling behaviors of columns containing them, in order to (i) obtain numerical evidence of the occurrence of D-G interaction, (ii) assess how the initial imperfection shape influences the column post-buckling behavior and (iii) identify the most detrimental one. This was done for 24 initial imperfection shapes (15º θ intervals, starting at 0º, in Fig. 55(a)) and Figure 56(a) shows the corresponding elastic equilibrium paths P/P_{cr} vs. $(v+v_0)/t$ (v is the mid-span top flange-lip corner vertical

[39] This column critical buckling mode involves not only predominant minor-axis flexure (as expected) but also a small (but clearly visible) contribution from the symmetric distortional mode **5** – it is, in fact, a flexural-distortional mode (Martins *et al.* 2018d).

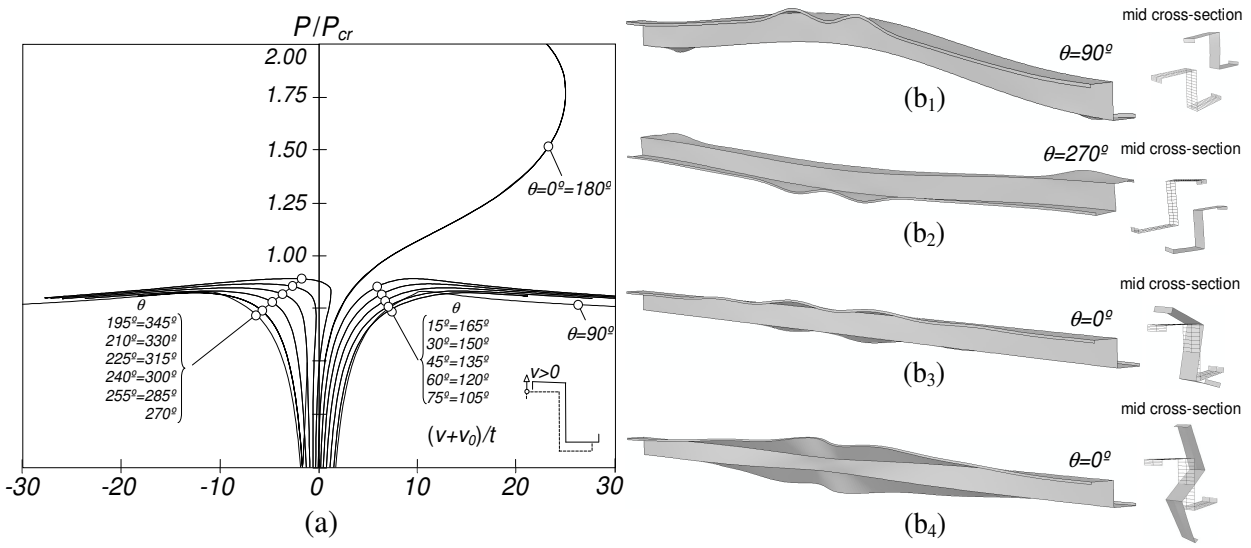

Figure 56: Zed-column (a) elastic post-buckling equilibrium paths P/P_{cr} vs. $(v+v_0)/t$ and (c) deformed configurations at advanced post-buckling stages for (b_1) θ=90º + $(v+v_0)/t$=30, (b_2) θ=270º + $(v+v_0)/t$=30, (b_3) θ=0º + $(v+v_0)/t$=10 and (b_4) θ=0º + $(v+v_0)/t$=25

displacement and v_0 the corresponding initial value) of the θ=0º, 15º,..., 345º columns. Moreover, Figure 56(b) shows several column deformed configurations at advance post-buckling stages. The observation of these post-buckling results leads to the followings conclusions:

(i) Most equilibrium paths are associated with deformed configurations combining a predominant "global" half-wave with several distortional half-waves, thus evidencing the occurrence of D-G interaction – *e.g.*, Figures 56(b_1)-(b_2) show the θ=90º and θ=270º column deformed configurations at advanced post-buckling stages ($(v+v_0)/t$=30). As expected, all these columns exhibit a very small post-critical strength and fail below the critical buckling load level (P_u/P_{cr}<1.0).

(ii) The equilibrium paths can be divided into three groups: (ii_1) θ=0º and θ=180º (discussed in the next item), (ii_2) 195º≤θ≤345º, associated with minor-axis flexural deformations towards the bottom flange (denoted "negative") and (ii_3) all the remaining ones (15º≤θ≤165º), involving almost exclusively "positive" minor-axis flexural deformations. Note that distinct initial imperfection amplitudes may lead to significantly different column post-buckling behavioral features (Dinis & Camotim 2011).

(iii) Surprisingly, the equilibrium paths of the columns with pure distortional initial imperfections (θ=0º and θ=180º) clearly differ from those of all the other columns. Figures 56(b_3)-(b_4) show deformed configurations of the θ=0º column at $(v+v_0)/t$=10 and 25, providing evidence that these columns are affected by D-G interaction of a different nature, involving distortional deformations and torsional rotations. This type of interaction is not due to the closeness between the distortional and torsional buckling loads. In fact, GBT-based results (Martins *et al.* 2018e) show that torsional rotations may emerge in columns either exhibiting a pure distortional post-buckling behavior or affected by D-G interaction, even when the critical torsional and minor-axis flexural buckling loads are not very close.

(iv) Since all equilibrium paths exhibit limit points prior to merging into "common curves" (except those addressed in the previous item), the most detrimental initial imperfection can be easily identified: that leading to the lowest failure load. Figure 56(a) shows that the θ=75º; 105º; 255º; 285º initial imperfections are the most detrimental (they correspond to P_u/P_{cr}=0.825). Nevertheless, it should be mentioned that P_u/P_{cr} is practically the same for the columns with pure "global" initial imperfections – therefore, for the sake of simplicity, it is perfectly acceptable to assume that the pure "global" initial imperfections are the most detrimental one.

7.2.3 Underlying mechanics – beams under D-G interaction

A GBT-based investigation on the elastic post-buckling behavior of a simply supported lipped channel beam subjected to uniform major-axis bending and undergoing "secondary global-bifurcation D-G interaction" is addressed (Martins *et al.* 2018a). The results are obtained by means of geometrically non-linear imperfect analyses based on a beam finite element formulation recently derived and numerically implemented by Martins *et al.* (2018b) and concern a beam with a critical (distortional) initial geometrical imperfection. This beam has length L=200cm and cross-section dimensions b_w=190, b_f=90, b_l=10 and t=3.06mm, leading to a critical global-to-distortional buckling moment ratio $R_{GD}\approx$2.00 – critical buckling modes with 5 (distortional) and one (global) half-waves. The GBT nodal discretization adopted involves 17 nodes (6 natural and 11 intermediate – 3 in the top/compressed flange, 1 in the bottom/tensioned flange and 7 in the web), corresponding to (i) 19 conventional (4 global, 2 distortional and 13 local – **1**-**19**), (ii) 16 shear (5 global and 11 local – **20**-**35**, (iii) 16 linear transverse extension (1 global isotropic, 4 global deviatoric and 11 local – **36**-**51**), and (iv) 16 quadratic transverse extension deformation modes (**52**-**67**) – a total of 67 deformation modes. The beam critical distortional and global buckling modes contain essentially contributions from deformation modes **5**+**6** and **3**+**4**, respectively.

Figures 57(a)-(b) show two M/M_{crD} vs. $(v+v_0)/t$ equilibrium paths of a beam containing initial geometrical imperfections akin to the critical distortional buckling mode, with amplitude 0.1t, and the associated modal participation diagram – for comparison purposes, ABAQUS SFE results are also included. As for Figures 58(a_1)-(b_4) and 59, they display (i) the evolution, as loading progresses, of the longitudinal profiles, due to various deformation modes/mode sets, of the top flange-lip corner vertical and mid-web transverse displacements, and (ii) beam deformed configurations at M/M_{crD}=0.507;0.919;0.701$^{\downarrow}$;0.484$^{\downarrow}$ – the vertical arrows identify equilibrium states located on the equilibrium path descending branch. These post-buckling results make it possible to draw the following conclusions:

(i) There is an excellent agreement between the GBT-based equilibrium paths, obtained with all the 67 deformation modes included, and that yielded by the shell finite element analysis – they are virtually coincident in the whole ascending branch and first part of the descending branch. In the second part of the equilibrium path descending branch, a GBT longitudinal discretization involving 16 finite elements (instead of 8) slightly improves the accuracy of the results.

(ii) The modal participation diagram shows two clearly distinct regions, before and after the equilibrium path limit point ($M/M_{crD}\approx$0.919). Initially, the beam deformed configuration combines essentially participations from modes **2** (mostly) and **5**+**6** (stemming from the initial geometrical imperfections) – up to M/M_{crD}=0.919, p_2 decreases from 95% to 56% and p_{5+6} increase from 4% to 27%. At M/M_{crD}=0.837, the mode **3** and **4** participations, barely perceptible until then, quickly rise from 1% each to 7% and 9%, respectively (at M/M_{crD}=0.919). Along the equilibrium path descending branch, mode **2** is fast "replaced" by modes **3** and **4** – participations of 26% and 36% at M/M_{crD}=0.473$^{\downarrow}$. Conversely, p_{5+6} reaches a peak value of 28% at M/M_{crD}=0.900$^{\downarrow}$ and then decreases continuously until M/M_{crD}=0.473$^{\downarrow}$ (p_{5+6}=14.1%). As for the joint participation of the local and shear modes, it never exceeds 2%. Finally, the joint participation of all transverse extension modes becomes more relevant as loading progresses: it reaches a maximum of 5% at M/M_{crD}=0.473$^{\downarrow}$ and consists mostly of contributions from modes **36** (1.7%), **39** (0.5%), **40** (1.3%).

(iii) All the displacement profiles displayed in Figures 58(a_1)-(b_4) are longitudinally symmetric, which is due to the fact that the critical distortional buckling mode (and the initial geometrical imperfection) has an odd half-wave number. Figure 57(b) shows that, at the early loading stages, the beam deformed configuration consists of a dominant single half-wave (downward) contribution from

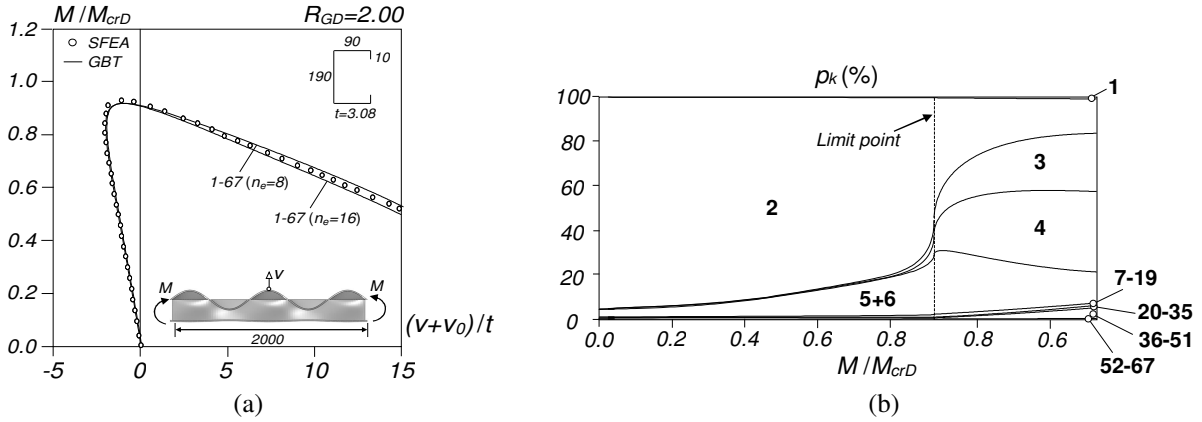

Figure 57: (a) M/M_{crD} vs. $(v+v_0)/t$ equilibrium paths of a lipped channel beam undergoing "secondary global-bifurcation D-G interaction" with a distortional initial geometrical imperfection, and (b) corresponding modal participation diagram

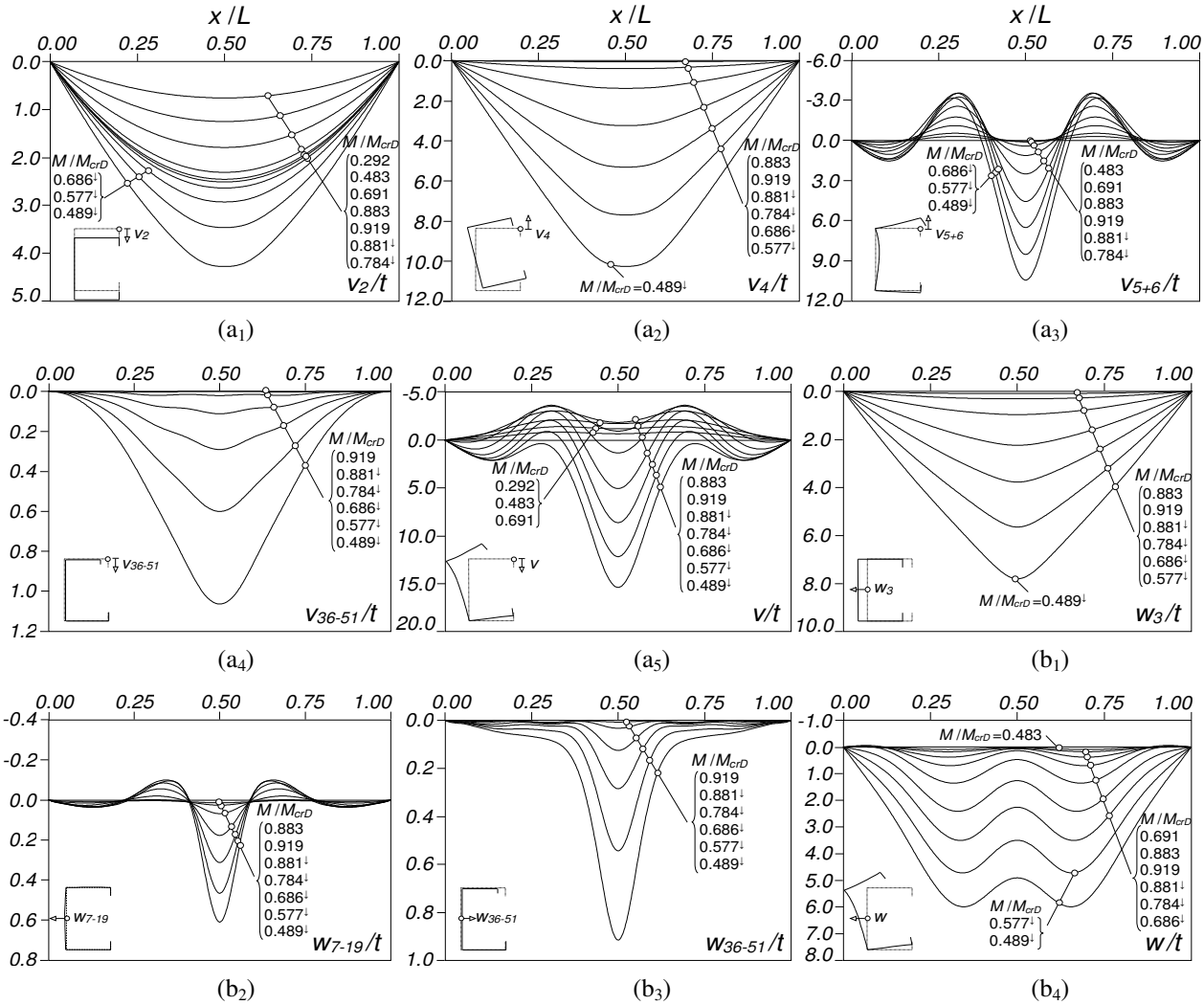

Figure 58: R_{GD}=2.00 lipped channel beam profiles of (a) top flange-lip corner vertical displacements $(_1)$ $v_{\mathbf{2}}(x)$, $(_2)$ $v_{\mathbf{4}}(x)$, $(_3)$ $v_{\mathbf{5+6}}(x)$, $(_4)$ $v_{\mathbf{36\text{-}51}}(x)$, $(_5)$ $v_{\mathbf{1\text{-}67}}(x)\equiv v(x)$, and (b) mid-web transverse displacements $(_1)$ $w_{\mathbf{3}}(x)$, $(_2)$ $w_{\mathbf{7\text{-}19}}(x)$, $(_3)$ $w_{\mathbf{36\text{-}51}}(x)$, $(_4)$ $w_{\mathbf{1\text{-}67}}(x)\equiv w(x)$

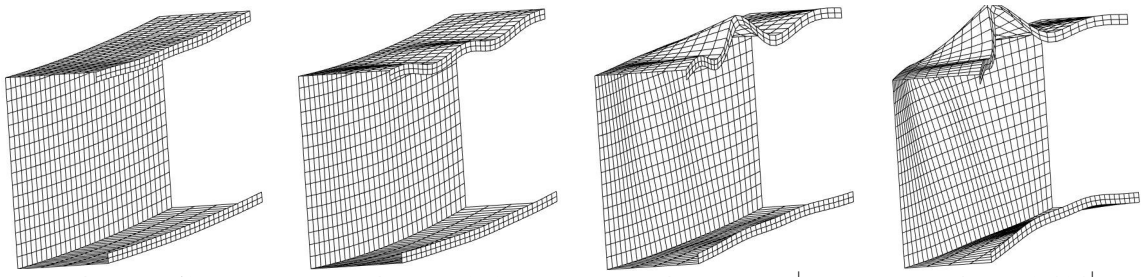

Figure 59: Lipped channel beam GBT-based deformed configurations at loading stages M/M_{crD}=0.507, 0.919, 0.701$^{\downarrow}$, 0.484$^{\downarrow}$

mode **2** (Fig. 58 (a_1)) and a 5 half-wave contribution from modes **5+6** (Fig. 58(a_3)). As loading progresses, the distortional deformations become more pronounced, originating a stress redistribution that causes the emergence of modes **3** and **4** – this also occurs in beams exhibiting a "pure" distortional post-buckling behavior (Martins *et al.* 18a). This emergence favors the interaction with global buckling, since M_{crG}/M_{crD} is not high enough to preclude such interaction. Once these global buckling modes are triggered, they became progressively more relevant, as depicted in Figures 58(a_2)+(b_1) (and also in Fig. 57(b)) – for M/M_{crD}<0.919$^{\downarrow}$, the dominance of $v_4(x)$ (Fig. 58(a_2)) in $v(x)$ (Fig. 58(a_5)) and of $w_3(x)$ (Fig. 58(b_1)) in $w(x)$ (Fig. 58(b_4)) are very clear. Note still that, for M/M_{crD}<0.919$^{\downarrow}$, the initially equal five distortional half-waves become progressively more unequal: the outward central half-wave is much more pronounced (see Fig. 58(a_3)), due to the "attractive power" of the single half-wave mode **4** participation – *i.e.*, the global buckling behavior plays a dominant role even when M_{crD}<M_{crG}. Finally, the tiny contributions from the local (Fig. 58(b_2)) and transverse extension (Figs. 58(a_4)+(b_3)) deformation modes follow similar trends.

(iv) There is no clear difference between the post-buckling behaviors of beams affected by "secondary global-bifurcation" and "true" and D-G interaction – the results concerning the latter can be found in Martins *et al.* (2018a). Indeed, modes **3** and **4**, associated with M_{crG}, emerge at fairly early loading stages for beams exhibiting either R_{GD}>1.00 or R_{GD}>>1.00 – in the latter case, exclusively due to the stress redistribution caused by the distortional deformations (not the closeness between M_{crG} and M_{crD}). This means that all these beams are affected by qualitatively similar D-G interaction effects, even if their origins may be distinct. This is why it was decided to term this type of D-G interaction as "secondary global-bifurcation D-G interaction" also when is does not stem from nearly coincident M_{crG} and M_{crD} values. This type of D-G interaction is always relevant for design purposes – in fact, much more so than anticipated (Martins *et al.* 2018c).

(v) Despite the distortional initial geometrical imperfections, distortional deformations and torsional rotations become visible at approximately the same loading stages: see Figures 58(a_2)-(a_3) and the first two deformed configurations in Figure 59. Moreover, their visibility increases considerably and gradually along the equilibrium path descending branch: the last two deformed configurations in Figure 59 provide very clear graphic evidence of the occurrence of D-G interaction, as attested by the dominance of both the torsional rotations and the top flange distortional deformations.

7.2.4 Ultimate strength data – columns under L-D interaction

Although a few test campaigns were carried out with the specific aim of investigating L-D interaction in fixed-ended cold-formed steel columns, exhibiting both "plain" and intermediately stiffened lipped cross-sections, the specimens providing clear experimental evidence of this coupling phenomenon and ensuing failure load erosion are fairly scarce – certainly, much less than those collected to propose/calibrate the existing L, D, G and L-G DSM design curves/expressions (Schafer 2008). The available experimental

studies on L-D interaction in fixed-ended CFS columns are due to (i) Kwon & Hancock (1992), Young & Rasmussen (1998), Kwon *et al.* (2009) and Young *et al.* (2013), for lipped channel (C) columns, (ii) Kwon *et al.* (2005), for hat-section (H) columns, (iii) Dinis *et al.* (2014), for rack-section (R) columns, (iv) Kwon & Hancock (1992), Kwon *et al.* (2009), Yap and Hancock (2011) and He *et al.* (2014), for web-stiffened lipped channel (WSC) columns, and (v) Yang & Hancock (2004), for web/flange-stiffened lipped channel (WFSC) columns – no zed-section (Z) column test results were found in the literature. Figures 60(a)-(d) concern tests carried out at the University of Hong Kong, which were carefully planned in close cooperation with researchers from the University of Lisbon and involved fixed-ended C and R columns. They provide (i) front and side views of the test rig and a typical set-up for testing a fixed-ended column, including the load application (through a servo-controlled hydraulic testing machine) and the transducers to measure mid-span cross-section displacements, and (ii) experimental evidence of the occurrence of L-D interaction in lipped channel and rack-section specimens (Young *et al.* 2013, Dinis *et al.* 2014). In "plain" cross-section columns, local buckling is almost always triggered by the web, where most of the L-D interaction takes place. This ceases to be true in the presence of web intermediate stiffeners (*e.g.*, WSC columns), as local buckling is bound to be triggered by the flanges, thus altering the

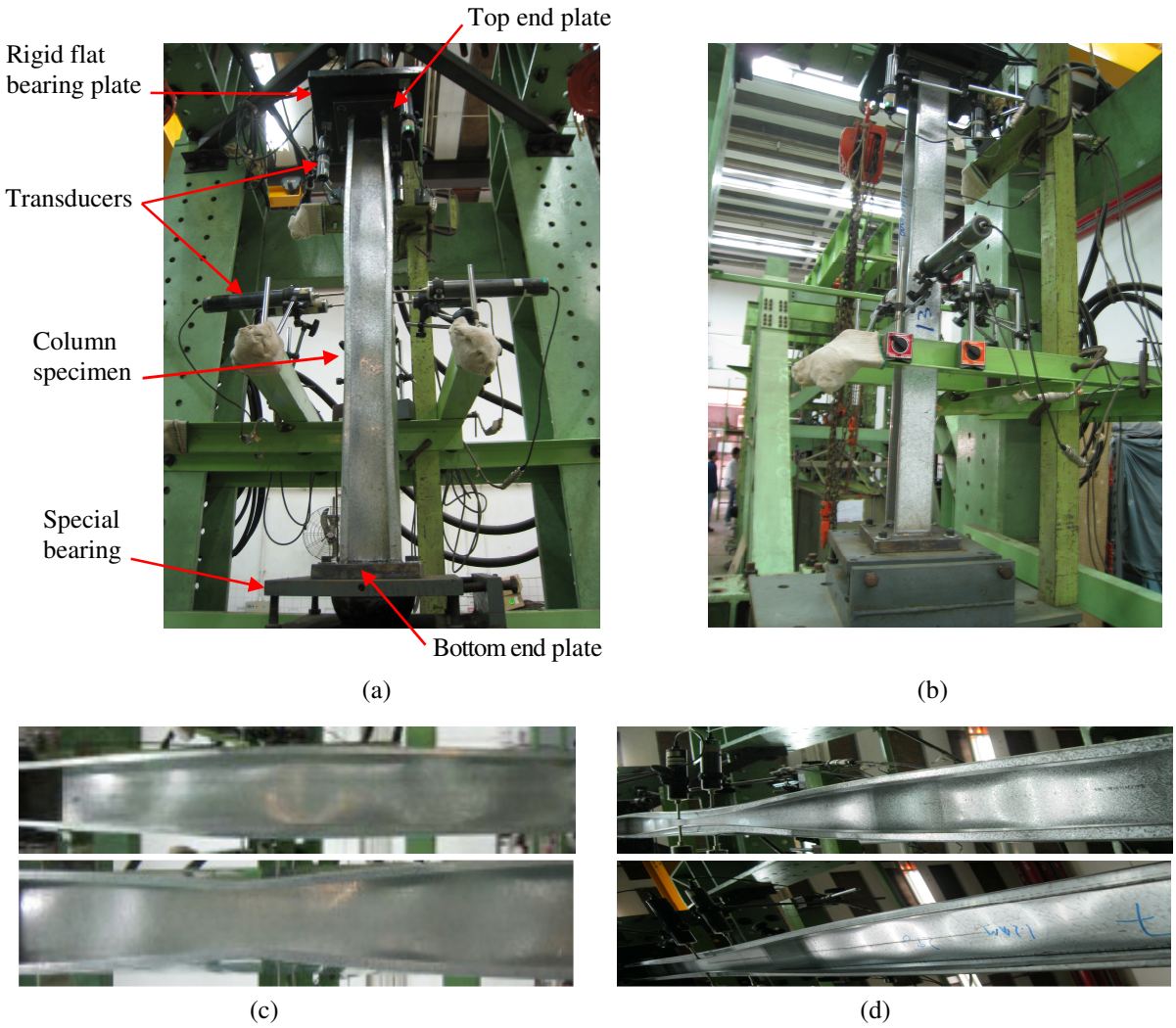

Figure 60: University of Hong Kong tests: (a) front and (b) side views of test rig and set-up, and experimental evidence of L-D interaction in (c) lipped channel and (d) rack-section columns

Table 3: Summary of the test results available in the literature on cold-formed steel columns undergoing L-D interaction

	SLB	N	TI	N	SDB	N
PCS			Kwon & Hancock (1992) Kwon *et al.* (2005)	5 5	Loughlan *et al.* (2012 Kwon *et al.* (2009)	20 3
WSC	Yap & Hancock (2011) He *et al.* (2014)	2 4	Kwon & Hancock (1992) Yap & Hancock (2011) He *et al.* (2014) Kwon *et al.* (2009)	3 9 8 7	He *et al.* (2014) Kwon *et al.* (2009)	5 3
WFSC			Yang & Hancock (2004)	5	Yang & Hancock (2004)	7
Total		6		42		38

L-D interaction features. Table 3, taken from Martins *et al.* (2017a), summarizes the above column test results. Using reported geometrical and material properties to obtain the critical local/distortional/global buckling and squash loads of the tested specimens, these results are divided into nine sets, according to the (i) cross-section geometry (plain, web-stiffened lipped channel or web/flange-stiffened lipped channel – PCS, WSC or WFSC) and (ii) L-D interaction nature (secondary local-bifurcation, true interaction or secondary distortional-bifurcation – SLB, TI or SDB) – N stands for the number of test results. It is readily concluded that there are only sizeable test result numbers for (i) PCS columns failing under SDB L-D interaction (23) and (ii) WSC columns collapsing due to TI L-D interaction (27) – otherwise, the test results are either scarce or null. It is worth noting that an experimental test program is planned to be carried out at the University of Hong Kong, involving WSC and WFSC columns with geometries selected to ensure SLB, TI and SDB L-D interaction – these test results will help "fill the gaps" in Table 3.

Extensive parametric studies were performed in the last few years, by means of ABAQUS SFEA, in order to obtain numerical failure loads to complement the experimental failure load data presented in Table 3. The modeling issues involved in the above numerical parametric studies, not addressed here, can be found, for instance, in Silvestre *et al.* (2012). The set of columns analyzed comprises (i) C columns such that $0.9 \leq R_{DL}=P_{crD}/P_{crL} \leq 1.0$ (TI) and $0.4 \leq R_{DL} \leq 2.4$ (SLI, TI, SDI), reported by Silvestre *et al.* (2012) and Martins *et al.* (2015), respectively, (ii) H, Z and R columns such that $0.9 \leq R_{DL} \leq 1.0$ (TI) and $0.4 \leq R_{DL} \leq 2.4$ (SLI, TI, SDI), reported by Dinis & Camotim (2015b) and Martins *et al.* (2015), respectively, (iii) WSC columns such that $0.4 \leq R_{DL} \leq 2.4$ (SLI, TI, SDI), reported by Martins *et al.* (2016), and (iv) WFSC

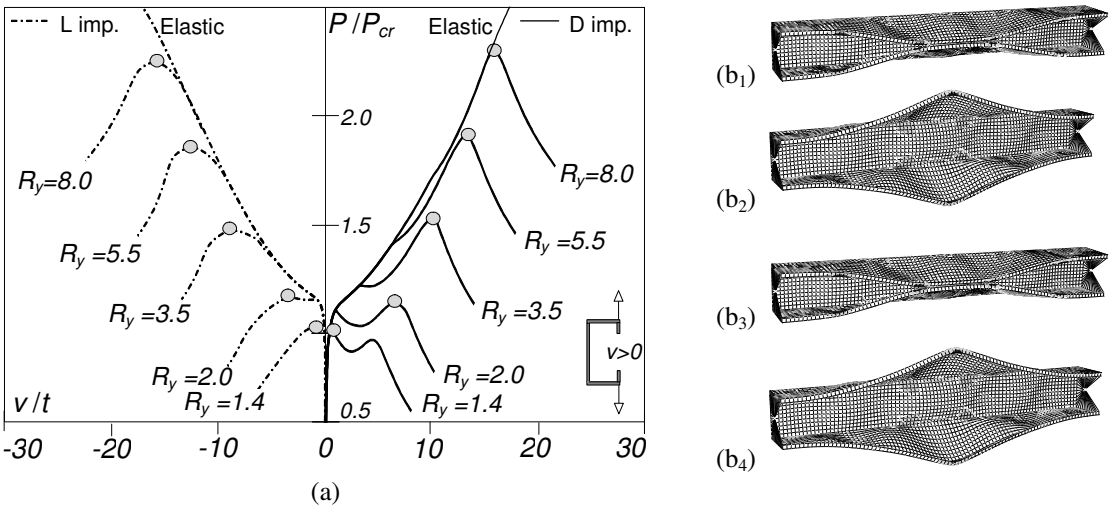

(a)

Figure 61: (a) P/P_{cr} vs v/t paths of C columns with R_{DL}=1.13 and containing D or L initial imperfections, and (b) failure modes and plastic strain diagrams of the (b_1)-(b_4) R_y=2.0+L, R_y=2.0+D, R_y=5.5+L and R_y=5.5+D columns

columns such that $0.4 \leq R_{DL} \leq 2.0$ (SLI, TI, SDI), reported by Martins *et al.* (2017d) – a total of more than 2000 values, corresponding to critical (local or distortional) slenderness values ranging from 1.00 to 3.50. Figure 61(a) shows the upper portions ($P/P_{cr}>0.5$) of the elastic-plastic P/P_{cr} vs v/t equilibrium paths concerning lipped channel columns with $R_{DL}=1.13$ and exhibiting (i) distortional or local (critical) initial geometrical imperfections and (ii) six yield stresses, so that $R_y=f_y/f_{cr.max}=1.4, 2.0, 3.5, 5.5, 8.0$ and ∞ (elastic behavior). As for Figures 61(b), they show deformed configurations and plastic strain distributions near collapse concerning columns with (i) $R_y=2.0$ and L (Fig. 61(b_1)) or D (Fig. 61(b_2)) imperfections, and (ii) $R_y=5.5$ with L (Fig. 61(b_3)) or D (Fig. 61(b_4)) imperfections – the deformed configurations are amplified 10 or 2.5 times (D or L imperfections). The observation of these post-buckling results prompts the following remarks (Martins *et al.* 2015):

(i) Unlike the columns with D initial imperfections, which always exhibit outward mid-span flange-lip motions (akin to the initial imperfection shape), all columns with L initial imperfections display inward mid-span flange-lip motions. This surprising feature is due to the presence of minor-axis bending, due to effective centroid shifts towards the web caused by stress redistribution (Young & Rasmussen 1999, despite the fixed end supports). The associated outward web curvature "attracts" mid-span inward distortional deformations, which explains the failure modes in Figs. 61(b_1) and (b_3).

(ii) In the columns with R_y closest to 1.0 ($R_y=1.4$), yielding starts when the normal stress distribution is still "not too far from uniform" and, therefore, precipitates a rather abrupt collapse, which occurs for a load that is practically imperfection-independent.

(iii) In the columns with $R_y>1.4$, on the other hand, first yielding takes place when the normal stress distribution is already "clearly non-uniform" and, therefore, does not lead to an immediate failure – collapse occurs either (iii_1) after a snap-through phenomenon and subsequent strength increase up to a limit point (columns with D imperfections) or (iii_2) following a fairly smooth stiffness decrease (columns with L imperfections). As R_y increases, the snap-through becomes less pronounced (it eventually disappears) and the elastic-plastic strength reserve grows considerably, because first yielding occurs at gradually more localized regions, thus impacting less the column stiffness – this can be confirmed by comparing the various R_y equilibrium paths of columns with D-imperfections.

(iv) In the columns with D imperfections and $R_y<3.5$ collapse occurs very soon after the yielding of the cross-section lips near the maximum outward distortional crest (*e.g.*, $R_y=2.0$+D – see Fig. 61(b_2)). As R_y increases, collapse occurs at a later stage, after the web-flange corner regions of the central $L/3$ segment have already yielded – see Figure 61(b_4).

(v) Columns with L imperfections and $R_y \leq 2.0$ reach the ultimate strength when the lip free end regions of the outer half-wave most deformed cross-sections have yielded – *e.g.*, see Figure 61(b_1), concerning the $R_y=2.0$+L column. For higher R_y values, collapse occurs again at a later stage, when the lip free end and web-flange corner regions of the central $L/3$ segment have also yielded – see, for instance, Figure 61(b_3), concerning the $R_y=5.5$+L column.

(vi) Regardless of the initial imperfection shape and R_y value, all columns with $R_y \geq 2.0$ exhibit visible L-D interaction. Moreover, note that the failure mode does not depend on R_y – *e.g.*, compare Figures 61(b_2) and (b_4), which show the collapse mechanisms of the $R_y=2.0$+D and $R_y=5.5$+D columns.

7.2.5 DSM design – columns under L-D-G interaction

In the first stages, the search for a DSM-based design approach to predict the ultimate strength of cold-formed steel columns failing in local-distortional-global interactive modes focused exclusively on plain lipped channel columns (Dinis *et al.* 2017). All available failure load data concerning columns affected by this particular coupling phenomenon were assembled, comprising (i) 52 experimental failure loads,

reported by Young & Rasmussen (1998 – 2 tests), Kwon *et al.* (2009 – 5 tests), Santos *et al*. (2012, 2014 – 12 and 16 tests, respectively) and Young *et al*. (2017 – 17 tests), and (ii) 893 numerical failure loads, obtained by Dinis *et al*. (2012b, 2017) and Cava *et al*. (2016). Then, following the procedure adopted in the currently codified DSM column design curve against L-G interactive failures (P_{nLG}), which was first suggested by Schafer (2002), it is possible to develop a design approach to estimate the ultimate strength of columns failing in D-G interactive modes (P_{nDG}), by replacing P_y with P_{nG} in the currently codified DSM column design curve against pure distortional failures. Moreover, Yap & Hancock (2011) carried this reasoning one step further and argued that it should be possible to predict the failure loads of CFS columns undergoing L-D-G interaction by means of P_{nLDG} values, by replacing P_y with P_{nDG} in the currently codified DSM column design curve against pure local failures. Therefore, three expressions are available to evaluate column nominal strengths against interactive failures involving global buckling (L-G, D-G and L-D-G)– they read

$$P_{nLG} = \begin{cases} P_{nG} & if \quad \lambda_{LG} \le 0.776 \\ P_{nG}\left(\frac{P_{crL}}{P_{nG}}\right)^{0.4}\left[1-0.15\left(\frac{P_{crL}}{P_{nG}}\right)^{0.4}\right] & if \quad \lambda_{LG} > 0.776 \end{cases} \quad \text{where} \quad \lambda_{LG} = \sqrt{\frac{P_{nG}}{P_{crL}}} \quad , \quad (13)$$

$$P_{nDG} = \begin{cases} P_{nG} & if \quad \lambda_{DG} \le 0.561 \\ P_{nG}\left(\frac{P_{crD}}{P_{nG}}\right)^{0.6}\left[1-0.25\left(\frac{P_{crD}}{P_{nG}}\right)^{0.6}\right] & if \quad \lambda_{DG} > 0.561 \end{cases} \quad \text{where} \quad \lambda_{DG} = \sqrt{\frac{P_{nG}}{P_{crD}}} \quad , \quad (14)$$

$$P_{nLDG} = \begin{cases} P_{nDG} & if \quad \lambda_{LDG} \le 0.776 \\ P_{nDG}\left(\frac{P_{crL}}{P_{nDG}}\right)^{0.4}\left[1-0.15\left(\frac{P_{crL}}{P_{nDG}}\right)^{0.4}\right] & if \quad \lambda_{LDG} > 0.776 \end{cases} \quad \text{where} \quad \lambda_{LDG} = \sqrt{\frac{P_{nDG}}{P_{crL}}} \quad . \quad (15)$$

Figures 62(a)-(b) compare the three above DSM-based column nominal strengths, plotted against λ_G[40], with the failure load ratios P_u/P_y concerning the 52 experimental and 893 numerical failure loads. First of all, the observation of these results readily shows that both the numerical and experimental P_u/P_y values correlate very well and are nicely aligned along a "Winter-type" curve with a small vertical

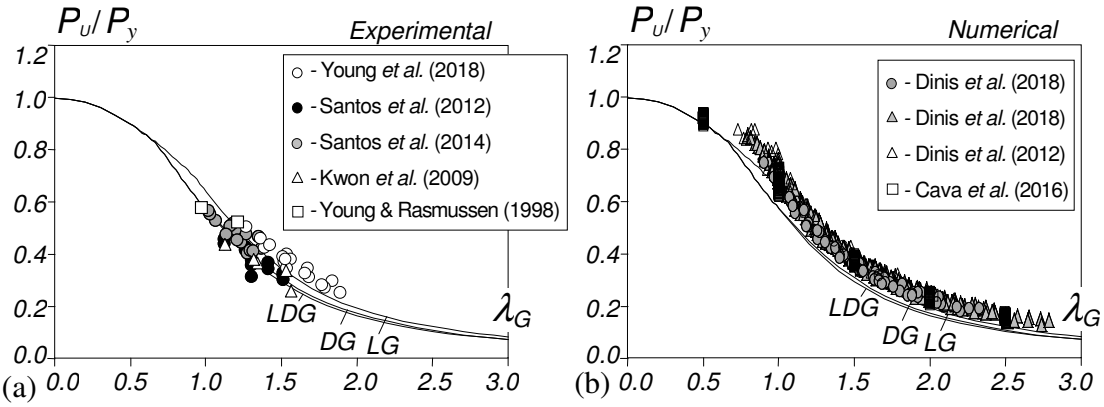

Figure 62: DSM design curves against interactive failures involving global deformations and plots of P_u/P_y against λ_G for the column failure loads obtained (a) experimentally and (b) numerically

[40] Naturally, the joint representation of the three design curves is made under the assumption that $\lambda_L \approx \lambda_D \approx \lambda_G$, which may be a crude approximation is some cases. A more accurate account would require a different plot for each design curve, thus making their comparison less clear.

dispersion. Note that the failure loads obtained during the first test campaign carried out by Santos *et al*. (2012) are generally lower than those reported by the other authors – this was due to the inability to ensure fully fixed ended support conditions during the tests (Dinis *et al*. 2017)[41].

Quite surprisingly, it was found that the currently codified DSM design curve against L-G interactive failures (P_{nLG}) provides the best failure load estimation quality. Indeed, the corresponding failure load predictions are generally safe and mostly accurate, while the other two DSM-based design approaches, P_{nDG} and P_{nLDG} (none currently codified), were shown to provide excessively safe failure load predictions (Dinis *et al*. 2017) – more so the P_{nLDG} values. Figure 63 plots, separately for the experimental and numerical failure loads, the failure-to-predicted load ratios P_u/P_{nLG} against λ_G, making it possible to confirm the above assertion: the P_{nLG} values provide mostly safe and reasonably accurate predictions of the experimental and numerical failure loads – the P_u/P_{nLG} average, standard deviation, maximum and minimum values are 1.04-0.15-1.35-0.71 (experimental failure loads) and 1.15-0.10-1.45-0.95 (numerical failure loads). Although there are several overestimations, almost all of them concerning experimental failure loads, note that the most severe ones are associated with the values obtained by Santos *et al*. (2012) – their removal would improve visibly the failure load prediction quality. It is also noted that virtually all numerical failure loads are underestimated – the underestimation increases visibly with the global slenderness λ_G. The LRFD resistance factors obtained from the P_u/P_{nLG} ratios either equal or exceed the value recommended in the North American Specification (AISI 2016) for compression members (ϕ_c=0.85). Indeed, the values obtained are ϕ_c=0.85 (experimental values), ϕ_c=1.00 (numerical values) and ϕ_c=0.99 (experimental and numerical values) – if the experimental failure loads due to Santos *et al*. (2012) were removed, the first and third resistance factors would increase to ϕ_c=0.92 and ϕ_c=1.00, respectively.

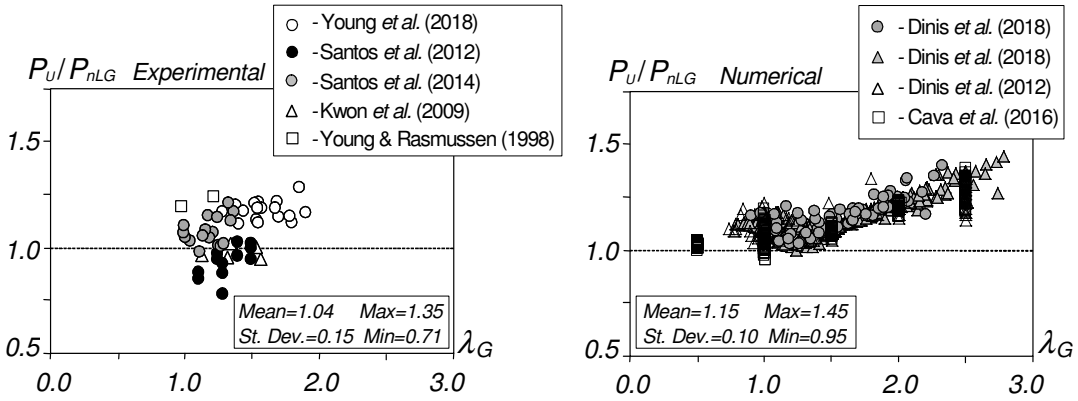

Figure 63: Plots, against λ_G, of the experimental and numerical failure-to-predicted load ratios P_u/P_{nLG}

The next step of the investigation consisted of assessing whether the above findings can be extended to cover CFS columns with other cross-section shapes that are affected by L-D-G interaction. On the basis of the results of a numerical investigation conducted by Dinis & Camotim (2016b), it was found that the P_{nLG} values provide adequate estimates for the failure loads of zed, hat and rack-section columns – Figures 64(a)-(c) show the respective P_u/P_{nLG} vs. λ_G plots. It is noted that these plots are perfectly in line with the conclusions drawn from the numerical and experimental study on lipped channel columns – the LRFD resistance factor obtained with these numerical P_u/P_{nLG} ratios are ϕ_c=0.96, ϕ_c=1.08 and ϕ_c=1.03, respectively for zed, hat and rack-section columns. However, note that there are no experimental failure loads available for any of these columns, an important limitation that must be overcome in the future.

[41] The authors themselves acknowledged this deficiency, which was corrected in a subsequent second test campaign (Santos *et al.* 2014).

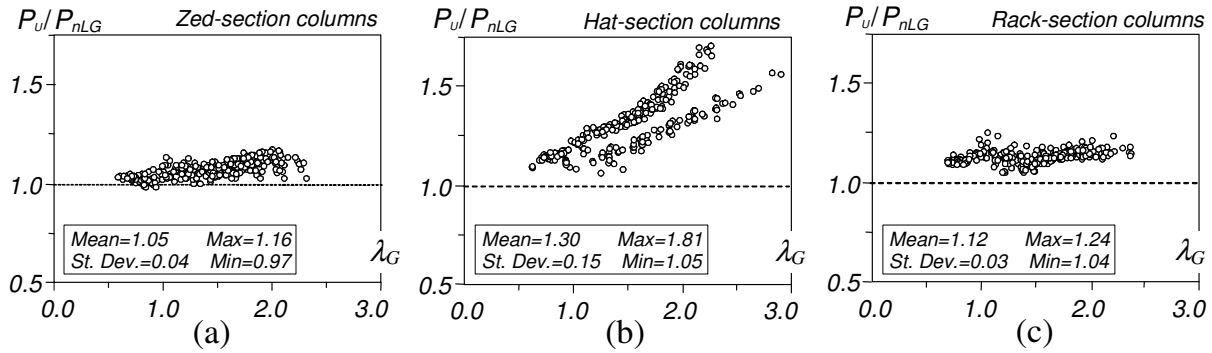

Figure 64: Plots P_u/P_{nLG} vs. λ_G concerning the (a) zed, (b) hat and (c) rack-section column numerical failure loads

Finally, one last word to call attention to the failure load prediction accuracy provided by the P_{nLG} values is clearly higher for zed and rack-section columns (see Figs. 64(a)+(c)) than for their lipped channel and rack-section counterparts (see Figs. 63 – numerical values – and 64(b)). In the latter, there are very significant failure load underestimations for λ_G>1.5, which become more severe as the slenderness grows. This fact, combined with the quite surprising finding that, apparently, the involvement of distortional buckling does not influence the failure load erosion of columns undergoing L-D-G interaction, prompted a numerical investigation on the accuracy of the currently codified DSM column global strength curve, since such accuracy (or lack of it) may be the source of the above unexpected features. The outcome of this study, which will be presented at this conference (Dinis *et al.* 2018), will certainly "force" a revisit to the available results on the behavior and design of columns affected by L-D-G (and also D-G) interaction.

8. Concluding Remarks

An overview of my research activity on structural stability in the last two decades (*i.e.*, since I joined SSRC back in 1997) was provided. The main results and findings obtained in several investigations in which I have collaborated on topics/problems dealing with the geometrically non-linear behavior of thin-walled structural members and systems were presented and briefly discussed – the common thread between them is the fact that virtually were reported at SSRC Annual Stability Conferences (or Technical Sessions & Meetings) before appearing in international journals.

The various topics/problems and results/findings, which were presented in chronological order as much as possible, concerned (i) the stability, non-linear strength and design of pitched-roof frames, (ii) the distortional post-buckling behavior, ultimate strength and DSM design of cold-formed steel columns and beams, (iii) the lateral-torsional stability of doubly and singly symmetric web-tapered beams, (iv) GBT formulations and applications dealing with linear buckling and elastic post-buckling analyses, (v) the stability, failure and DSM design of cold-formed steel equal-leg angle columns, and (vi) the post-buckling behavior, ultimate strength and DSM design of cold-formed steel columns and beams affected by local-distortional, local-distortional-global or distortional-global interaction – analytical, numerical and experimental results were addressed.

I cannot close this paper without a last word to congratulate and pay tribute to SSRC for its invaluable role in fostering and disseminating research on Structural Stability topics/problems, and for putting together, year after year, such a unique conference[42]. Thank you very much and see you all again in St. Louis!

[42] As far as the organization of the Annual Stability Conference is concerned, the funding, support and help of the American Institute of Steel Construction (AISC) is very gratefully acknowledged. Indeed, the "unique character" of the conference would be utterly impossible without the generosity and care of this prestigious institution (not even in dreams…).

References

Abambres M, Camotim D, Silvestre N, Rasmussen KJR (2013). GBT-based structural analysis of elastic-plastic thin-walled members, *Computers & Structures*, **136**(May), 1-23.

Abambres M, Camotim D, Silvestre N (2014). GBT-based elastic-plastic post-buckling analysis of stainless steel thin-walled members, *Thin-Walled Structures*, **83**(October), 85-102.

AISI (American Iron and Steel Institute) (2012). *North American Specification* (NAS) *for the Design of Cold-Formed Steel Structural Members* (AISI-S100-12), Washington DC.

AISI (American Iron and Steel Institute) (2016). *North American Specification* (NAS) *for the Design of Cold-Formed Steel Structural Members* (AISI-S100-16), Washington DC.

Andrade A, Camotim D (2004). Lateral-torsional buckling of prismatic and tapered thin-walled open beams: assessing the influence of pre-buckling deflections. *Steel & Composite Structures*, **4**(4), 281-301.

Andrade A, Camotim D (2005). Lateral-torsional buckling of singly symmetric tapered beams: theory and applications. *Journal of Engineering Mechanics* (ASCE), **131**(6), 586-597.

Andrade A, Camotim D, Dinis PB (2007). Lateral-torsional buckling of singly symmetric web-tapered thin-walled I-beams: 1D model *vs.* shell FEA. *Computers & Structures*, **85**(17-18), 1343-1359.

Andrade A, Providência P, Camotim D (2010). Elastic lateral-torsional buckling of restrained web-tapered I-beams, *Computers & Structures*, **88**(21-22), 1179-1196.

Basaglia C, Camotim D (2013). Enhanced generalised beam theory buckling formulation to handle transverse load application effects, *International Journal of Solids and Structures*, **50**(3-4), 531-547.

Basaglia C, Camotim D, Silvestre N (2008). Global buckling analysis of plane and space thin-walled frames in the context of GBT, *Thin-Walled Structures*, **46**(1), 79-101.

Basaglia C, Camotim D, Silvestre N (2009), GBT-based local, distortional and global buckling analysis of thin-walled steel frames, *Thin-Walled Structures*, **47**(11), 1246-1264.

Basaglia C, Camotim D, Silvestre N (2011). Non-linear GBT formulation for open-section thin-walled members with arbitrary support conditions, *Computers & Structures*, **89**(21-22), 1906-1919.

Basaglia C, Camotim D, Silvestre N (2012). Torsion warping transmission at thin-walled frame joints: kinematics, modelling and structural response, *Journal of Constructional Steel Research*, **69**(1), 39-53.

Bebiano R, Silvestre N, Camotim D (2007). GBT formulation to analyze the buckling behaviour of thin-walled members subjected to non-uniform bending. *International Journal of Structural Stability and Dynamics*, **7**(1), 23-54.

Bebiano R, Gonçalves R, Camotim D (2015). A cross-section analysis procedure developed to rationalize and automate the performance of GBT-based structural analyses, *Thin-Walled Structures*, **92**(July), 29-47.

Bebiano R, Camotim D, Gonçalves R (2018a). GBTUL 2.0 – a second-generation code for the GBT-based buckling and vibration analysis of thin-walled members, *Thin-Walled Structures*, **124**(March), 235-257.

Bebiano R, Basaglia C, Camotim D, Gonçalves R (2018b). GBT buckling analysis of generally loaded thin-walled members with arbitrary flat-walled cross-sections, *Thin-Walled Structures*, **123**(February), 11-24.

Boissonnade N, Muzeau JP (2001). New beam finite element for tapered members, *Proceedings of 8th International Conference on Civil and Structural Engineering Computing* (CC 2001–Vienna, 19-21/9**),** B. Topping (ed.), Civil-Comp Press (Stirlinshire), 73-74. (full paper in CD-ROM Procedings –paper 27)

Camotim D, Basaglia C (2013). Buckling analysis of thin-walled structures using Generalised Beam Theory (GBT): state-of-the-art report, *Steel Construction*, **6**(2), 117-131.

Camotim D, Dinis PB (2011). Coupled instabilities with distortional buckling in cold-formed steel lipped channel columns, *Thin-Walled Structures*, **49**(5), 562-575.

Camotim D, Dinis PB (2013). Distortional-global interaction in lipped channel columns, *Proceedings of the Institution of Civil Engineers (ICE)-Structures and Buildings*, **166**(8), 381-391.

Camotim D, Silvestre N, Gonçalves R, Dinis PB (2004). GBT analysis of thin-walled members: new formulations and applications, *Thin-Walled Structures: Recent Advances and Future Trends in Thin-Walled Structures Technology,* J. Loughlan (ed.), Canopus Publishing Ltd. (Bath), 137-168.

Camotim D, Silvestre N, Basaglia C, Bebiano R (2008). GBT-based buckling analysis of thin-walled members with non-standard support conditions. *Thin-Walled Structures*, **46**(7-9), 800-815.

Camotim D, Basaglia C, Silvestre N (2010). GBT buckling analysis of thin-walled steel frames: a state-of-the-art report, *Thin-Walled Structures*, **48**(10-11), 726-743.

Camotim D, Dinis PB, Martins AD (2016). Direct Strength Method (DSM) – a general approach for the design of cold-formed steel structures, *Recent Trends in Cold-Formed Steel Construction*, C. Yu (ed.), Woodhead Publishing (Amsterdam), 69-105.

Cava D, Camotim D, Dinis PB, Madeo A (2016). Numerical investigation and direct strength design of cold-formed steel lipped channel columns experiencing local-distortional-global interaction, *Thin-Walled Structures*, **105**(August), 231-247.

CEN (Comité Européen de Normalisation) (2005). *Eurocode 3: Design of Steel Structures – Part 1-1: General Rules and Rules for Buildings*, EN 1993-1-1:2005, Brussels, Belgium.

Dinis PB, Camotim D (2011). Post-buckling behaviour and strength of cold-formed steel lipped channel columns experiencing distortional/global interaction, *Computers & Structures*, **89**(3-4), 422-434.

Dinis PB, Camotim D (2015a). A novel DSM-based approach for the rational design of fixed-ended and pin-ended short-to-intermediate thin-walled angle columns, *Thin-Walled Structures*, **87**(February), 158-182.

Dinis PB, Camotim D (2015b). Cold-formed steel columns undergoing local-distortional coupling: behaviour and direct strength prediction against interactive failure, *Computers & Structures*, **147**(January), 181-208.

Dinis PB, Camotim D (2016a). Proposal for the codification of a DSM design approach for cold-formed steel short-to-intermediate angle columns, *Proceedings of Wei-Wen Yu International Specialty Conference on Cold-Formed Steel Structures* (CCFSS 2016 – Baltimore, 9-10/11) R. LaBoube, W.-W. Yu (eds.), 155-171.

Dinis PB, Camotim D (2016b). Behaviour and DSM design of hat, zed and rack columns experiencing local-distortional-global interaction, *USB Key Drive Proceedings of Eighth International Conference on Steel and Aluminium Structures* (ICSAS 2016 – Hong Kong, 7-9/12), B. Young, Y. Cai (eds.), Paper 60.

Dinis PB, Camotim D, Silvestre N (2012a). On the mechanics of angle column instability, *Thin-Walled Structures*, **52**(March), 80-89.

Dinis PB, Batista EM, Camotim D, Santos ES (2012b). Local-distortional-global interaction in lipped channel columns: experimental results, numerical simulations and design considerations, *Thin-Walled Structures*, **61**(December), 2-13.

Dinis PB, Young B, Camotim D (2014). Local-distortional interaction in cold-formed steel rack-section columns, *Thin-Walled Structures*, **81**(August), 185-194.

Dinis PB, Camotim D, Young B, Batista EM (2017). CFS lipped channel columns affected by L-D-G interaction – II: numerical simulations and design considerations, *Computers & Structures,* in press, 2018.

Dinis PB, Camotim D, Martins AD (2018). On the accuracy of the current Direct Strength Method (DSM) design curve for columns failing in global modes, *Website Proceedings of Structural Stability Research Council (SSRC) 2018 Annual Stability Conference* (Baltimore, 10-13/4).

Ganesan K, Moen CD (2012). LRFD resistance factor for cold-formed steel compression members, *Journal of Constructional Steel Research*, **72**(May), 261-266.

Gonçalves R, Camotim D (2012). Geometrically non-linear Generalized Beam Theory for elastoplastic thin-walled metal members, *Thin-Walled Structures*, **51**(February), 121-129.

Gonçalves R, Bebiano R, Camotim D (2014). On the shear deformation modes in the framework of Generalised Beam Theory, *Thin-Walled Structures*, **84**(November), 325-334.

He Z, Zhou X, Liu Z, Chen M (2014). Post-buckling behaviour and DSM design of web-stiffened lipped channel columns with distortional and local mode interaction, *Thin-Walled Structures,* **84**(November), 189-203.

Horne M (1975). An approximate method for calculating the elastic critical loads of multi-storey plane frames, *The Structural Engineer*, **53**(6), 242-248.

Kwon YB, Hancock GJ (1992). Tests of cold-formed channels with local and distortional buckling, *Journal of Structural Engineering* (ASCE)*,* **118**(7), 1786-1803.

Kwon YB, Kim NK, Kim BS (2005). A study on the direct strength method for compression members undergoing mixed mode buckling, *Proceedings of 3rd International Symposium on Steel Structures* (ISSS'05 – Seoul 10-11/03), 108-119.

Kwon YB, Kim BS, Hancock GJ (2009). Compression tests of high strength cold-formed steel channel with buckling interaction, *Journal of Constructional Steel Research*, **65**(2), 278-289.

Landesmann A, Camotim D (2011). On the distortional buckling, post-buckling and strength of cold-formed steel lipped channel columns under fire conditions. *Journal of Structural Fire Engineering,* **2**(1), 1-19.

Landesmann A, Camotim D (2013). On the Direct Strength Method (DSM) design of cold-formed steel columns against distortional failure, *Thin-Walled Structures*, **67**(June), 168-187.

Landesmann A, Camotim D (2016). Distortional failure and DSM design of cold-formed steel lipped channel beams under elevated temperatures, *Thin-Walled Structures*, **98A**(January), 75-93.

Landesmann A, Camotim D, Dinis PB, Cruz R (2016). Short-to-intermediate slender pin-ended cold-formed steel equal-leg angle columns: experimental investigation, numerical simulation and DSM design, *Engineering Structures*, **132**(February), 471-493.

Lee G, Szabo B (1967). Torsional response of tapered I-girders. Journal of the Structural Division (ASCE), **93**(5), 233-252.

Lutz LA (2017). The history of the development of the single angle design provisions in the AISC specification, *Website Proceedings of Structural Stability Research Council (SSRC) 2017 Annual Stability Conference* (San Antonio, 21-24/3).

Martins AD, Dinis PB, Camotim D, Providência P (2015). On the relevance of local-distortional interaction effects in the behaviour and design of cold-formed steel columns, *Computers & Structures*, **160**(November), 57-89.

Martins AD, Dinis PB, Camotim D (2016). On the Influence of local-distortional interaction in the behaviour and design of cold-formed steel web-stiffened lipped channel columns, *Thin-Walled Structures*, **101**(April), 181-204.

Martins AD, Camotim D, Dinis PB (2017a). On the direct strength design of cold-formed steel columns failing in local-distortional interactive modes, *Thin-Walled Structures*, **120**(November), 432-445.

Martins AD, Landesmann A, Camotim D, Dinis PB (2017b). Distortional failure of cold-formed steel beams under uniform bending: behaviour, strength and DSM design, *Thin-Walled Structures*, **118**(September), 196-213.

Martins AD, Camotim D, Dinis PB (2017c). Local-distortional interaction in cold-formed steel beams: behaviour, strength and DSM design, *Thin-Walled Structures*, **119**(October), 879-901.

Martins AD, Camotim D, Dinis PB (2017d). Behaviour and DSM design of cold-formed steel stiffened lipped channel columns undergoing local-distortional interaction, *Journal of Constructional Steel Research*, **128**(January), 99-118.

Martins AD, Camotim D, Gonçalves R, Dinis PB (2018a). GBT-based assessment of the mechanics of distortional-global interaction in thin-walled lipped channel beams, *Thin-Walled Structures* **124**(March), 32-47.

Martins AD, Camotim D, Gonçalves R, Dinis PB (2018b). Enhanced geometrically non-linear Generalized Beam Theory (GBT) formulation: derivation, numerical Implementation and illustration, *Journal of Structural Engineering* (ASCE), accepted for publication.

Martins AD, Camotim D, Dinis PB (2018c). Distortional-global interaction in lipped channel and zed-section beams: strength, relevance and DSM design, *Thin-Walled Structures*, accepted for publication.

Martins AD, Camotim D, Dinis PB (2018d). On the distortional-global interaction in cold-formed steel columns: relevance, post-buckling behaviour, strength and DSM design, *Journal of Constructional Steel Research*, accepted for publication.

Martins AD, Camotim D, Gonçalves R, Dinis PB (2018e). On the mechanics of distortional-global interaction in fixed-ended columns, *Thin-Walled Structures*, **123**(February), 162-184.

Mesacasa Jr. E, Dinis PB, Camotim D, Malite M (2014). Mode interaction and imperfection-sensitivity in thin-walled equal-leg angle columns, *Thin-Walled Structures*, **81**(August), 138-149.

Prola LC, Camotim D (2002a). On the distortional post-buckling behavior of cold-formed lipped channel steel columns, *Proceedings of Structural Stability Research Council (SSRC) 2002 Annual Stability Conference* (Seattle, 24-27/4), 571-590.

Prola LC, Camotim D (2002b). On the distortional post-buckling behaviour of cold-formed lipped channel steel beams, *Advances in Steel Structures* (ICASS'02 – Hong Kong, 9-11/2), S.L. Chan, J.G. Teng, K.F. Chung (eds.), Elsevier (Amsterdam) 331-339 (vol. 1).

Prola LC, Camotim D (2002c). On the distortional post-buckling behaviour of rack-section cold-formed steel columns, *Proceedings of 6th International Conference on Computational Structures Technology* (CST 2002 – Prague, 4-6/9), B. Topping, Z. Bittnar (eds.), Civil-Comp Press (Stirling). (full paper in CD-ROM Proceedings – paper 98)

Rasmussen KJR (2006). Design of slender angle section beam-columns by the direct strength method, *Journal of Structural Engineering* (ASCE), **132**(2), 204-211.

Santos ES, Batista EM, Camotim D (2012). Experimental investigation concerning lipped channel columns undergoing local-distortional-global buckling mode interaction, *Thin-Walled Structures*, **54**(May), 19-34.

Santos ES, Batista EM, Camotim D (2014). Cold-formed steel columns under L-D-G interaction: experimental investigation, *Steel Construction*, **7**(3), 193-198.

Schafer BW (2002). Local, distortional and Euler buckling in thin-walled columns, *Journal of Structural Engineering* (ASCE), **128**(3), 289-299.

Schafer BW (2005). *Direct Strength Method Design Guide*, American Iron and Steel Institute (AISI) Report, Washington DC.

Schafer BW (2008). Review: the Direct Strength Method of cold-formed steel member design, *Journal of Constructional Steel Research*, **64**(7-8), 766-788.

Schafer BW, Peköz T (1998). Computational modeling of cold-formed steel: characterizing geometric imperfections and residual stresses, *Journal of Constructional Steel Research*, **47**(3), 193-210.

Shifferaw Y, Schafer BW (2012). Inelastic bending capacity of cold-formed steel members, *Journal of Structural Engineering* (ASCE), **138**(4), 468-480.

Silvestre N, Camotim D (1999). Étude sur la stabilité des portiques à traverse brisée, *Revue Construction Métallique*, nº 4, 5-20. (French)

Silvestre N, Camotim D (2003). Non-linear Generalized Beam Theory for cold-formed steel members, *International Journal of Structural Stability and Dynamics*, **3**(4), 461-490.

Silvestre N, Camotim D (2004a). Distortional buckling formulae for cold-formed steel C and Z-section members: part I – derivation, *Thin-Walled Structures*, **42**(11), 1567-1597.

Silvestre N, Camotim D (2004b). Distortional buckling formulae for cold-formed steel C and Z-section members: part II – validation and pplication, *Thin-Walled Structures*, **42**(11), 1599-1629.

Silvestre N, Camotim D (2004c). Distortional buckling formulae for cold-formed steel rack-section members, *Steel & Composite Structures*, **4**(1), 49-75.

Silvestre N, Camotim D (2006). Local-plate and distortional postbuckling behavior of cold-formed steel lipped channel columns with intermediate stiffeners", *Journal of Structural Engineering* (ASCE), **132**(4), 529-540.

Silvestre N, Camotim D (2007). Elastic buckling and second-order behaviour of pitched-roof steel frames, *Journal of Constructional Steel Research*, **63**(6), 814-818.

Silvestre N, Camotim D, Ritto-Corrêa M (1998). On the design and safety checking of unbraced pitched-roof steel frames, *Journal of Constructional Steel Research*, **46**(1-3), 328-330. (full paper in CD-ROM – paper 188)

Silvestre N, Bebiano R, Camotim D (2005). On the distortional post-buckling asymmetry of cold-formed steel channel columns with different stiffener configurations, *Proceedings of SSRC Annual Stability Conference* (Montreal, 6-9/04), 63-88.

Silvestre N, Camotim D, Dinis PB (2012). Post-buckling behaviour and direct strength design of lipped channel columns experiencing local/distortional interaction, *Journal of Constructional Steel Research,* **73**(June), 12-30.

Silvestre N, Dinis PB, Camotim D (2013). Developments on the design of cold-formed steel angles, *Journal of Structural Engineering* (ASCE), **139**(5), 680-694.

Torabian S, Schafer BW (2018). Development and experimental validation of the Direct Strength Method for cold-formed steel beam-columns, *Journal of Structural Engineering* (ASCE), accepted for publication.

Trahair NS, Bradford MA, Nethercot DA, Gardner L (2006). *The Behaviour and Design of Steel Structures to EC3*, Spon Press (London).

Yang D, Hancock GJ (2004). Compression tests of high strength steel channel columns with interaction between local and distortional buckling, *Journal of Structural Engineering* (ASCE), **130**(12), 1954-1963.

Yang YB, Yau JD (1987). Stability of beams with tapered I-sections, *Journal of Engineering Mechanics* (ASCE), **113**(9), 1337-1357.

Yap DCY, Hancock GJ (2011). Experimental study of high strength cold-formed stiffened-web C-sections in compression, *Journal of Structural Engineering* (ASCE)*,* **137**(2), 162-172.

Young B (2004). Tests and design of fixed-ended cold-formed steel plain angle columns, *Journal of Structural Engineering* (ASCE), **130**(12), 1931-1940.

Young B, Rasmussen KJR (1998). Design of lipped channel columns, *Journal of Structural Engineering* (ASCE), **124**(2), 140-148.

Young B, Rasmussen KJR (1999). Shift of effective centroid in channel columns, *Journal of Structural Engineering* (ASCE), **125**(5), 524-531.

Young B, Silvestre N, Camotim D (2013). Cold-formed steel lipped channel columns influenced by local-distortional interaction: strength and DSM design, *Journal of Structural Engineering* (ASCE)*,* **139**(6), 1059-1074.

Young B, Dinis PB, Camotim D (2017). CFS lipped channel columns affected by L-D-G interaction – I: experimental investigation, *Computers & Structures,* in press.

Yu C, Schafer BW (2003). Local buckling tests on cold-formed steel beams, *Journal of Structural Engineering* (ASCE), **129**(12), 1596-1606.

Yu C, Schafer BW (2006). Distortional buckling tests on cold-formed steel beams, *Journal of Structural Engineering* (ASCE), **132**(4), 515-528.

ANNEX A: CO-AUTHORED PAPERS PUBLISHED IN SSRC PROCEEDINGS

- **1997 (Toronto)**

Silvestre N. Camotim D (1997). Second-order effects in pitched-roof steel frames, *Proceedings of Structural Stability Research Council (SSRC) 1997 Annual Technical Session and Meeting* (Toronto, 9-11/6), 85-98.

- **1998 (Atlanta)**

Batista EM, Camotim D, Prola LC, Vazquez E (1999). On the local buckling behavior of rack section thin-walled columns, *Proceedings of Structural Stability Research Council (SSRC) 1998 Annual Technical Session and Meeting* (Atlanta, 21-23/9), 107-120.

Silvestre N, Mesquita A, Camotim D, Silva LS (2000). In-plane buckling behavior of pitched-roof steel frames with semi-rigid connections, *Frames with Partially Restrained Connections* – Structural Stability Research Council (SSRC) 1998 Theme Conference Workshop Volume (Atlanta, 21-23/9), 21-34.

- **2000 (Memphis)**

Camotim D, Batista EM, Prola LC, Vazquez E (2000). Southwell plot estimation of local critical stresses in thin-walled columns, *Proceedings of Structural Stability Research Council (SSRC) 2000 Annual Technical Session and Meeting* (Memphis, 24-26/7), 171-184.

Batista EM, Camotim D, Prola LC, Vazquez E (2000). On the influence of the end plate conditions on the distortional buckling of cold-formed rack sections, *Proceedings of Structural Stability Research Council (SSRC) 2000 Annual Technical Session and Meeting* (Memphis, 24-26/7), 185-198.

Silvestre N, Camotim D (2000). In-plane stability and 2nd order effects in multi-bay pitched-roof steel frames, *Proceedings of Structural Stability Research Council (SSRC) 2000 Annual Technical Session and Meeting* (Memphis, 24-26/7), 89-103.

Nogueiro P, Silva LS, Silvestre N, Camotim D (2000). Non-linear behavior of pitched-roof frames with bi-linear semi-rigid connections, *Proceedings of Structural Stability Research Council (SSRC) 2000 Annual Technical Session and Meeting* (Memphis, 24-26/7), 104-116.

- **2001 (Fort Lauderdale)**

Camotim D, Prola LC (2001). On the accounting of local post-buckling effects in the global behavior of cold-formed steel columns, *Proceedings of Structural Stability Research Council (SSRC) 2001 Annual Technical Session and Meeting* (Fort Lauderdale, 9-12/5), 383-402.

Gonçalves R, Camotim D (2001). First and second-order design or safety checking of steel frames: allowance for member imperfections, *Proceedings of Structural Stability Research Council (SSRC) 2001 Annual Technical Session and Meeting* (Fort Lauderdale, 9-12/5), 333-352.

- **2002 (Seattle)**

Prola LC, Camotim D (2002). On the distortional post-buckling behavior of cold-formed lipped channel steel columns, *Proceedings of Structural Stability Research Council (SSRC) 2002 Annual Stability Conference* (Seattle, 24-27/4), 571-590.

Silvestre N, Camotim D (2002). Post-buckling behavior, imperfection-sensitivity and mode interaction in pitched-roof steel frames, *Proceedings of Structural Stability Research Council (SSRC) 2002 Annual Stability Conference* (Seattle, 24-27/4), 139-162.

- **2003 (Baltimore)**

Andrade A, Camotim D (2003). Lateral-torsional buckling of singly symmetric web-tapered I-section steel beams and cantilevers, *Proceedings of Structural Stability Research Council (SSRC) 2003 Annual Technical Session and Meeting* (Baltimore, 2-5/4), 233-254.

Silvestre N, Camotim D (2003). GBT-based approach to develop distortional buckling formulae for cold-formed steel members, *Proceedings of Structural Stability Research Council (SSRC) 2003 Annual Technical Session and Meeting* (Baltimore, 2-5/4), 493-518.

- **2004 (Long Beach)**

Dinis PB, Camotim D (2004). Local-plate and distortional post-buckling behavior of cold-formed steel columns: elastic and elastic-plastic FEM analysis, *Proceedings of Structural Stability Research Council (SSRC) 2004 Annual Stability Conference* (Long Beach, 24-27/3), 475-498.

Silvestre N, Camotim D (2004). Towards an efficient design against distortional buckling: formulae for C and Z-section cold-formed steel members, *Proceedings of Structural Stability Research Council (SSRC) 2004 Annual Stability Conference* (Long Beach, 24-27/3), 239-263.[43]

- **2005 (Montreal)**

Silvestre N, Bebiano R, Camotim D (2005). On the distortional post-buckling asymmetry of cold-formed steel channel columns with different stiffener configurations, *Proceedings of Structural Stability Research Council (SSRC) 2005 Annual Stability Conference* (Montreal, 6-9/4), 63-88.

Andrade A, Camotim D, Costa PP (2005). Elastic lateral-torsional buckling behavior of doubly symmetric tapered beam-columns, *Proceedings of Structural Stability Research Council (SSRC) 2005 Annual Stability Conference*, (Montreal, 6-9/4), 445-468.

- **2006 (San Antonio)**

Bebiano R, Silvestre N, Camotim D (2006). On the influence of stress gradients on the local-plate, distortional and global buckling behavior of thin-walled steel members, *Proceedings of Structural Stability Research Council (SSRC) 2006 Annual Stability Conference* (San Antonio, 8-11/2), 301-327.

Gonçalves R, Dinis PB, Camotim D (2006). GBT linear and buckling analysis of thin-walled multi-cell box girders, *Proceedings of Structural Stability Research Council (SSRC) 2006 Annual Stability Conference* (San Antonio, 8-11/2), 329-352.

- **2007 (New Orleans)**

Basaglia C, Camotim D, Silvestre N (2007). GBT-based analysis of the local-plate, distortional and global buckling behavior of thin-walled steel frames, *Proceedings of Structural Stability Research Council (SSRC) 2007 Annual Stability Conference* (New Orleans, 18-21/4), 391-412.

Surovek AE, White DW, Ziemian RD, Camotim D, Hajjar JF, Teh LH (2007). Recommendations for the use of direct second-order inelastic analysis to design steel frames, *Proceedings of Structural Stability Research Council (SSRC) 2007 Annual Stability Conference* (New Orleans, 18-21/4), 301-315.

Martins A, Dinis PB, Camotim D (2007). On the post-buckling behavior of cold-formed steel lipped channel beams affected by local-plate/distortional buckling mode interaction, *Proceedings of Structural Stability Research Council (SSRC) 2007 Annual Stability Conference* (New Orleans, 18-21/4), 413-435.

Hansoulle T, Boissonnade N, Gonçalves R, Camotim D, Jaspart JP (2007). Design of beam-columns in steel sway frames: from the actual member to a simply supported equivalent one, *Proceedings of Structural Stability Research Council (SSRC) 2007 Annual Stability Conference* (New Orleans, 18-21/4), 177-200.

Alves MC, Batista EM, Camotim D (2007). Buckling, post-buckling and ultimate strength of cold-formed steel members under fire condition, *Proceedings of Structural Stability Research Council (SSRC) 2007 Annual Stability Conference* (New Orleans, 18-21/4), 541-563.

- **2008 (Nashville)**

Basaglia C, Camotim D, Silvestre N (2008). GBT-based post-buckling analysis of thin-walled steel members and frames, *Proceedings of Structural Stability Research Council (SSRC) 2008 Annual Stability Conference* (Nashville, 2-5/4), 215-237.

Dinis PB, Camotim D (2008). Post-buckling analysis of cold-formed steel lipped channel columns affected by distortional-global mode interaction, *Proceedings of Structural Stability Research Council (SSRC) 2008 Annual Stability Conference* (Nashville, 2-5/4), 405-431.

[43] Nuno Silvestre received the SSRC 2004 Vinnakota Award for this paper.

- **2009 (Phoenix)**

Basaglia C, Camotim D, Silvestre N (2009). Latest developments on the GBT-based buckling analysis of thin-walled steel frames, *Proceedings of Structural Stability Research Council (SSRC) 2009 Annual Stability Conference* (Phoenix, 1-4/4), 325-344.

Dinis PB, Camotim D (2009). Local-distortional-global buckling mode interaction in cold-formed steel lipped channel columns, *Proceedings of Structural Stability Research Council (SSRC) 2009 Annual Stability Conference* (Phoenix, 1-4/4), 295-323.

- **2010 (Kissimmee – Orlando)**

Basaglia C, Camotim D, Silvestre N (2010). Non-linear GBT for thin-walled steel frames: formulation, implementation and application, *Proceedings of Structural Stability Research Council (SSRC) 2010 Annual Stability Conference* (Kissimmee-Orlando, 11-15/5), 461-480.

Dinis PB, Camotim D (2010). Local-distortional-global buckling mode interaction in cold-formed steel rack-section columns, *Proceedings of Structural Stability Research Council (SSRC) 2010 Annual Stability Conference* (Kissimmee-Orlando, 11-15/5), 481-504.

Landesmann A, Camotim D (2010). Distortional failure and design of cold-formed steel lipped channel columns under fire conditions, *Proceedings of Structural Stability Research Council (SSRC) 2010 Annual Stability Conference*, (Kissimmee-Orlando, 11-15/5), 505-532.

- **2011 (Pittsburgh)**

Basaglia C, Camotim D (2011). On the incorporation of load application effects in the GBT buckling analysis of thin-walled steel beams and frames, *USB Key Drive Proceedings of Structural Stability Research Council (SSRC) 2011 Annual Stability Conference* (Pittsburgh, 10-14/5).

Dinis PB, Camotim D (2011). Buckling, post-buckling and strength of cruciform columns, *USB Key Drive Proceedings of Structural Stability Research Council (SSRC) 2011 Annual Stability Conference* (Pittsburgh, 10-14/5).

Landesmann A, Camotim D (2011). DSM design of cold-formed steel columns against distortional failure: investigation on the influence of the cross-section geometry and support conditions, *USB Key Drive Proceedings of Structural Stability Research Council (SSRC) 2011 Annual Stability Conference* (Pittsburgh, 10-14/5).

- **2012 (Grapevine – Dallas)**

Basaglia C, Camotim D (2012). On the behavior, failure and DSM design of thin-walled steel frames, *USB Key Drive Proceedings of Structural Stability Research Council (SSRC) 2012 Annual Stability Conference* (Grapevine-Dallas, 17-21/4), paper 8.

Dinis PB, Camotim D, Fena R (2012). Post-buckling, strength and design of cold-formed steel lipped channel, hat-section and zed-section columns affected by local-distortional interaction, *USB Key Drive Proceedings of Structural Stability Research Council (SSRC) 2012 Annual Stability Conference* (Grapevine-Dallas, 17-21/4), paper 23.

Dinis PB, Camotim D, Silvestre N (2012). -Buckling, post-buckling, strength and design of angle columns, *USB Key Drive Proceedings of Structural Stability Research Council (SSRC) 2012 Annual Stability Conference* (Grapevine-Dallas, 17-21/4), paper 5.

Graça A, Basaglia C, Camotim D, Gonçalves R (2012). GBT-based assessment of the buckling behavior of cold-formed steel purlins restrained by sheeting, *USB Key Drive Proceedings of Structural Stability Research Council (SSRC) 2012 Annual Stability Conference* (Grapevine-Dallas, 17-21/4), paper 10.[44]

Landesmann A, Camotim D (2012). DSM design of cold-formed steel columns failing distortionally exposed to fire: how relevant is the temperature dependence of the material behavior?, *USB Key Drive Proceedings of Structural Stability Research Council (SSRC) 2012 Annual Stability Conference* (Grapevine-Dallas, 17-21/4), paper 29.

Mesacasa Jr. EC, Camotim D, Dinis PB, Malite M (2012). Flexural buckling of simply supported columns with 'rigid end inks' – the key to interpret pin-ended angle column test results?, *USB Key Drive Proceedings of Structural Stability Research Council (SSRC) 2012 Annual Stability Conference* (Grapevine-Dallas, 17-21/4), paper 4.

[44] André Graça obtained an honourable mention concerning the SSRC 2012 Vinnakota Award for this paper.

- **2013 (St. Louis)**

Abambres M, Camotim D, Silvestre N (2013). GBT-based structural analysis of elastic-plastic thin-walled members, *USB Key Drive Proceedings of Structural Stability Research Council (SSRC) 2013 Annual Stability Conference* (St. Louis, 16-20/4), 621-653.[45]

Dinis PB, Camotim D, Landesmann A (2013). Towards a more rational DSM design approach for angle columns, *USB Key Drive Proceedings of Structural Stability Research Council (SSRC) 2013 Annual Stability Conference* (St. Louis, 16-20/4), 471-502.

Dinis PB, Green PS, Camotim D (2013). Numerical and experimental investigation on the post-buckling behavior, ultimate strength and DSM design of thin-walled cruciform steel columns, *USB Key Drive Proceedings of Structural Stability Research Council (SSRC) 2013 Annual Stability Conference* (St. Louis, 16-20/4), 503-524.

Landesmann A, Camotim D, Basaglia C (2013). Distortional post-buckling behavior and strength of cold-formed steel columns: how does the cross-section geometry affect it?, *USB Key Drive Proceedings of Structural Stability Research Council (SSRC) 2013 Annual Stability Conference* (St. Louis, 16-20/4), 294-312.

Tomás J, Nseir J, Camotim D, Boissonnade N (2013). Stability, failure and design of I-section beams subjected to tension, *USB Key Drive Proceedings of Structural Stability Research Council (SSRC) 2013 Annual Stability Conference* (St. Louis, 16-20/4), 669-695.

- **2014 (Toronto)**

Basaglia C, Landesmann A, Camotim D (2014). About the influence of the cross-section geometry on the distortional post-buckling strength of cold-formed steel columns, *AISC Website Proceedings of Structural Stability Research Council (SSRC) 2014 Annual Stability Conference* (Toronto, 25-28/3).

Dinis PB, Camotim D, Peres N (2014). A novel DSM-based approach for the rational design of fixed-ended and pin-ended short-to-intermediate angle columns, *USB Key Drive Proceedings of Structural Stability Research Council (SSRC) 2014 Annual Stability Conference* (Toronto, 25-28/3), 129-165.

Landesmann A, Camotim D (2014). Cold-formed steel lipped channel beams under fire conditions: distortional response, failure and DSM design, *USB Key Drive Proceedings of Structural Stability Research Council (SSRC) 2014 Annual Stability Conference* (Toronto, 25-28/3), 182-212.

Martins AD, Dinis PB, Camotim D, Providência P (2014). On the relevance of local-distortional interaction effects in the behavior and design of cold-formed steel columns, *USB Key Drive Proceedings of Structural Stability Research Council (SSRC) 2014 Annual Stability Conference* (Toronto, 25-28/3), 388-431.[46]

- **2015 (Nashville)**

Basaglia C, Camotim D, Silvestre N (2015). GBT-based assessment of the buckling behavior of steel frames formed by circular hollow section members, *Website Proceedings of Structural Stability Research Council (SSRC) 2015 Annual Stability Conference* (Nashville, 24-27/3).

Bebiano R, Basaglia C, Camotim D, Gonçalves R (2015). GBT buckling analysis of generally loaded thin-walled members exhibiting arbitrary flat-walled cross-sections, *Website Proceedings of Structural Stability Research Council (SSRC) 2015 Annual Stability Conference* (Nashville, 24-27/3).

Dinis PB, Camotim D, Belivanis K, Roskos C, Helwig T (2015). On the buckling, post-buckling and strength behavior of thin-walled unequal-leg angle columns, *Website Proceedings of Structural Stability Research Council (SSRC) 2015 Annual Stability Conference* (Nashville, 24-27/3).

Landesmann A, Camotim D, Garcia R (2015). On the strength and DSM design of cold-formed steel web/flange-stiffened lipped channel columns buckling in distortional modes, *Website Proceedings of Structural Stability Research Council (SSRC) 2015 Annual Stability Conference* (Nashville, 24-27/3).

Martins AD, Camotim D, Dinis PB, Providência P (2015). On the mechanics of local-distortional interaction in lipped channel thin-walled columns, *Website Proceedings of Structural Stability Research Council (SSRC) 2015 Annual Stability Conference* (Nashville, 24-27/3).[47]

[45] Miguel Abambres received the SSRC 2013 Vinnakota Award for this paper.

[46] André Martins obtained an honourable mention concerning the SSRC 2014 Vinnakota Award for this paper.

[47] André Martins received the SSRC 2015 Vinnakota Award for this paper.

- **2016 (Kissimmee – Orlando)**

Basaglia C, Camotim D, Silvestre N, Palermo Jr. L (2016). GBT-based buckling analysis of circular cylindrical steel shells under uniform external pressure, *Website Proceedings of Structural Stability Research Council (SSRC) 2016 Annual Stability Conference* (Kissimmee-Orlando, 12-15/4).

Dinis PB, Young B, Camotim D (2016). Local-distortional-global interaction in cold-formed steel lipped channel columns: behavior, strength and DSM design, *Website Proceedings of Structural Stability Research Council (SSRC) 2016 Annual Stability Conference* (Kissimmee-Orlando, 12-15/4).

Gonçalves R, Henriques D, Camotim D (2016). Recent developments in the GBT-based numerical modeling of steel-concrete composite beams, *Website Proceedings of Structural Stability Research Council (SSRC) 2016 Annual Stability Conference* (Kissimmee-Orlando, 12-15/4).

Landesmann A, Camotim D, Dinis PB, Cruz R (2016). Short-to-intermediate slender pin-ended cold-formed steel equal-leg angle columns: experimental investigation and DSM design, *Website Proceedings of Structural Stability Research Council (SSRC) 2016 Annual Stability Conference* (Kissimmee-Orlando, 12-15/4).

Martins AD, Landesmann A, Camotim D, Dinis PB (2016). Distortional failure of cold-formed steel beams under uniform bending: behavior, strength and DSM design, *Website Proceedings of Structural Stability Research Council (SSRC) 2016 Annual Stability Conference* (Kissimmee-Orlando, 12-15/4).

Mesacasa Jr. E, Basaglia C, Camotim D, Malite M (2016). GBT-based buckling analysis of thin-walled steel frames with semi-rigid joints, *Website Proceedings of Structural Stability Research Council (SSRC) 2016 Annual Stability Conference* (Kissimmee-Orlando, 12-15/4).[48]

- **2017 (San Antonio)**

Dinis PB, Camotim D (2017). Spherically-hinged short-to-intermediate angle columns: stability, non-linear behavior and DSM design, *Website Proceedings of Structural Stability Research Council (SSRC) 2017 Annual Stability Conference* (San Antonio, 21-24/3).

Gonçalves R, Camotim D (2017). Efficient GBT displacement-based finite elements for non-linear problems, *Website Proceedings of Structural Stability Research Council (SSRC) 2017 Annual Stability Conference* (San Antonio, 21-24/3).

Landesmann A, Camotim D, Silva FCM (2017). DSM design of cold-formed steel columns failing in distortional modes at elevated temperatures, *Website Proceedings of Structural Stability Research Council (SSRC) 2017 Annual Stability Conference* (San Antonio, 21-24/3).

Martins AD, Camotim D, Dinis PB (2017). On the distortional-global interaction in cold-formed steel columns: relevance, post-buckling behavior, strength and DSM design, *Website Proceedings of Structural Stability Research Council (SSRC) 2017 Annual Stability Conference* (San Antonio, 21-24/3).

- **2018 (Baltimore)**

Depolli I, Landesmann A, Camotim D, Martins AD (2018). Distortional failure and DSM design of cold-formed steel lipped channel beams under non-uniform bending, *Website Proceedings of Structural Stability Research Council (SSRC) 2018 Annual Stability Conference* (Baltimore, 10-13/4).

Dinis PB, Camotim D, Martins AD (2018). On the accuracy of the current Direct Strength Method (DSM) design curve for columns failing in global modes, *Website Proceedings of Structural Stability Research Council (SSRC) 2018 Annual Stability Conference* (Baltimore, 10-13/4).

[48] Enio Mesacasa Jr. received the SSRC 2016 Vinnakota Award for this paper.